MINISTRY OF HIGHER EDUCATION AND SCIENTIFIC RESEARCH
HASSIBA BENBOUALI UNIVERSITY OF CHLEF
FACULTY OF TECHNOLOGY
MECHANICAL ENGINEERING DEPARTMENT

THESIS

Presented to obtain the degree of

DOCTORATE

Major: Mechanical Engineering

Specialty: Mechanical Construction

By

Abdelilah BOURAGBA

Title

Characterization of damage and anisotropy of DC06 sheet metal applied to deep drawing

Defended on 20 / 02 / 2025 before a jury composed of

Abdelkader HOCINE	Professor	University of Chlef	Chairman
Ibrahim ZIDANE	Professor	University of Chlef	Supervisor
Mohamed HADJ MILOUD	Professor	University of Chlef	Co-supervisor
Mohand OULD OUALI	Professor	University of Tizi Ouzou	Examiner
Chahinez FARES	Professor	University of Chlef	Examiner
Mohamed ELGUERRI	MCA	University of Tiaret	Examiner
Mohammed MENDAS	Professor	University of Chlef	Guest

Academic Year 2024 - 2025

Acknowledgements

الحمد والشكر لله أولًا وآخرًا على توفيقه وعونه

*Upon completion of this thesis, I heartily say, and with unwavering faith, that the Almighty, الله - **Allah**, has blessed me with helpful thoughts, strength, and patience, for which I can never be grateful enough.*

*Since the first meeting, I have always considered myself fortunate to have such supervisors, **Pr. Ibrahim ZIDANE** and **Dr. Mohamed HADJ MILOUD**, who, with time and work, along with invaluable guidance, mentorship, and patience, I consider myself gained, other than knowledge and expertise from him, a sincere person whom I look up to, to whom goes my extreme thanks, and with whom I wish to achieve more.*

*Further thanks go to the professors that examined the work, **Abdelkader HOCINE**, **Mohand OULD OUALI**, **Chahinez FARES**, and **Mohamed ELGUERRI**, for their time and efforts in accepting the evaluation of the thesis, improving its overall readability, and assessing the accuracy of the information.*

*I also extend my gratitude to the head of the department at **EIMS Company**, Mr. **BENHADJ M'HAMED Ali**, and Mr. **GUESSOUM Tayeb**, the head of services, for their valuable information, advice, and support throughout this journey.*

*I express my sincere appreciation to **Mr. Belkacem YAAKOUBI**, the responsible engineer of **Rheology and Mechanics Laboratory**, for his invaluable support and advice.*

*I am also grateful to the professors who have helped me in my education, **Mohamed ELGUERRI**, **Abdelkader KARAS**, **Ahmed BOUZIDANE**, and **Mohamed GUEMMOUR**, be it through their encouragement or their valuable feedback. The same goes for my colleagues for their cooperation and their insightful discussions.*

*Without forgetting the other parts of me who helped, encouraged, and stood by me with love even in difficult times. My dears, father **Abdallah**, the moral strengthener; mother, the foundation supporting me; and brothers, **Mohamed**, **Mouley**, and **Younes**. No words can express my gratitude for their sacrifices, and I will strive to make them proud and show my appreciation, even if it's just a fraction compared to what they have done for me. My relatives also have a part of my thanks for their attention and support.*

*Finally, a heartfelt hat tip to my wonderful friends, **Yassine EL GUERRI**, **Khaled Madani KOUADRIA**, **Chaaben ARROUSSI**, **Mohamed TELDJOUN**, **Naas ZAHOUT**, **Adel HADJ AMAR**, **Abdelwahab KHLEDJ**, **Abdelkader LOUZA**, **Amar Abdelouahed AIACHI**, **Nabil GUERBAS**, **Houssam BELMILOUD**, **Miloud BEKHAIRA**, **Bassam Gamal Nasser MUTHANA**, **Musaab SALAMA**, **Ahmed ELAGHA**, **Youcef AOUISSI**, **Amar BOUZIANE**, **Ahmed Ouadah BOUAKKAZ**, **Amina BELGUEBLI**, **Ghizlene Rahma RENNOU**, and many more, for being there with patience, understanding, and unwavering support throughout this long and challenging journey.*

Abstract

This study explores the integration of the Gurson-Tvergaard-Needleman (GTN) micromechanical damage model as a promising alternative to traditional forming limit curves by assessment of the formability in a deep drawing process. The success of the deep drawing process depends mainly on the material characterization. The sheet metal used in this thesis work is DC06EK. The mechanical characterization of this sheet metal was first the subject of a characterization of anisotropic behavior and then to isotropic and anisotropic plastic yield criteria from tensile tests on a specimen with a constant cross-section. Then, to characterize the GTN damage model and a hardening law, a new inverse identification strategy was proposed with a tensile test on a specimen with a variable (notched) cross-section. This strategy entails using both global and local observables, such as force and plastic strain, in two distinct zones within the tensile test specimen: a localization of deformation in one zone and the stagnation of deformation in another zone of the specimen with the variable cross-section indicates the moment of necking onset. The inverse identification was performed on a pseudo-experimental database to validate and test the reliability of the used algorithm considering three cases: the first one using only the force as a global observable, the second case adding a local observable, which is the plastic strain at the center of the specimen where rupture occurs, and the third case adding the plastic strain stagnation in a shifted zone from the center. Next, the validated approach was similarly used on an experimental tensile test to identify the GTN damage model coupled with hardening law parameters. The inverse identification process demonstrated good agreement between experimental and numerical results, emphasizing the importance of combining global and local observables for accurate parameter determination. In the second step, the identified parameters of the GTN damage model coupled with the hardening law were implemented into a numerical simulation of an industrial deep drawing application. This application concerns the deep drawing of a wheelbarrow tray. The findings demonstrated that the GTN damage model can significantly influence the prediction of wrinkling defects and accurately predict the zone and moment of necking onset, while traditional forming limit curves indicate the presence or absence of rupture, the case which could not be obtained via the GTN model.

Keywords: Anisotropy, Deep drawing, Formability, GTN damage model, Inverse identification, Numerical simulation, Wheelbarrow tray.

Résumé

Cette étude explore l'intégration du modèle d'endommagement micromécanique Gurson-Tvergaard-Needleman (GTN) comme alternative prometteuse aux courbes limites de formage traditionnelles par l'évaluation de la formabilité dans un procédé d'emboutissage profond. Le succès du procédé d'emboutissage profond dépend principalement de la caractérisation du matériau. La tôle métallique utilisée dans ce travail de thèse est le DC06EK. La caractérisation mécanique de cette tôle a d'abord fait l'objet d'une caractérisation du comportement anisotrope puis à des critères de plasticité isotropes et anisotropes à partir d'essais de traction sur une éprouvette de section constante. Ensuite, pour caractériser le modèle d'endommagement GTN et une loi d'écrouissage, une nouvelle stratégie d'identification inverse a été proposée avec un essai de traction sur une éprouvette de section variable (entaillée). Cette stratégie consiste à utiliser à la fois des observables globaux et locaux, tels que la force et la déformation plastique, dans deux zones distinctes au sein de l'éprouvette de traction : une localisation des déformations dans une zone et la stagnation des déformations dans une autre zone de l'éprouvette à section variable indiquent le moment de l'apparition de la striction. L'identification inverse a été réalisée sur une base de données pseudo-expérimentale pour valider et tester la fiabilité de l'algorithme utilisé en considérant trois cas : le premier utilisant uniquement la force comme observable globale, le deuxième cas ajoutant un observable local, qui est la déformation plastique au centre de l'éprouvette où la rupture se produit, et le troisième cas ajoutant la déformation plastique où il y a une stagnation de la déformation plastique dans une zone décalée par rapport au centre. Ensuite, l'approche validée a été utilisée de manière similaire sur un essai de traction expérimental pour identifier les paramètres du modèle d'endommagement GTN couplé à la loi d'écrouissage. La procédure d'identification inverse a démontré une bonne concordance entre les résultats expérimentaux et numériques, soulignant l'importance de combiner les observables globales et locales pour une détermination précise des paramètres. Dans la deuxième étape, les paramètres identifiés du modèle d'endommagement GTN couplés à la loi d'écrouissage ont été implémentés dans une simulation numérique d'une application industrielle d'emboutissage profond. Cette application concerne l'emboutissage d'une caisse de brouette. Les résultats ont démontré que le modèle d'endommagement GTN peut influencer de manière significative la prédiction des défauts de plissement et prédire avec précision la zone et le moment de l'apparition de la striction, tandis que les courbes limites de formage traditionnelles indiquent la présence ou l'absence de rupture, le cas qui n'a pas pu être obtenu via le modèle GTN.

Mots-clés : Anisotropie, Emboutissage, Formabilité, Modèle d'endommagement GTN, Identification inverse, Simulation numérique, Caisse de la brouette.

ملخص

تتناول هذه الدراسة دمج نموذج التلف الميكانيكي الدقيق لغورسون-تفيرغارد- نيدلمان (GTN) كبديل للمنحنيات التقليدية لحد التشكيل من خلال تقييم قابلية التشكيل في عملية التشكيل العميق. يعتمد نجاح عملية التشكيل العميق بشكل أساسي على توصيف المواد .الصفيحة المعدنية المستخدمة في هده الأطروحة هي من الفولاذ المدلفن على البارد "DC06EK". بداية التوصيف الميكانيكي لهذه الصفيحة المعدنية كان موضوعًا لتوصيف السلوك المتباين (anisotropy) أولاً ثم تحديد المعايير البلاستيكية للأنسوتروبي من خلال اختبارات الشد على عينة ذات مقطع عرضي ثابت .بعد ذلك، لتوصيف نموذج التلف GTN وقانون التصلب، تم اقتراح جديد لاستراتيجية التطابق العكسي مع اختبار الشد على عينة ذات مقطع عرضي متغير. تتضمن هذه الاستراتيجية استخدام كل من الملاحظات الكلية و المَوضِعِية، مثل القوة و التشوه البلاستيكي في منطقتين متميزتين داخل عينة اختبار الشد: تحديد موقع زيادة التشوه في منطقة و ركود التشوه في منطقة أخرى من العينة ذو مقطع عرضي متغير يشير إلى لحظة بداية التمزق. تم إجراء التطابق العكسي على قاعدة بيانات شبه تجريبية للتحقق من صحة واختبار موثوقية الخوارزمية المستخدمة مع مراعاة ثلاث حالات: الأولى باستخدام القوة فقط كملاحظة كلية، والحالة الثانية بإضافة ملاحظة موضعية، وهي التشوه البلاستيكي في مركز العينة حيث يحدث التمزق، والحالة الثالثة بإضافة التشوه البلاستيكي في منطقة أخرى من المركز. بعد ذلك، تم استخدام التطابق العكسي المعتمد على نحو مماثل في اختبار الشد التجريبي لتحديد معلمات نموذج التلف GTN مقترنًا بقانون التصلب. أظهرت عملية التطابق العكسي اتفاقًا جيدًا بين النتائج التجريبية والمحاكات العددية، مما يؤكد على أهمية الجمع بين الملاحظات الكلية و المَوضِعِية لتحديد المعلمات بدقة. في الخطوة الثانية، تم إدراج المعلمات المعرفة لنموذج التلف GTN مقترنة بقانون التصلب في محاكاة عددية لتطبيق التشكيل العميق الصناعي. يتعلق هذا التطبيق بالتشكيل العميق لصينية عربة اليد. أظهرت النتائج أن نموذج التلف GTN يمكن أن يؤثر بشكل كبير على التنبؤ بعيوب التجعد والتنبؤ بدقة بمنطقة ولحظة بداية التمزق، في حين تشير منحنيات حد التشكيل التقليدية إلى وجود أو عدم وجود تمزق، وهي الحالة التي لا يمكن الحصول عليها من خلال نموذج التلف GTN .

الكلمات المفتاحية: التباين، التشكيل العميق، قابلية التشكيل، نموذج التلفGTN ، التطابق العكسي، المحاكاة العددية، صينية عربة اليد.

Table of Contents

List of Figures

List of Tables

Nomenclature

A	Hardening parameter	[-]
b, b_0	Final and initial width	[mm]
f^*	Modified porosity	[-]
f_0	Initial porosity	[-]
f_C	Critical porosity	[-]
f_F	Porosity at final fracture	[-]
F_g	Growth function	[-]
F_n	Nucleation function	[-]
${f_U}^*$	The ultimate value of porosity	[-]
F, G, H, L, M, N	Hill 48 parameters	[-]
H	Hardening parameters	[-]
K	Strength coefficient (consistency)	[-]
m	Exponent related to crystallographic structure	[-]
n	Hardening exponent	[-]
q_1, q_2, q_3	Constitutive parameters	[-]
Q	Cost function	[-]
r	Lankford coefficient	[-]
r_0, r_{45}, r_{90}	Lankford coefficient at 0°, 45°, and 90°	[-]
r_n, R	Normal anisotropy	[-]
S_N	Standard deviation	[-]
t, t_0	Final and initial thickness	[mm]
α, β	Hardening law coupling parameters	[-]
η	Triaxiality	[-]
δ	Coalescence acceleration	[-]
Δ_r	Planar anisotropy	[-]
ε_2	Longitudinal principal strain (deformation in width)	[%]
ε_3	Transverse principal strain (deformation in thickness)	[%]
ε_N	Mean strain	[%]
ε^p	Plastic strain	[%]
ε	Strain	[%]
$\dot{\varepsilon}^p_{kk}$	The trace of the macroscopic strain rates tensor	[%]
θ	Rolling direction (angle)	[°]
$\bar{\sigma}$	Equivalent Stress	[MPa]
$\sigma_1, \sigma_2, \sigma_3$	Principal stresses	[MPa]
σ_{ij}	Stress tensor components	[MPa]
σ_m	Mean hydrostatic stress	[MPa]
σ_s	Saturation stress	[MPa]
σ_y	Yielding stress	[MPa]

Abbreviations

ABS	Acrylonitrile Butadiene Styrene
ASTM	American Society for Testing and Materials
BHP	Blank Holder Pressure
CCD	Charge-Coupled Device camera
CDM	Continuum Damage Mechanics
DDP	Deep Drawing Process
DIC	Digital Image Correlation
DP	Dual Phase Steel
EIMS	Enterprise Industrielle de Matériel Sanitaire (Industrial Company of Sanitary Equipment)
FE	Finite Element
FLCs	Forming Limit Curves
FLDs	Forming Limit Diagrams
GTN	Gurson-Tvergaard-Needleman model
HSLA	High-Strength Low-Alloy Steel
HSS	High-Strength Steels
IA	Inverse Analysis
IDDRG	International Deep Drawing Research Group
IF	Interstitial Free Steel
IM	Inverse Method
ISO	International Organization for Standardization
MSE	Mean Square Error
ND	Normal direction
PEEQ	Equivalent Plastic Strain
RD	Rolling direction
RMSE	Root Mean Square Error
RSM	Response Surface Methodology
TD	Transverse direction
VVF	Void Volume Fraction at Total Failure
VVFN	Void Volume Fraction due to Nucleation
WBT	Wheelbarrow Tray

General Introduction

The deep drawing process (DDP) is one of the most important sheet metal forming processes and plays an essential role in various industrial applications, particularly in the automotive and sanitary sectors. EIMS (Entreprise Industrielle de Matériel Sanitaire), which serves as the focal point of this thesis work, is a leading manufacturing company specializing in the production of a diverse range of products, particularly those manufactured by DDP. Its portfolio includes various sanitary and industrial components. Recently, EIMS has pursued strategic expansion by offering subcontracting services to the automotive industry (Fiat and Mercedes), focusing on deep-drawn parts such as automotive body components. This expansion is supported by the adoption of high-performance sheet materials, such as DC06EK steel, known for its excellent formability and adaptability in multiple applications.

Despite its importance, the DDP presents significant challenges in numerical simulation due to its inherent complexity. Accurately modeling the anisotropic behavior of sheet metals, selecting appropriate hardening laws, predicting formability, and integrating advanced damage models such as the Gurson-Tvergaard-Needleman (GTN) model remain major concerns. These challenges are important to ensuring the reliability and efficiency of the process, especially in predicting and preventing common defects such as surface defect, springback, wrinkling, necking, and rupture, which can compromise product quality of the final product.

Traditional forming limit curves (FLCs) have long been used at the macromechanical scale to characterize formability and predict defects in sheet metal forming. However, obtaining FLCs experimentally involves costly biaxial testing. To address these limitations, the GTN micromechanical damage model has emerged as a promising alternative, offering a more detailed understanding of material damage mechanisms. The GTN model captures localized deformation and rupture initiation with high accuracy by considering three fundamental damage stages: void nucleation, growth, and coalescence. This makes it a valuable tool for evaluating formability limits at the micromechanical scale, particularly in industrial deep drawing applications.

In the context of deep drawing, numerical simulation plays a crucial role in virtual manufacturing. Accurate simulations rely heavily on the constitutive models used to describe the mechanical behavior of sheet metals. Beyond plastic yield criteria and hardening laws, incorporating the GTN damage model into finite element analysis enables more precise formability predictions. The challenge lies in determining the parameters of the GTN model, which are typically identified through inverse analysis methods. Modern approaches integrate material damage into constitutive behavior laws, resulting in coupled models that enhance predictive accuracy.

This thesis aims to advance material characterization and inverse identification techniques while integrating them into industrial applications. The proposed methods offer a reliable framework for rupture prediction and process optimization in deep drawing. The thesis is then structured into three chapters:

The 1st chapter provides a bibliographic study, beginning with an overview of the EIMS company, its operations, and the range of products it manufactures through deep drawing. It also explores EIMS's strategic expansion into automotive subcontracting for manufacturing deep-drawn components like automotive body parts. The chapter further explores the properties, chemical composition, designation and applications of sheet materials used at EIMS, as well as the challenges in simulating the deep drawing process. Topics such as anisotropic yield criteria, hardening laws, formability, and the GTN damage model are addressed. Additionally, it includes a comprehensive literature review on determining GTN model parameters through inverse analysis, establishing a foundation for subsequent research.

The mechanical characterization of the choice of DC06EK sheet metal was the subject of the 2nd chapter. The latter starts with a characterization of anisotropic behavior and then to isotropic and anisotropic plastic yield criteria. Then, it focuses on investigating and validating a novel inverse identification strategy for coupled GTN damage and hardening law parameters. The strategy is first tested using a pseudo-experimental database to evaluate its robustness and reliability, then applied to experimental tensile test data to identify material parameters. Three scenarios are explored: (1) using only global observables (e.g., tensile force), (2) incorporating a local

observable (plastic strain in the rupture zone), and (3) adding another local observable where plastic strain stagnation occurs.

The final chapter applies the GTN model coupled with the hardening law parameters, identified in the 2nd chapter, to simulate an industrial DDP of a product. Before focusing on a specific case study, a presentation of projects conducted on different products manufactured by deep drawing at EIMS company. Among these, the wheelbarrow tray (WBT) was selected for this study due to its relative simplicity. A numerical simulation was then conducted using real industrial parameters, and the results were validated against thickness measurements obtained with an ultrasonic measuring device. Additionally, triaxiality cartographies and deformation modes of the sheet metal were analyzed. At the end, the integration of the GTN micromechanical damage model is investigated as a promising alternative to traditional FLCs by assessment of the formability in deep drawing of WBT.

Chapter 1. Bibliographic study

1.1. Introduction

The DDP is intensively used at EIMS company to manufacture a variety of sanitary and industrial products. This company is also looking to expand its production to the automotive sector by subcontracting with major companies: Fiat and Mercedes, focusing on deep-drawn components such as automotive body parts. The problems generally encountered in EIMS are the occurrence of rupture and wrinkling. The final objective is to propose a simulation of a reliable deep drawing operation capable of precisely defining the optimal conditions of use of this process in order to avoid the above-mentioned defects. However, the use of the numerical approach requires a good understanding of the constitutive laws and of the formability of the sheet metal material. Consequently, this chapter begins with a brief overview of EIMS and the sheet materials used in its production. Following this, a detailed bibliographic review is presented, covering the following key topics:

- Deep drawing process;
- EIMS products manufactured by deep drawing and forming defects;
- Sheet materials used in EIMS and in other applications;
- Challenges associated with numerical simulation of the DDP;
- Constitutive laws (work hardening law and isotropic and anisotropic yield criteria);
- FLCs as a tool to evaluate defects like necking, rupture, and wrinkling in deep-drawn parts;
- Introduction to the GTN damage model, accompanied by a comprehensive literature review on inverse identification and GTN damage model parameters determination.

1.2. Overview of EIMS Company

The "Industrial Company of Sanitary Equipment", called "In French: Enterprise Industrielle de Matériel Sanitaire (EIMS)" is an Algerian economic public company and a subsidiary of "Holding Elec El Djazair". Based in Miliana, wilaya of Aïn-Defla, Algeria, EIMS is recognized as one of the largest industrial enterprises in the country, playing a

vital role in driving the national economy, particularly in the sectors of metal and polymers transformation, and surface coating providing several products (Figure 1-1). With 44 years of experience, the company has developed extensive multidisciplinary expertise in deep drawing, folding, cutting, thermoforming, and enameling [1].

Figure 1-1 : Manufactured products at EIMS Company [1].

The following are the three main categories of the most commonly utilized mechanical manufacturing processes:

Figure 1-2 : Deep drawing press [1].

Deep drawing process (Figure 1-2): This process produces high-quality semi-finished products. The equipment includes presses specifically designed to handle large sheet metal pieces, ranging from 1 m × 0.5 m to 2 m × 1.5 m, with powerful deep drawing

presses ranging from 315 to 1600 tons. EIMS has five double-effect hydraulic presses with capacities of 315, 500, 600, and 1600 tons, made by the German brand MULLER. These presses can be operated individually or in a line through a transfer system.

Enameling process (Figure 1-3): EIMS has significant capacity for enamel application, performed manually using pneumatic spray guns. This allows for enameling parts of all sizes and shapes. The company has a high-capacity radiant enamel furnace (6000 kg/hour at 800°C) and an enameling line automatically fed by a conveyor system. It consists of four steps: cleaning, Mass coating, baking, and cover-coat enameling.

Figure 1-3 : Enameling workshop [2].

Thermoforming process (Figure 1-4): Reinforced polymer bathtubs are manufactured using this process. The used polymer is Acrylonitrile Butadiene Styrene (ABS). After thermoforming of the bathtub, it undergoes a polyurethane reinforcement process, involving the application of environmentally friendly polyurethane foam to strengthen the surface.

Figure 1-4 : Thermoforming workshop.

EIMS company aims to expand its activities by offering subcontracting services in the fields of the automotive sector. The targeted products primarily include deep-drawn parts, particularly components of automotive bodywork. Following consultations with automotive sector operators, such as the military company manufacturing Mercedes vehicles and FIAT Algeria, several issues need to be addressed, as:

- 3D measurements of different parts of components of automotive bodywork, designed to be manufactured.
- Generating different tool geometries (punch, die, and blank holder) through the option mold.
- Manufacturing the different tools.
- Numerical simulation of the deep drawing process for multiple parts in order to fix the operating conditions and the DDP parameters to avoid the appearance of mentioned defects (rupture, wrinkling) and other ones such as springback and surface defects.
- Make in service a production line for deep drawing, folding, and cutting processes.

In this thesis work, we are interested in the deep drawing process.

1.3. Deep drawing process

Deep drawing is a manufacturing technique used to transform a sheet metal into part with varying levels of complexity without removing material. This technique involves plastically deforming a metal delivered in sheet into the desired shape at room temperature. Generally, deep drawing operation is performed using mechanical or hydraulic presses, equipped with specialized tooling that includes a punch, a die, and a blank holder. The (sheet metal) blank may be circular, rectangular, or have a more complex shape [3]. During the deep drawing operation, the blank flow is controlled by the blank holder pressure and the lubricant [2]. The blank is drawn out of the blank holder-die region and is subjected to both compressive and tensile stresses with no intentional change in the blank's thickness. The principle of deep drawing is schematically shown in Figure 1-5.

This process is commonly used in the EIMS company, and in other various industries, particularly in aeronautics and the automotive sector.

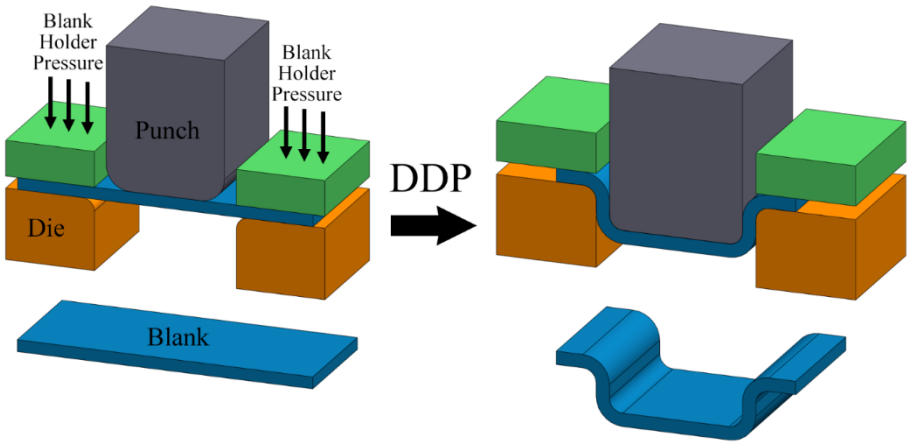

Figure 1-5 : Schematic representation of deep drawing process.

1.4. Deep-Drawn Products and Forming Defects at EIMS

EIMS is specialized in the production and marketing of sanitary products in enameled steel and stainless steel. The company manufactures and commercializes a range of sanitary articles with various dimensions and types. These products include [2]:

Sanitary products in enameled steel and stainless steel:

- Bathtubs: Available in three sizes – 1.70 m × 0.70 m, 1.60 m × 0.70 m, and 1.40 m × 0.70 m.
- Single-bowl kitchen sinks: Measuring 1.00 m × 0.60 m.
- Double-bowl kitchen sinks: With dimensions of 1.20 m × 0.50 m.
- Washbasins: Offered in two sizes – 0.60 m × 0.50 m and 1.20 m × 0.60 m.
- Shower Trays: Sized at 0.70 m × 0.70 m.

Household appliances and other products:

- Wheelbarrow.
- Natural gas heater 9000 kcal.
- Electronic weighing scale.
- Flat two-burner enameled steel stove.
- Light pole reflector.
- Office ceiling light.
- Light pole caps.

In the manufacture of the above products by deep drawing, there are two major problems: rupture and wrinkling defects, as represented in Figure 1-6. Minimizing rejected products due to these two defects is a desired goal of the company.

Figure 1-6 : Deep drawing defects: Wrinkling (a,b), Rupture (c,d).

1.5. Sheet materials used in EIMS and in other applications

Generally, steel and aluminum alloys are the mainly used materials in sheet metal industries. The growing trend toward using lightweight metals is well demonstrated by the multi-material concept shown in Figure 1-7. In this design approach, over two-thirds of the body-in-white is constructed from various aluminum alloys, including wrought sheets, extruded profiles, and castings, while 31% consists of high-strength steels (HSS) [4]. The base of HSS is low carbon steel, or referred to as mild steel. This material can be obtained by cold or hot rolled process [3,5].

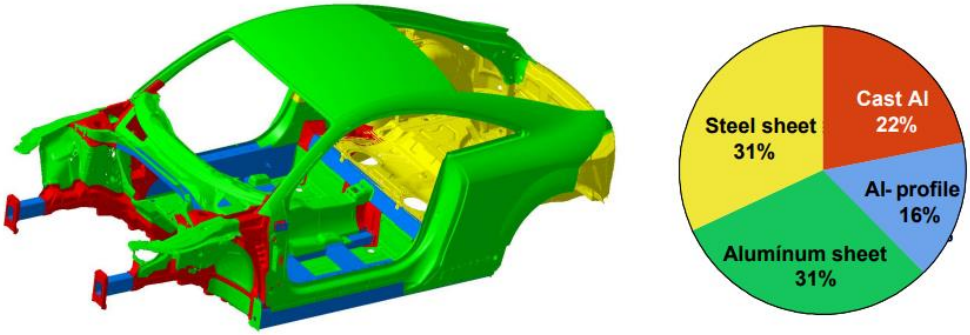

Figure 1-7 : The multi-material car concept in car body manufacturing [4] .

Based on our literature review and Figure 1-7, cold-rolled steels of the DC0"x" series have been the most widely used materials in automotive manufacturing for decades. Despite their relatively low strength, these steels offer excellent formability, particularly in terms of elongation properties, as illustrated in Figure 1-8, making them an ideal solution for various applications [6].

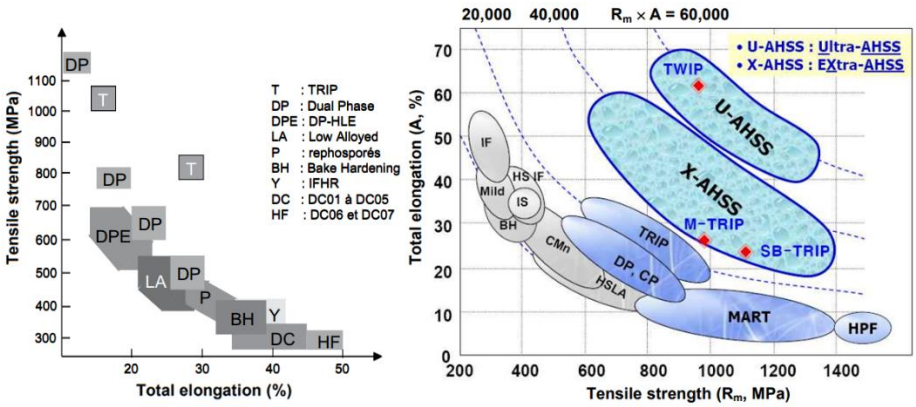

Figure 1-8 : Tensile strength vs. total elongation for various steel grades [3,4]

Additionally, Figure 1-9 highlights the estimated weight reduction potential of different steel grades and aluminum alloys, further emphasizing the versatility of these materials in lightweight design.

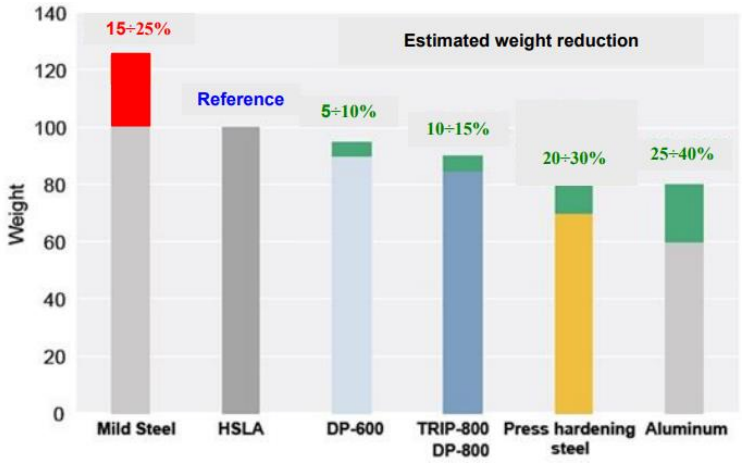

Figure 1-9 : Weight reduction potential of various high strength materials in car body manufacturing [6].

Table 1-1: Steel grades sheet materials used in the numerical simulation of different sheet metal forming applications.

Material	FE simulation	Reference
Aluminum alloy (AA5182-O)	Deep drawing of a cylindrical cup	R. Amaral et al. [7]
Metallic sheet AA6016-T4	Deep drawing of a rectangular box.	A. Kami et al. [8]
DC04 steel	Deep drawing process	S. Laboubi et al. [9]
DC06 steel	Deep drawing process of a bathtub	A. Hadj Amar e al [10]
DC06 steel	Deep drawing process of a wheelbarrow tray (WBT)	A. Belguebli et al. [11]
Interstitial free steel (IF) sheet	Single Point incremental forming (SPIF)	S. More e al. [12]
Cu-0.1Fe cooper alloy	micro-single-point incremental forming (µ-SPIF)	K. Belouettar et al. [13]
DP600	Blanking process	P. J. Zhao et al. [14]
High Strength Low Alloy Steel (HSLA)		M. Achouri et al. [15]
Carbon Steel		R. Hambli et al. [16]
Steels (DD13, X6Cr17 grades)		Rachik et al. [17]
Mild steel XES		Lemiale et al. [18]
FeSi (3wt.%) steel		Marouani et al. [19]

Table 1-1 provides an overview of previous research studies that used numerical simulation to investigate sheet metals commonly used in deep drawing applications. These studies confirm that mild steels of the DC0"x" series are the most widely used sheets in industries such as automotive manufacturing, household appliances, and sanitary equipment production.

According to the EN 10130 standard (April 2007), six grades of mild steel are available, as summarized in Table 1-2 [3]. At EIMS, DC0"x" series cold-rolled steels are extensively employed in the deep drawing process. The specific grade of steel used depends on the requirements of the process whether it involves standard deep drawing, extra-deep drawing, or applications requiring high formability to accommodate significant plastic deformation.

Table 1-2: Mechanical properties of different DC grades and their application [3].

Grade	Re_{max} (MPa)	Rm (MPa)	A (%) mini
DC01	270	270-390	30
DC03	220	270-350	36
DC04	190	270-350	38
DC05	240	270-370	34
DC06	210	270-350	38
DC07	190	270-350	38

Enamel steel sheets can be available in many grades or specifications. The EN 10209 standard defines six grades: three for conventional enameling (index EK) and three for direct enameling (index ED) [3]. The grades for direct enameling, DC03ED and DC04ED, are decarburized in coils. They have very pure grain joints, which can make them somewhat fragile in areas with very tight bends.

Table 1-3: Mechanical properties of different DC grades and their application [3].

Grade	$Re_{0,2}$ (MPa)	R_m (MPa)	A_{80} mini (%)	r_{90} mini
DC01EK	270	270-390	30	-
DC04EK	220	270-350	36	-
DC06EK	190	270-350	38	1,6
DC03ED	240	270-370	34	-
DC04ED	210	270-350	38	-
DC06ED	190	270-350	38	1,6

For the numerical simulations conducted in this study, we selected the DC06EK metal sheet, which is one of the most commonly used materials at EIMS for deep drawing operations. The designation of this sheet steel is as follows [3]:

- D: steel for cold forming;
- C: Cold-Rolled steel;
- 06 is the steel grade as mentioned in Table 1-2 mostly used in deep drawing
- EK for conventional enameling.

Table 1-4: Chemical composisition of DCEK steel sheet.

Element	Fe	C	S	N	Mn	P	Si	Al	T_i
Annex 1	balance	0.005	0.016	0.0095	0.195	0.010	0.008	0.060	0.100

Table 1-4 provides the chemical composition of the DC06EK steel sheet, highlighting the presence of various alloying elements that contribute to its mechanical properties and performance. One key observation is the low carbon (C) content (0.005%), which plays a crucial role in enhancing the steel's plastic deformation capabilities. This low carbon percentage reduces the formation of carbides, ensuring better formability, which is particularly beneficial in applications requiring deep drawing and high ductility.

Additionally, the presence of manganese (Mn) at 0.195% helps improve the steel's strength and hardenability while maintaining good toughness. The low phosphorus (P) and sulfur (S) contents (0.010% and 0.016%, respectively) contribute to improved weldability and reduced brittleness, making the material more reliable for structural applications.

Moreover, the silicon (Si) and titanium (Ti) contents (0.008% and 0.100%, respectively) indicate their role as grain refiners. Titanium, in particular, is known for stabilizing the microstructure by forming fine precipitates, which improves strength while maintaining ductility. Similarly, aluminum (Al) at 0.060% contributes to deoxidation and further refines grain size, leading to improved mechanical performance.

1.6. Challenges of numerical simulation of the DDP

The EIMS company has as a specific goal to minimize the rejected products. To respond to this need, a numerical simulation of deep drawing process with real parameters used in EIMS company will be performed in this study.

Nowadays, numerical analysis based on the finite element method provides a better understanding of deep drawing processes [20], allowing for the prediction of forming defects [21,22] and providing information on the deformed shape, stress and strain distribution, and punch loading [23–25]. This technique now offers significant economic benefits in terms of time and cost savings.

To model a deep drawing operation, including geometries, tool actions and speeds, temperature, etc., it is necessary to incorporate the following components into a numerical simulation software [26,27]:

- the elastoplastic behavior laws describing the mechanical behavior of the sheet,
- a friction law expressing the sheet-tool contacts, whether dry or lubricated,
- and a forming limit curve or damage model for predicting different defects (wrinkling, necking onset and rupture) during the forming process.

The primary aim of this thesis is to offer a simulation of a DDP with real operating parameters. This reliable predictive tool is capable of precisely defining the optimal conditions for using this process. However, the use of the numerical approach requires a good understanding of the material behavior laws of the sheet metal and a proper assessment of its formability. Predictive models exist, but their accuracy is directly linked to the identification of the material's mechanical behavior. This is achieved through rheological tests that can reproduce the specific phenomena of forming processes.

After analyzing the aforementioned numerical models in paragraph § 3.2, it was found that none of them have used a damage model in an industrial application. Therefore, in the following sections, in addition to the presentation of hardening laws, anisotropic plasticity criteria, and formability, a particular focus will be placed on the GTN damage model, which is primarily used in predicting necking/rupture in sheet metal forming, as opposed to predicting necking using FLCs.

1.7. Sheet material behavior

1.7.1. Plastic yield Criteria

The modeling of the plastic behavior of sheet metals requires the use of a yield criterion and hardening laws to enable the study of forming processes through numerical simulation. These criteria are described by a mathematical function called the yield function or plastic flow surface, which represents the boundary between the elastic and plastic domains for a material at a given moment. The yield criterion is thus defined based on the shape of the yield surface $f = 0$. It is generally determined by the difference between the equivalent stress $(\bar{\sigma})$ and the yield stress σ_y. Its equation can be written as follows [28]:

$$f(\sigma_{ij}, \varepsilon) = \overline{\sigma}(\sigma_{ij}) - \sigma_y(\overline{\varepsilon}) \quad 1\text{-}1$$

where σ_{ij} the components of the stress tensor, and σ_y the yielding stress.

This surface is governed by several conditions, including the case where the material exhibits elastic behavior when the function $f(\sigma_{ij}, \varepsilon) < 0$ and the case where the function $f(\sigma_{ij}, \varepsilon) = 0$, which corresponds to the yield point that defines the plastic flow surface [28].

1.7.1.1. Isotropic yield Criteria

Isotropic material refers to the material in which the mechanical properties are the same regardless the orientation of the rolling direction in the sheet metal.

In sheet metal forming, the surface of the sheet is typically used as the reference plane, with stress and strain definitions adapted accordingly. Direction 3 is oriented perpendicular to the sheet surface (the thickness direction), while Directions 1 and 2 lie parallel to the surface. This setup assumes that $\sigma_3 = 0$ (the plane stress condition), and the effective stress is described by equation 1-2 [29]:

$$\bar{\sigma} = \sqrt{\sigma_1^2 - \sigma_1\sigma_2 + \sigma_2^2} \quad 1\text{-}2$$

Usually, Von Mises criterion and Tresca are the most used for isotropic materials to define both yield function and elastic limit. In a plane stress scenario, graphical presentation of the yield function of both the Tresca criterion and the von Mises criterion are illustrated in Figure 1-10.

The lines within that illustration represent the yield locus, which defines the boundary for plastic deformation. When the stresses remain within this locus, no plastic deformation occurs; however, plastic deformation begins when the stress state reaches the boundary. If the material undergoes hardening, the yield locus changes shape due to the plastic deformation [29].

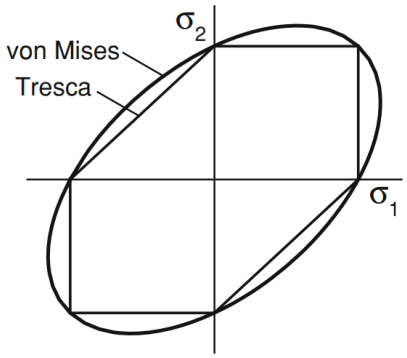

Figure 1-10 : Graphical presentation of the yield function of both Tresca and Von mises criterion.

1.7.1.2. Anisotropic yield Criteria

Anisotropic material refers to a material in which the mechanical properties are different in normal, transverse, and longitudinal directions [29]. In other words, the material's behavior depends on the orientation of the rolling direction.

Sheet metals destined for forming are generally obtained by rolling process which has many problems of plastic instability. The material changes at microstructural scale as well as the crystal orientation during rolling operation leads to create anisotropy. The anisotropy plastic behavior characterization of sheet metal uses the relations of Lankford's coefficient [30–32]. It is calculated by the deformation ratio of width to thickness of uniaxial tensile test specimen equation 1-3 [31,32].

$$r = \frac{\varepsilon_2}{\varepsilon_3} \qquad 1\text{-}3$$

Equation 1-3 can be written as follows:

$$r = \frac{ln\frac{b}{b_0}}{ln\frac{t}{t_0}} \qquad 1\text{-}4$$

where: b and b_0 the final and initial width of the specimen, while t and t_0 the final and initial thickness respectively.

By taking into account the volume incompressibility assumption ($\varepsilon_1 + \varepsilon_2 + \varepsilon_3 = 0$), the anisotropy coefficient (equation 1-3) can be written as:

$$r = -\frac{\varepsilon_2}{\varepsilon_1+\varepsilon_2} \quad 1\text{-}5$$

Thus equation 1-4 will be written as follows:

$$r = \frac{-ln\left(\frac{b}{b_0}\right)}{ln\left(\frac{l}{l_0}\right)+ln\left(\frac{b}{b_0}\right)} \quad 1\text{-}6$$

where: l and l_0 the final and initial gage length of the specimen. l_0 is specified by standards.

Therefore equation 1-6 can be expressed in the following form:

$$r = \frac{\left(ln\frac{b}{b_0}\right)}{ln\left(\frac{l_0 b_0}{l\ b}\right)} \quad 1\text{-}7$$

Considering a specimen cut in three different orientations in the plane of the metal sheet (0°, 45°, and 90° respectively). The corresponding r values for each orientation can be obtained, then the coefficient of normal anisotropy is calculated by the following formula:

$$r_n = -\frac{r_0+2r_{45}+r_{90}}{4} \quad 1\text{-}8$$

The variation of the normal anisotropy with the angle with respect to the rolling direction is known as planar anisotropy and given by the following expression:

$$\Delta r = -\frac{r_0+r_{90}-2r_{45}}{2} \quad 1\text{-}9$$

When $r \neq 1\ and\ \Delta r \neq 0$, we assume that the material exhibits either normal and planar anisotropy, while for ($r \neq 1\ and\ \Delta r = 0$), the material exhibits normal anisotropy, in contrast when $r_0 = r_{45} = r_{90} = 1\ or\ r = 1\ and\ \Delta r = 0$ it reduces the isotropic case [33].

In sheet metal forming the anisotropy can be considered through the Hill 48 criterion [31,32] equation 1-11, which is the extension of Von Mises criterion expressed, equation 1-10).

$$(\sigma_{11} - \sigma_{22})^2 + (\sigma_{22} - \sigma_{33})^2 + (\sigma_{33} - \sigma_{11})^2 + 6((\sigma_{12} + \sigma_{23} + \sigma_{13})^2) = 2{\sigma_0}^2 = 2{\overline{\sigma}_M}^2 \quad 1\text{-}10$$

$$2f(\sigma_{ij}) = F(\sigma_{22}-\sigma_{33})^2 + G(\sigma_{33}-\sigma_{11})^2 + H(\sigma_{11}-\sigma_{22})^2 + 2L\sigma_{23}^2 + 2M\sigma_{31}^2 + 2N\sigma_{12}^2 = 1 \quad 1\text{-}11$$

where: $\overline{\sigma_M}$ is the equivalent Von Mises stress, and $F, G, H, L, M, and\ N$ are anisotropy parameters.

These parameters can be written in function of the six yield stress ratios as follows [34]:

$$\begin{cases} F = \frac{1}{2}\left(\frac{1}{{R_{22}}^2} + \frac{1}{{R_{33}}^2} - \frac{1}{{R_{11}}^2}\right) \\ G = \frac{1}{2}\left(\frac{1}{{R_{11}}^2} + \frac{1}{{R_{33}}^2} - \frac{1}{{R_{22}}^2}\right) \\ H = \frac{1}{2}\left(\frac{1}{{R_{22}}^2} + \frac{1}{{R_{11}}^2} - \frac{1}{{R_{33}}^2}\right) \\ L = \frac{3}{2{R_{23}}^2} \\ M = \frac{3}{2{R_{13}}^2} \\ N = \frac{3}{2{R_{13}}^2} \end{cases} \quad 1\text{-}12$$

During the sheet metal forming process the material exhibits plane stress ($\sigma_{33} = \sigma_{31} = \sigma_{23} = 0$), thus, only four constants are remained to be determined and the Hill 48 yield criterion reduces to equation 1-13 [31,32,34]:

$$2f(\sigma_{ij}) = (G+H){\sigma_{11}}^2 - 2H\sigma_{11}\sigma_{22} + (H+F){\sigma_{22}}^2 + 2N\sigma_{12}^2 = 1 \quad 1\text{-}13$$

It can be formulated for a tensile test as a function of the applied stress σ_0 which depends on the solicitation direction and the orientation angle θ formed by the axes system and the rolling direction (Figure 1-11). So, we can write [34]:

$$f = \sigma_\theta \sqrt{(G+H)\cos(\theta)^4 + (F+H)\sin(\theta)^4 + 2(N-H)\cos(\theta)^2\sin(\theta)^2} - \sigma_0 \quad 1\text{-}14$$

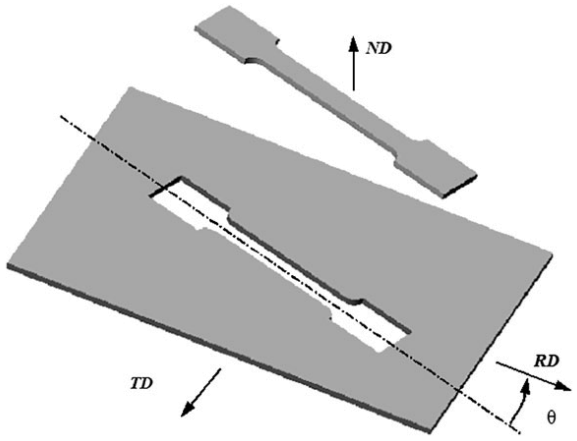

Figure 1-11 : Specimen orientation with respect to the rolling direction.

To determine the Hill's 48 anisotropy parameters, we can use Lankford anisotropy coefficient (r_θ) as a function of orientation angle θ, which is written as follows:

$$r_\theta = \frac{\dot{\varepsilon}_{yy}}{\dot{\varepsilon}_{zz}} \quad 1\text{-}15$$

At elastic limits, the yield stress is defined when $f = 0$, also σ_0 is the yield stress in the rolling direction (r_θ = 0°). Therefore, we deduct that $G + H = 1$ and the anisotropy coefficients as follows:

$$\begin{cases} F = \frac{r_0}{r_{90}(1+r_0)} \\ G = \frac{1}{(1+r_0)} \\ H = \frac{r_0}{(1+r_0)} \\ N = \frac{(r_0+r_{90})(1+2r_{45})}{2r_{90}(1+r_0)} \end{cases} \quad 1\text{-}16$$

$$\begin{cases} R_{22} = \sqrt{\frac{r_{90}(1+r_0)}{r_0(1+r_{90})}} \\ R_{33} = \sqrt{\frac{r_{90}(1+r_0)}{(r_{90}+r_0)}} \\ R_{12} = \sqrt{\frac{3r_{90}(1+r_0)}{(2r_{45}+1)(r_{90}+r_0)}} \end{cases} \quad 1\text{-}17$$

with: $R_{11} = R_{13} = R_{23} = 1$

1.7.1.3. Non-Quadratic yield Criteria

Von Mises and Hill 48 are popular for describing sheet metal behavior, their formulation quadratic does not always accurately represent the anisotropy of certain materials [35]. To investigate other modeling of anisotropic behavior, non-quadratic isotropic and anisotropic plasticity criteria were also evaluated, specifically the Hershey-Hosford and Logan-Hosford criteria. Their parameters can be identified from uniaxial tensile tests, shear tests or even equibiaxial tensile tests.

Hershey-Hosford Criterion

A non-quadratic isotropic criterion was proposed by Hershey in 1954 and Hosford in 1972 by introducing the "m" component which depends on the crystallographic structure of the material [36]. The yield function for this criterion is expressed in terms of the principal stresses as follows:

$$2\bar{\sigma}^m_{(\sigma_{ij})} = |\sigma_1 - \sigma_2|^m + |\sigma_3 - \sigma_1|^m + |\sigma_2 - \sigma_3|^m \quad 1\text{-}18$$

when $m = 2$, the yield surface resembles that of von Mises.

Logan-Hosford Criterion

A second particular anisotropic case (Logan-Hosford) of the Hill 48 criterion is used to better study the anisotropy of the DC06EK for the same values of the Hill 48. This criterion has the following form [37]:

$$\bar{\sigma}^{m}_{(\sigma_{ij})} = \frac{1}{1+R}(|\sigma_1|^m - |\sigma_2|^m) + \frac{R}{1+R}|\sigma_1 - \sigma_2|^m \quad 1\text{-}19$$

1.7.2. Hardening Laws

The transition between the plastic and elastic region is controlled by the plastic deformation when reaching critical values [32]. The variation of the stress in function of the plastic deformation is described by the hardening law. The selection of the suitable hardening law is essential for numerical modeling of the elastoplastic behavior of the material. In addition, the hardening law can be implemented into ABAQUS finite element software through a subroutine or directly by a table [28,33,38].

Various forms of isotropic hardening laws are available in the literature; hereinafter are the most used:

Hollomon law: This is the simplest law governed by equation 1-20

$$\sigma = K\varepsilon^{n} \quad 1\text{-}20$$

with K: The strength coefficient or the consistency and n: the strain hardening coefficient

To obtain these parameters, a linear transformation of the stress train curve should be made, after that the slope of the new curve define the strain hardening coefficient [28].

At very low strain level, the material behavior is not perfectly described because this law assumes plastic strain domination and it does not give any information about the elastic limit [28,39]. However, at high strain level it provides a good approximation [39].

Ludwik's Law: It is an extension of Hollomon law including additional term which is the initial yield stress σ_0 or the elastic limit (equation1-21). It does not give a good fit in case of large deformations because the slope is constant most of metals and σ_0 becomes negligeable [39,40], however it is suitable for material that exhibit a distinct elastic-to-plastic transition.

$$\sigma = \sigma_0 + K(\varepsilon^p)^n \quad 1\text{-}21$$

Swift's law: It provides a better fit to the experimental stress-strain curves than the Ludwick's law, it is given by equation 1-22:

$$\sigma = \sigma_0[1 + K(\varepsilon^p)]^n \quad 1\text{-}22$$

Both Voce and Hockett-Sherby, equation 1-23 and equation 1-24, respectively, introduced saturation parameters σ_s, called saturating hardening models, they are well-suited for accurately simulating tensile strain in the homogeneous deformation region. However, they tend to predict a premature decrease in strength just before the onset of necking in contrast with non-saturating laws (Hollomon, swift, and Ludwick) [41].

Voce's law

$$\sigma = \sigma_s - (\sigma_s - \sigma_0)\, exp(-A(\varepsilon_p)) \quad 1\text{-}23$$

Hockett-Sherby's law

$$\sigma = \sigma_s - (\sigma_s - \sigma_0)\, exp(-A(\varepsilon_p)^H) \quad 1\text{-}24$$

In the work of M. Djouabi et al [41], they determined the parameters for simple hardening laws (Swift, Voce, and Hockett-Sherby) by fitting the numerical curves with the experimental ones using the least square method. After that they combined those laws (Swift-Hockett-Sherby and Swift-Voce) (equation 1-25 and 1-26 respectively) to better describe the hardening behavior incorporating the initial yield stress σ_0 and the saturation stress σ_s. The coupling parameters (α and β) of the combined models were determined through the inverse method IM using modeFRONTIER software.

Swift-Hockett-Sherby's law

$$\sigma = (1-\beta)\left[\sigma_0 + K\left(\varepsilon_p\right)^n\right] + \beta\left[\sigma_s(\sigma_s - \sigma_0)\, exp\left(-\alpha\left(\varepsilon_p\right)\right)\right] \quad 1\text{-}25$$

Swift-Voce's law

$$\sigma = (1-\alpha)\left[\sigma_0 + K\left(\varepsilon_p\right)^n\right] + \alpha\left[\sigma_s - (\sigma_s - \sigma_0)\, exp\left(-\alpha\left(\varepsilon_p\right)^H\right)\right] \quad 1\text{-}26$$

1.7.3. Formability

The concept of evaluating the formability of materials was introduced by Keeler and Backofen [42] and Goodwin [43]. Generally, formability is defined as the ability of a material to undergo irreversible plastic deformation without the appearance of defects, either in the form of a macroscopic rupture or in the form of a localized necking [44].

According to the manufacturers, the products that contain those defects are rejected. These defects cause a waste of time and financial losses.

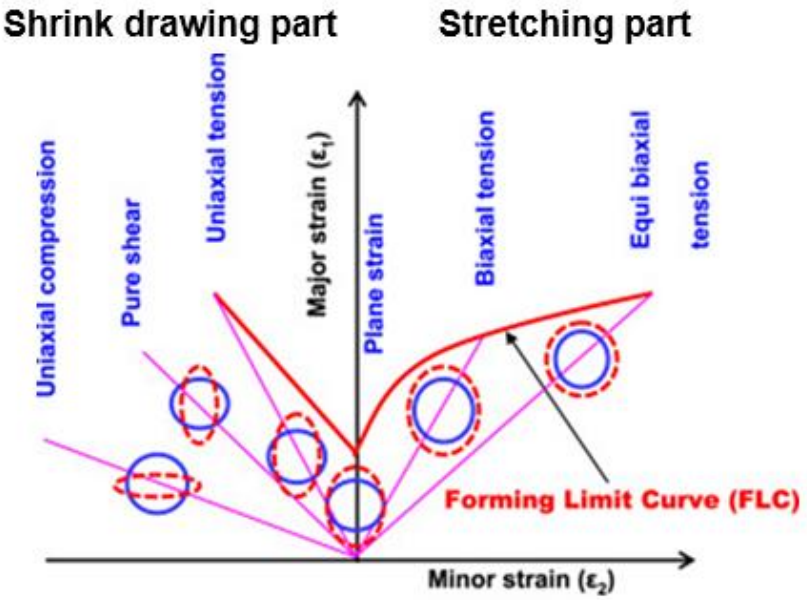

Figure 1-12 : Forming limit curve (FLC) and deformation modes [45].

In addition, the strain can be concentrated in unstable regions that exhibit thickness reduction; this is defined as the presence of necking onset. On the other hand, the variation of strain gradually stops as we move away from weak regions [46].

The FLCs are a graphical representation (Figure 1-12), that define the limit of formability for a given material by representing the minor and major strain in principal plane (Figure 1-12). FLCs bounds the deformation of the material. Above the curve necking/rupture occurs and under while below the curve it is safe.

1.7.3.1. Experimental and theoretical methods for determining FLCs

FLCs are essential tools in DDP, used to predict the onset of necking and eventual rupture [47–50]. In order to obtain the FLC representative of the formability of sheet metals, several experimental and theoretical works have been carried out to reproduce the different strain paths and to evaluate the appearance of localized necking.

Experimentally, different mechanical tests have been developed to determine the FLC. They vary between them by the type of test and the way of measuring deformations. These tests are illustrated in the Table 1-5.

Table 1-5: Different mechanical tests of biaxial solicitation to determine the FLC [38].

	FLC in shrink drawing part	FLC in stretching part	Variation of strain path	Dynamic tests	Tests under temperatures
Deep drawing test (Nakazima and Marciniak)	+ +	+ +	-	+	+ +
Bulge test	-	+ +	-	+ +	-
Biaxial tensile test	+	+	+ +	+ +	+ +

\- not suitable + poorly suitable + + well suitable

The experimental determination of FLCs requires expensive equipment for biaxial tests [27,51,52]. For this reason, many research trended to propose analytical and numerical methods to determine the FLCs. Keeler and Brazier [53,54] analytically developed a model to represent the FLC. This model is defined in terms of sheet thickness t_0 and the strain-hardening coefficient n to calculate the FLC for mild steels.

The key variable in the model is the location of the lowest point of the FLC, which is positioned along the plane deformation path and referred to as 'FLC.' According to this model, the FLC is determined as follows:

$$\begin{cases} FLC_0 = ln\left(\frac{n}{0.116}(0.2325 + 0.1413.t_0) + 1\right) \\ Stretching\ part\ of\ the\ FLC: \varepsilon_1 = FLC_0 - \varepsilon_2 \\ Shrink\ drawing\ part\ of\ the\ FLC: \varepsilon_1 = (FLC_0 + 1)(\varepsilon_2 + 1)^{0.5} - 1 \end{cases} \quad 1\text{-}27$$

1.7.3.2. Localized necking's determination methods for establishing FLCS

There are many ways to evaluate the level of deformation at which localized necking appears. However, the main issue lies in the simple fact that there is no rigorous definition of this stage, with each person interpreting it more or less in their own way.

To define what a FLC is, we have already described the American method known as the "Keeler method", which is based on visual and tactile detection, stating that it is likely the closest to industrial practice. However, several methods have been proposed for the localized necking determination, they are described as follows [3]:

Hecker Method

The Hecker method for determining the onset of necking [55] has been widely used in North America and provides results fairly close to industrial reality. The approach is as follows: on ruptured specimens subjected to different modes, the deformations of circles (or squares) near a fractured zone are measured. Each measured element is assigned to one of the following three categories (Figure 1-13-a):

- Ellipse A: Fractured (ε_1 is determined by the sum of the two halves).
- Ellipse B: Very close to the necking zone.
- Ellipse C: Not necked.

These points are plotted on a strain diagram, distinguishing them, for example (Figure 1-13-b), as follows:

- Fractured: Black.
- Very close to necking: Gray.
- Not necked: White.

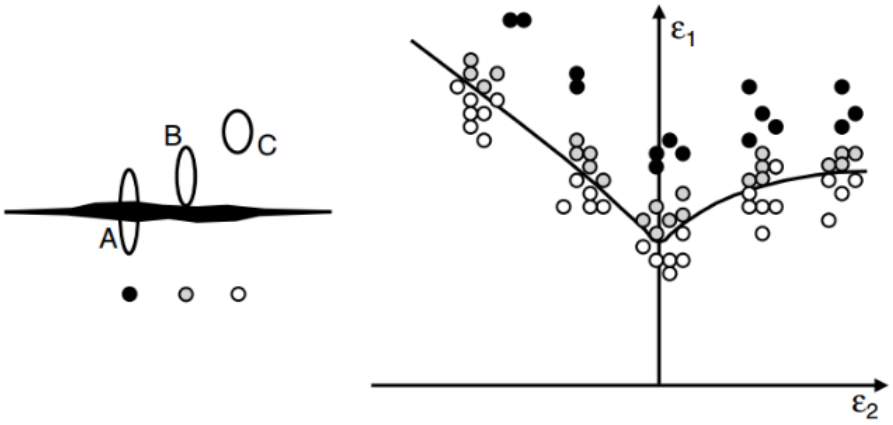

Figure 1-13 : Hecker method [3].

It is observed that a curve can be drawn between the points representing necking and those corresponding to non-necking. This curve represents the localized necking (FLC of the sheet metal, Figure 1-13-b). Furthermore, it is evident that the fracture FLC could just as easily be determined between the gray and black points.

Veerman Method

In 1971, Veerman, then at the steelmaker Hoogovens, described a graphical method for determining the onset of necking [56].

Test specimens are brought to various stages of deformation, for example, by stopping the testing machine at different stroke heights. At each stage, the deformation of the circles in the supposedly critical area of the specimen is measured. When the specimen fractures, the fractured circle is precisely identified (the fracture must occur at its center), and its deformations are compared to those of the two adjacent circles along the direction of principal deformation.

The adopted hypothesis, which is entirely justified, is that the three circles deform identically as long as there is no localized necking. However, when localized necking begins, the deformation of the central circle accelerates, while the deformation of the others halts.

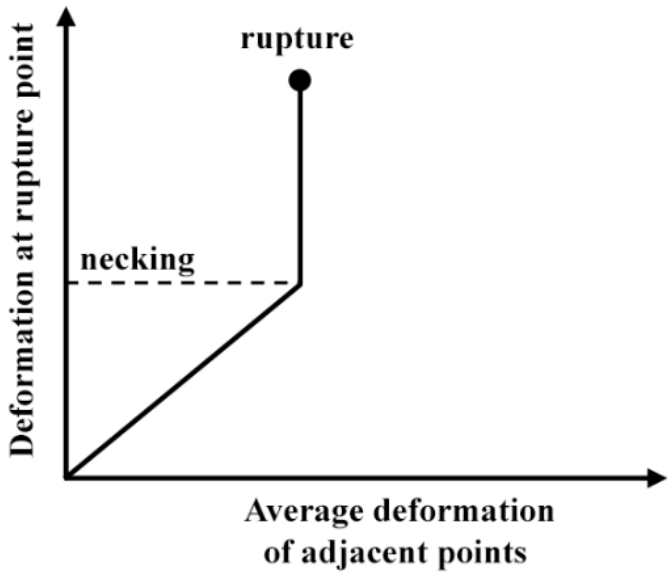

Figure 1-14 : Graphical representation of ruptured cercle and its adjacent [3].

The evolution of the deformation of the circle that will fracture is then plotted on a graph (ordinate) as a function of the average deformation of the two adjacent circles (abscissa) (Figure 1-14). The curve describing this evolution undergoes an inflection point when localized necking appears.

BRAGARD Method

The use of the Veerman method involves a tremendous amount of work. To address this drawback, a researcher from CRM, Bragard [57], developed a relatively simpler way to determine the onset of necking in 1972. Instead of applying multiple levels of deformation, as in the previous technique, only a single fractured specimen is required to find a point on the FLC (as in the Hecker method).

The deformation of all points surrounding the fracture in the direction of principal deformation is measured, thus providing access to the deformation gradient in this area. The guiding idea is that deformation was relatively homogeneous until the onset of localized necking. This corresponds to a curve in the shape of an inverted parabola, as shown in Figure 1-15.

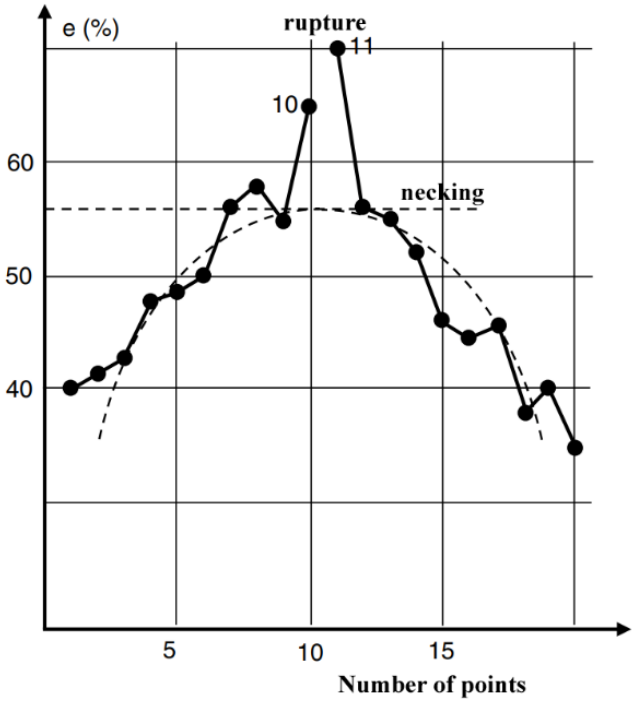

Figure 1-15 : Distribution of Deformations Around the Fracture and Extrapolation [3].

Extrapolating this curve is the main challenge, as it is only possible under certain well-defined conditions, which have been more or less standardized through extensive community studies by the IDDRG (International Deep Drawing Research Group), an organization dedicated to deep drawing research, established in 1957. The method standardized by this group is known as the Zurich Method No. 5, named after the conference held in Zurich where the method was officially recognized.

Since the advent of computer technology, the determination of the extrapolation has become more automated, making it less dependent on the operator. Appropriate algorithms have been developed by Vegter and his team at Corus, and these are now integrated into the ISO 12004-2 standard, which was mentioned earlier.

Velocity Method

The initial idea, presented in 1997, came from a team of researchers at the steelmaker Usinor [58]. It resulted from the clever use of advancements in electronics and computer science, incorporating four key features:

- The deformation of the sample during a Marciniak test is continuously filmed using a CCD camera.
- The grid of circles or squares is replaced by a speckle pattern.
- Deformation tracking is done in real-time using image correlation analysis software.
- The images are continuously recorded.

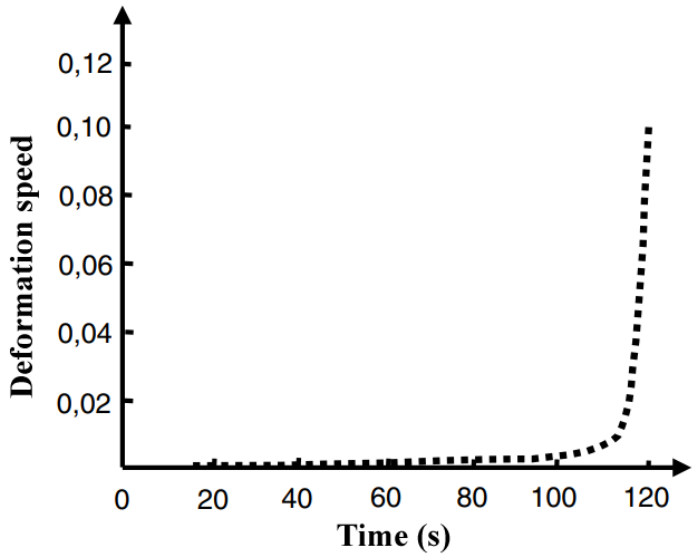

Figure 1-16 : Deformation Rate (deformation speed) as a Function of Time [3,59].

At the end of the test, the rupture location in the specimen is known, and the critical zone can be measured. It is then easy to "rewind" the deformation film and follow its local evolution. However, this was not the chosen criterion because it was found more useful to consider the evolution of the deformation rate. It increases significantly at the onset of necking, as shown in Figure 1-16. This method shares a similar principle with the Veerman method.

This is one of a fast and nearly automatic, highly sophisticated technique, and recent technological advancements have led to the emergence of several commercial products. Its efficiency can be further improved by considering the deformation evolution in the areas adjacent to the necking zone (while deformation accelerates in the necked region, it slows down outside of it).

1.8. GTN damage model

The experimental determination of FLCs requires expensive equipment for biaxial tests [27,51,52]. For this reason, many research trended to propose custom models to face the cost of these tests [60,61]. For this reason, as many researchers [62–65], we adopt to investigate the GTN damage model as an alternative to the FLCs to predict necking/rupture and the formability of the material.

In the last decade, the modeling of damage and rupture has been extensively investigated. Moreover, it allows for assessing the integrity of in-service structures when full-scale experiments are not available [66].Thus, the GTN damage model was proposed to evaluate the formability limits at the micromechanical scale [62–65]. It provides a better understanding of material damage mechanisms, allowing the capture of localized deformation and rupture initiation with high accuracy.

Over the past three decades, two major damage theories have been developed in the literature. The first theory is known as continuum damage mechanics (CDM). This theory assumes that the material is continuous; in another context, the hydrostatic pressure has no noticeable effect on the material's yield, and the material's volume does not change during plastic deformation. It is based on macro-damage characteristics such as notches, cracks, and elongation [67]. Failure is predicted through a damage accumulation criterion for uncoupled damage models [2–9], while for coupled damage models [68,69], a phenomenologically concluded damage evolution function is used.

The second theory is based on a physically motivated micromechanics approach combined with the mechanical process to link the materials' meso-structure evolution to their micromechanical behavior. This approach focuses on micro-void kinematics during plastic deformation within the material under different loading conditions [70].

The principle of volume invariance of macro-damage mechanics is no longer suitable for describing ductile fracture behavior caused by volume expansion of the material's micro-voids. As a result, Gurson analyzed the evolution of spherical voids within a cubic cell [62,71]. He derived a plastic yield potential function, considering the influences of void volume fraction (porosity) and hydrostatic pressure, forming the first porous metal plastic model. The Gurson model was developed considering the interaction between voids. The modified model, known as The Gurson-Tvergaard-Needleman (GTN) model, is a well-known damage model considering void nucleation, growth, and coalescence [65,71]. Figure 1-17 illustrates the evolution of damage mechanism from voids (or inclusions) to coalescence.

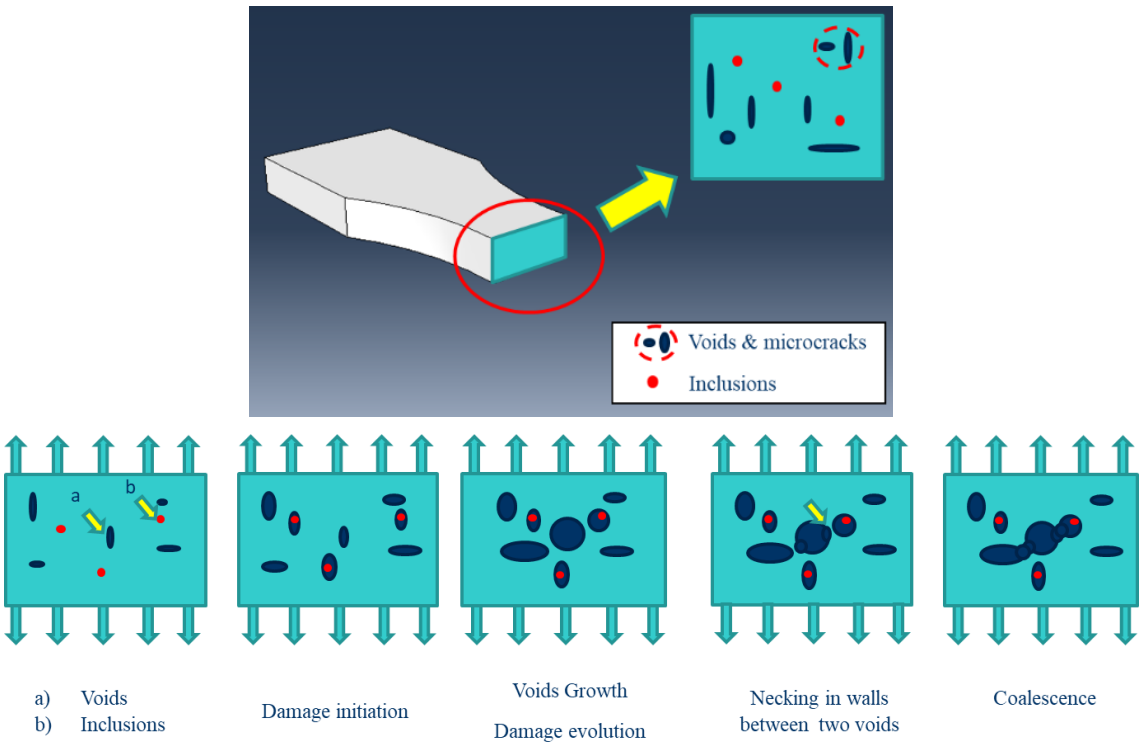

Figure 1-17 : Damage mechanisms.

The expression of the GTN model is written as follows:

$$\Phi(\sigma_{eq}, \sigma_y, f) = \frac{{\sigma_{eq}}^2}{{\sigma_y}^2} + 2q_1 \cosh\left(\frac{3}{2} q_2 \frac{\sigma_m}{\sigma_y}\right) - (1 + q_3 f^2) = 0 \qquad 1\text{-}28$$

where: σ_{eq} the equivalent Von Mises stress, σ_y the yield stress of the matrix, σ_m the hydrostatic stress, q_1, q_2, and q_3 Constitutive parameters, and f the porosity.

To accommodate the rapid softening of the material during the coalescence stage, Tvergaard and Needleman [65] introduced the *f* *(*f*) function in addition to the previous yielding criteria. The yield surface of the GTN model is expressed by the following equation:

$$\Phi\left(\sigma_{eq},\sigma_{y},f\right)=\frac{\sigma_{\mathrm{eq}}^{2}}{\overline{\sigma}^{2}}+2\mathrm{q}_{1}f^{*}\cosh\left(\frac{3}{2}q_{2}\frac{\sigma_{m}}{\overline{\sigma}}\right)-(1+q_{1}^{2}f^{*2})=0 \qquad 1\text{-}29$$

where: $\overline{\sigma}$ represents the equivalent tensile flow stress at the actual microscopic stress state in the matrix material, and f^{*} represents the modified porosity and it follows the law below:

$$f^{*}(f)=\begin{cases} f & if\ f\leq f_{c} \\ f_{c}+\delta(f-f_{c}) & if\ f_{c}<f<f_{f} \\ f_{U}^{*} & if\ f\geq f_{f} \end{cases} \qquad 1\text{-}30$$

with: $\delta=\frac{f_{U}{}^{*}-f_{C}}{f_{F}-f_{C}}$ Coalescence acceleration;

f_{C} Critical porosity corresponding to the beginning of the coalescence;

f_{F} Porosity corresponding to the final rupture of the material;

$f_{U}{}^{*}$The ultimate value, reached when the macroscopic fracture occurs by loss of the bearing load and is calculated by the expression $f_{U}{}^{*}=\frac{1}{q_{1}}$ when $q_{3}=q_{1}{}^{2}$.

During plastic flow, porosity function evolves due to void growth and nucleation, equation 1-31.

$$\dot{f}=\dot{f_{growth}}+\dot{f_{nucleation}} \qquad 1\text{-}31$$

Assuming matrix incompressibility, the term accounting for void growth is expressed by equation 1-32

$$\dot{f_{growth}}=(1-f)\,\dot{\varepsilon}_{kk}^{p} \qquad 1\text{-}32$$

where: $\dot{\varepsilon}_{kk}^{p}$ the trace of the macroscopic strain rates tensor.

When nucleation is governed by the plastic strain, its contribution is given by equation 1-33.

$$\dot{f_{nucleation}}=A\dot{\bar{\varepsilon}}^{p} \qquad 1\text{-}33$$

Chu and Needleman [72] hypothesized that the initiation of voids follows a normal distribution with a mean strain ε_N and a standard deviation S_N, given in equation 1-34.

$$A = \frac{f_n}{S_n\sqrt{2\pi}} exp\left[-\frac{1}{2}\left(\frac{\bar{\varepsilon}^p - \varepsilon_N}{S_N}\right)^2\right] \quad 1\text{-}34$$

where: $\bar{\varepsilon}^p$ the equivalent plastic strain.

The GTN model parameters are then classified into three subsets: constitutive parameters, nucleation parameters, and porosities. The constitutive parameters (q_1, q_2, and q_3) are commonly set to fixed values, with $q_1 = 1.5$, , $q_2 = 1$ and $q_3 = {q_1}^2 = 2{,}25$ based on established literature [63,73–76]. The nucleation parameters include ε_N, S_N and f_N. Typically, ε_N and S_N are assigned values of 0.3 and 0.1, respectively, for most materials [75,76]. These values are typically not regarded as intrinsic material properties but rather as constants, as shown in Table 1-6. This Table presents various GTN model parameters determined for different steel-grade materials, as outlined in the study by Gholipour et al. [76]. The void volume fraction f_N refers to the volume of particles available for void nucleation, and it is considered to have intrinsic material properties.

Table 1-6: Different parameters of the GTN model determined for different steel-grade materials.

Reference	Material	q_1	q_2	q_3	ε_N	S_N	f_0	f_N	f_C	f_F
Tvergaard et al. [65]	-	1.5	1	2.25	0.3	0.1	0	0.04	0.15	0.25
S. More et al. [12]	Interstitial free (IF) steel sheet	1.5	1	2.25	0.1934	0.156	0.0002	0.0005	0.0278	0.163
M. Abbasi et al.[77]	IF steel	1.5	1	2.25	0.1	0.1	0.0002	0.0106	0.0134	0.0216
H. Gholipour et al. [76]	SAE1010 plain carbon steel	1.5	1	2.25	0.3	0.1	0.00107	0.00716	0.01	0.15
Hambli [16]	Carbon steel	1.5	1	2.25	0.3	0.1	-	0.04	-	-
Schmitt et al. [78]	20MnMoNi55	1.5	1	2.25	0.3	0.1	0	0.02	0.06	0.212
Rachik et al. [17]	Steels DD 13, X6Cr17	1.5	1	2.25	0.3	0.1	-	0.04	0.1	0.101
Springmann et al. [79]	Steel	1.5	1	2.25	0.3	0.1	0.001	0.01	0.01	0.15
Lemiale et al. [18]	Mild steel XES	1.5	1	2.25	0.2	0.1	-	0.04	0.15	0.25
Marouani et al. [19]	FeSi (3wt.%) steel	1.5	1	2.25	0.3	0.1	-	0.04	0.11	0.12
Kossakowski et al. [80]	S235JR steel	1.91	0.79	3.65	0.3	0.05	0.0017	0.04	0.06	0.6
Kiran et al. [81]	ASTM A992	1.5	1	2.25	0.45	0.05	0	0.02	0.03	0.5
Achouri et al. [15]	HSLA	1.5	1	2.25	0.3	0.1	0	0.04	0.1	0.15
Zhao et al. [14]	DP600	1.5	1	2.25	0.2	0.1	0.0008	0.02	0.028	0.09

Porosities such as f_0, f_C, and f_F are treated as material parameters. f_0 is the initial void volume fraction. Determining f_C, which marks the onset of coalescence, is challenging and usually done by fitting numerical curves to experimental data. f_F indicates the material's state at fracture.

1.8.1. Literature review on the determination of GTN damage model by inverse analysis

Brunet et al. [82] simulated the deep drawing of a 3D square cup based on the NUMISHEET'93 Benchmark which refers to a standardized set of tests and geometries established for the NUMISHEET'93 Conference, employing the Gurson-Tvergaard model in their numerical simulations. Building on this approach, Ramazani et al. [83] utilized the GTN model to evaluate the FLCs of DP600 dual-phase steel through the cross-die test, a widely used technique in the automotive industry for assessing sheet metal formability. The model parameters were calibrated using response surface methodology (RSM) implemented in MATLAB and validated by comparing experimental and predicted FLCs. The strong agreement between the results confirmed the GTN model's ability to capture failure behavior and highlighted the effectiveness of RSM for parameter calibration.

Similarly, Kami et al. [8] adopted the same inverse identification technique, integrating RSM with numerical simulations of uniaxial tensile tests to calibrate an anisotropic GTN model parameters of AA6016-T4 aluminum alloy. These parameters were then applied to a numerical simulation of the DDP of a rectangular box Through VUMAT Subroutine. A comparison of experimental and numerical results showed remarkable consistency in both the rupture shape and location, as well as near-identical punch force values from both methods.

Amaral et al. [7] utilized MATLAB software for an inverse analysis (IA) to identify parameters of GTN model, Lemaitre, and Johnson-Cook model damage models. This analysis was supplied with a mean square error (MSE) optimization algorithm, which minimizes an objective function through an iterative process, aiming to reduce discrepancies between numerical and experimental results. Observable variables included the force-elongation curve from uniaxial tensile tests and the pressure-pole height from

hydraulic bulge tests. The applicability of the calibrated GTN damage model parameters was validated through a numerical simulation of a cylindrical cup deep-drawing process.

In a related study, Djouabi et al. [41] employed mode FRONTIER software for the inverse analysis to calibrate the parameters of several hardening laws coupled with the GTN damage model. These parameters were then implemented in a circular cup drawing test for DP980 steel sheets, where findings underscored the influence of the selected hardening law on damage model parameters.

1.8.2. A brief overview on inverse identification

The theory of inverse problems, in its broadest sense, was developed by geophysicists. It later expanded to other areas of physics. Applications of this theory include source identification [84], determining internal characteristics of a material [85], geophysical exploration [86], thermal non-destructive testing [87], identifying residual stresses, calibrating vibrational models, and many other fields [88].

The classical identification approach involves conducting simple tests to verify the assumption of homogeneous stress and strain fields within the specimen [89]. The identification of material parameters involves fitting the chosen model over the "experimental" stress-strain curve. However, analytical calculation methods used to determine stress-strain pairs are significantly limited by the assumption of homogeneous stress and strain within the specimen.

Indeed, certain experimental tests are inherently inhomogeneous. Consequently, interpreting these tests as homogeneous directly impacts the predictive accuracy of the identified models [89].

To overcome the assumption of homogeneity, a technique introduced by Schnur and Zabaras [90] involves coupling a finite element calculation code with an optimization method to identify the behavior of a material. This approach is classified among inverse problems, which aim to minimize, through an iterative process, the discrepancy between the computed result and the experimental measurement. The technique typically relies on a specific norm, most often the Euclidean norm. Since its formulation within the framework of inverse problems, this method for identifying material behavior has been widely adopted.

Gavrus et al. [91–94] applied the principle of the inverse method to identify the rheological behavior of thermo-visco-plastic materials subjected to tension and torsion under severe deformation conditions. These conditions are comparable to those encountered in industrial applications, such as self-heating phenomena and strain localization. The minimization algorithm employed in this approach uses the Gauss-Newton procedure.

Mahnken and Stein [95–97] identified the parameters of viscoplastic models using the same identification technique employed by Gavrus et al. Mahnken and Kuhl further extended and adapted this parametric identification technique for other applications [98]. The authors proposed identifying the parameters of damage models that account for non-uniform distributions of stress and strain while incorporating damage variables. Additionally, Gelin and Ghouati extensively applied this inverse identification technique to determine the visco-plastic behavior parameters of aluminum alloys [99]. These authors also employed the inverse method in other studies [100–104].

The inverse identification technique has also been applied in forming processes to identify material behavior, predict formability and potential damage, enhance product quality, and optimize the process.

1.8.3. Coupled and Uncoupled inverse identification

Inverse identification is referred to as coupled when the model identifies both the hardening law and damage parameters simultaneously. In contrast, it is considered uncoupled when the parameters are identified separately. In previous researches, inverse parameter identification has emerged as a widely adopted technique to identify simultaneously or separately the parameters the hardening laws and GTN damage model. This approach, whether iterative or non-iterative process, minimizes discrepancies between experimental and numerical outcomes [105,106]. Its convergence depends on factors such as the number of parameters to be identified [106] and whether the hardening law is coupled or not coupled with the damage model. Recent studies highlight the superior accuracy and performance of coupled models [13,41,75,107,108].

The identification process is commonly based on global or local experimental data from conventional mechanical tests including force-displacement curves from tensile tests and pressure-pole heights from bulge tests. However, despite its advantages,

parameter identification remains challenging task in practical applications, primarily due to the non-uniqueness of solutions, which often makes successful calibration of GTN model parameters elusive [109].

The literature review summarizes previous research on identifying GTN model parameters and their sheet metal forming process's simulation, as outlined in Table 1-7. These studies primarily emphasize the type of used observables (local or global) for calibrating the GTN damage model, both in conjunction with and independent of hardening laws, as well as their applications in sheet metal forming. The current study is included at the end of the table to clearly distinguish its contributions from prior work.

Table 1-7: Previous research on the identification of GTN model parameters and their application in sheet metal forming processes.

Sheet material	Damage model	Anisotropy	Hardening law	Identified parameters		Calibration strategy		FE simulation	Ref
						Experiments	Observables		
AA6016-T4 metallic sheet	GTN	Hill 48	Swift	$f_0 f_C$ $f_N f_F$	4	Tensile test	Force-Elongation	Deep drawing of a rectangular box.	[8]
Aluminum alloy AA5182-O	GTN Jonson Cook Lemaitre	X	Voce	$f_0 f_C$ $f_N f_F$ $d_1 d_2 d_3$	7	Tensile test Bulge test	Load-Elongation Pressure-Pole height	Deep drawing of a cylindrical cup	[7]
DP980 steel sheet	GTN	X	Swift-Voce Hockett-Sherby Swift-Hockett-Sherby	$q_1 q_2$ $f_0 f_N \varepsilon_N$ $S_N f_C f_F$	8	Tensile test	Force-Elongation	Deep drawing of a circular cup	[41]
Interstitial free (IF) steel sheet	GTN	X	Hollomon	$f_C f_N f_F$ $\varepsilon_N S_N$	5	Tensile test	Stress-strain	Single Point incremental forming (SPIF)	[12]
Tailor welded blanks (TWBs)	GTN	X	------	$f_0 f_C f_N$ $f_F \varepsilon_N S_N$	6	Tensile test	Stress-strain	Hecker test	[109]
IF steel	GTN	X	------	$f_0 f_C$ $f_N f_F$	4	Tensile test	Stress-strain	Hecker test	[77]
DC06 0.8 mm sheet	GTN	Hill 48	--------	$f_N \varepsilon_N$	2	Tensile test	Stress-strain	Incremental sheet forming (ISF)	[110]
DC06EK	GTN	X	Ludwik	σ_0, K, n $f_N f_C f_F$	6	Tensile test	Force-displacement Equivalent plastic strain	Deep drawing process of wheelbarrow tray	In this thesis work

1.9. Conclusions

At the EIMS company, deep drawing is widely used to manufacture household appliances, sanitary products, and industrial components. This company is also looking to expand its production to the automotive sector by subcontracting with major companies, Fiat and Mercedes, focusing on deep-drawn components such as automotive body parts. The primary challenges encountered during the DDP include the occurrence of wrinkling and rupture defects. Therefore, the objective is to develop a reliable numerical tool capable of accurately simulating the actual phenomena occurring during the DDP. Achieving this requires not only modeling the process itself but also precisely characterizing the behavior of the sheet metal.

In this thesis work, the GTN damage model is proposed as a potential alternative to traditional FLCs for industrial deep drawing applications. Based on the bibliographic review, the application of the GTN model has been limited to experimental DDP and has not been adopted in industrial scenarios (Table 1-7). Furthermore, the identification of GTN model parameters remains a significant challenge in industrial applications [109]. The non-uniqueness of solutions often hinders the successful calibration of GTN parameters in many cases. Addressing these two limitations constitutes the novelty of this thesis.

The choice of sheet material focused on cold-rolled steels due to their extensive use at EIMS and their application in deep drawing various automotive body parts. To enable comparisons with the aforementioned numerical studies in subsection § 3.2, the DC06EK sheet metal was selected.

The next step of this thesis work will focus on identifying the parameters of a hardening law coupled with the GTN damage model, as discussed in subsection § 1.8.3 Following a similar approach to previous studies, an inverse analysis method will be used.

However, unlike prior works, the novelty of this identification process lies in the utilization of both global and local experimental data (observables). This method primarily focuses on force-displacement curves and the evolution of equivalent plastic strain in two distinct regions within a tensile specimen: (1) a central region where rupture occurs, characterized by either a bifurcation or a significant increase in equivalent plastic

strain, and (2) another region where equivalent plastic strain stabilizes, indicating stagnation of deformation. This approach is inspired from literature (subsection § 1.8.1). The ratio of equivalent plastic strains in these two regions provides critical insights into the precise moment when necking initiates before rupture. This innovative approach offers a more nuanced and comprehensive understanding of the material's plastic behavior, particularly during the critical stages of deformation and damage evolution.

Chapter 2. Characterization of anisotropy and GTN damage model

2.1. Introduction

The primary objective of this chapter is to characterize the anisotropy, hardening behavior, and GTN damage model of the DC06EK sheet metal. The ultimate goal is to use these characterization data in the numerical simulation of a deep drawing of an industrial application conducted in the EIMS company.

This chapter begins with an investigation of anisotropy behavior through tensile tests performed on standard specimens. From these tests, the plastic yield criteria for the DC06EK sheet metal are determined.

As deducted from the first chapter, the identification of a coupled hardening law and GTN damage parameters is pursued using a unified numerical approach. This involves employing an inverse analysis method based on tensile tests conducted on specimens with a variable (notched) cross-section cut from the DC06EK sheet metal. The numerical simulations of these tests, coupled with an optimization tool, were executed using the ABAQUS finite element software. The inverse analysis strategy was validated on a pseudo-experimental database and then used on real experimental data to finally determine the parameters of the hardening law coupled to the GTN damage model.

2.2. Tensile tests

2.2.1. Specimens

To study the plastic behavior, assess anisotropy, and identify the GTN damage parameters of DC06EK steel, tensile tests were conducted on specimens of varying geometries. These specimens were obtained from a cold-rolled DC06EK steel sheet with a thickness of 1.6 mm. Approximately sixty tensile specimens were cut using water jet cutting technology following three orientations relative to the rolling direction: 0°, 45°, and 90°.

The geometry of cut specimen is illustrated in Figure 2-1. This process was initially undertaken in the research work of A. Belguebli [28] and continued in the early stages of this thesis. Water jet cutting was chosen for its precision and superior surface finish, minimizing manufacturing defects that might influence material behavior under tensile forces. More than half of these specimens were used in the present study.

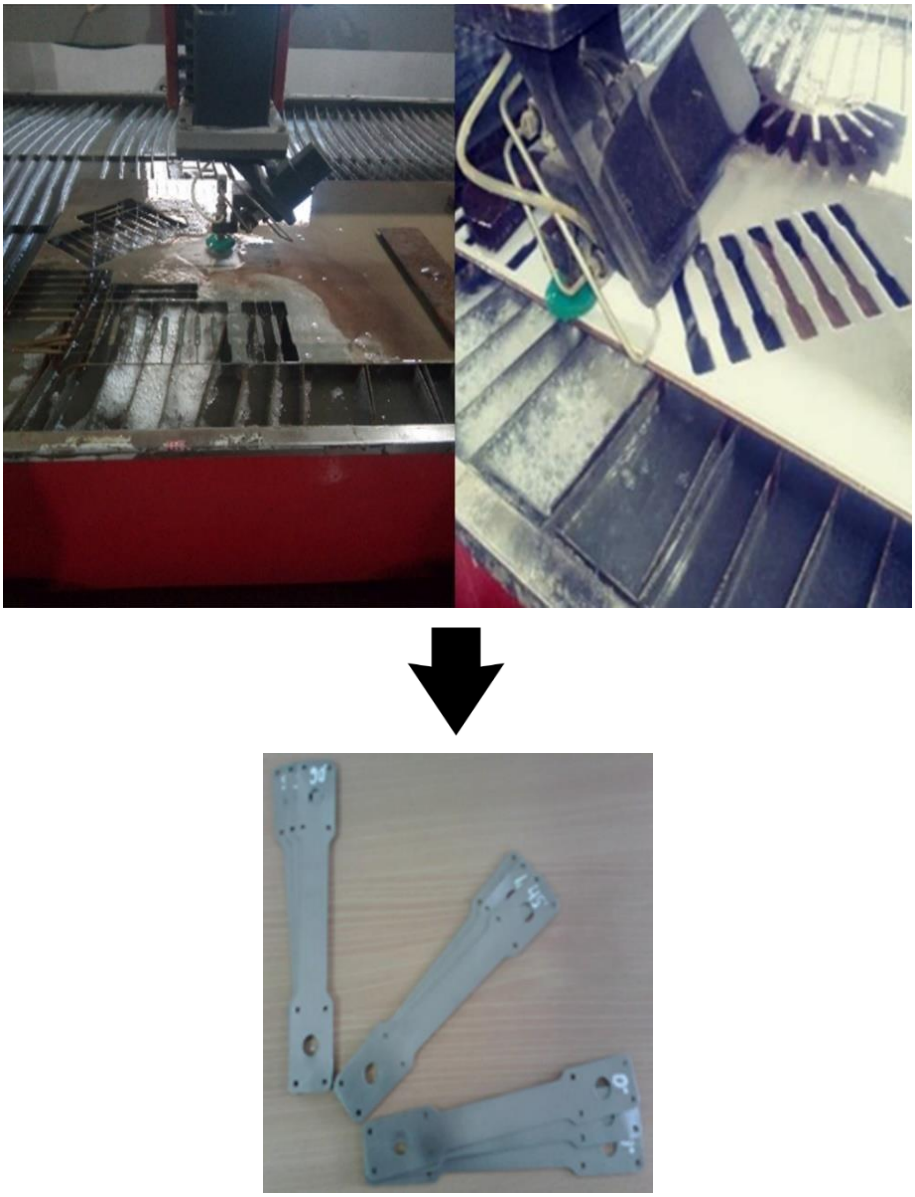

Figure 2-1: Water jet cutting process [28].

Two specimen geometries were prepared and tested using a tensile testing machine, as shown in Figure 2-2 and Figure 2-3. The first geometry, with a constant cross-section, was designed according to ASTM E8M-2010 standards [111] (Figure 2-2). For each rolling direction (0°, 45°, and 90°), three specimens were tested to ensure reproducibility. Subsequently, notched specimens with variable cross-sections (Figure 2-3) were machined from the constant-section specimens using a milling machine. To prevent bending during machining due to the thin sheet thickness, multiple specimens were clamped together in a vice.

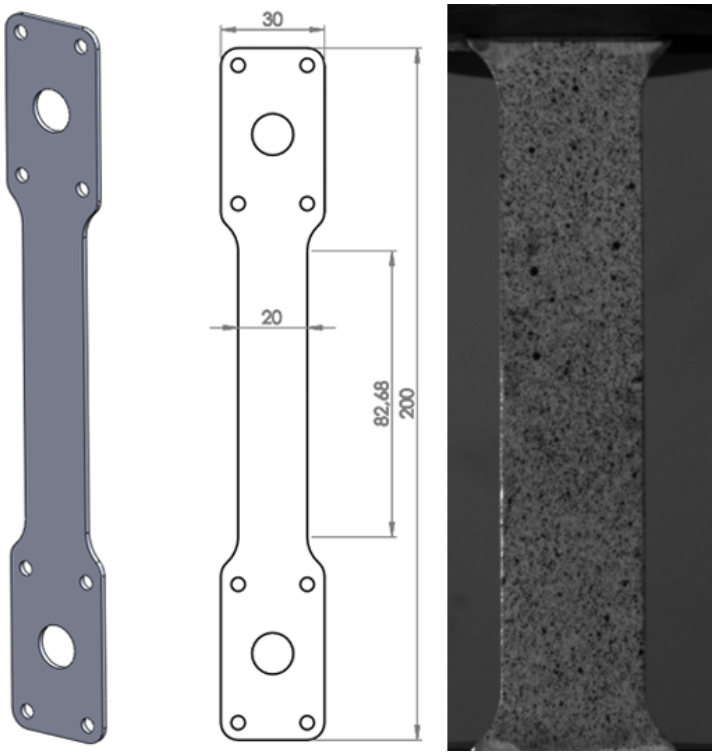

Figure 2-2: Uniaxial tensile specimen with a constant cross-section.

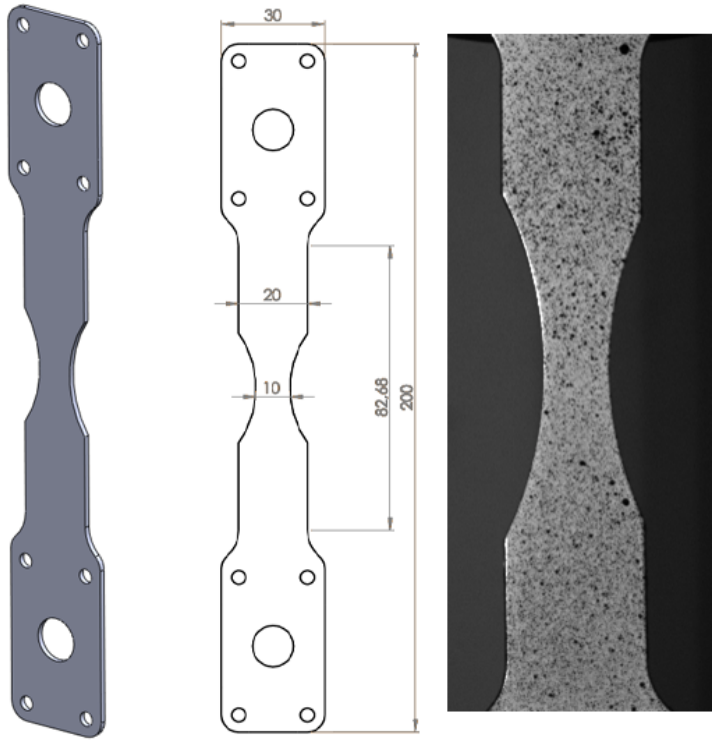

Figure 2-3: Uniaxial tensile specimen with a variable (notched) cross-section.

2.2.2. Test Procedure

The tensile tests were carried out on a GUNT WP 310 tensile testing machine with a 50 kN load capacity at a constant velocity of 1 mm/min. The gauge section of each specimen was monitored using a high-resolution camera operating at an acquisition rate of 1 image per second. Plastic strain levels were determined through digital image correlation (DIC), while load, displacement, and time data were directly recorded by the tensile machine's sensors. As mentioned in subsection § 2.2.1, tensile tests were performed according to ASTM E8M-2010 standards [111].

2.2.3. Digital Image Correlation (DIC) Technique

The DIC technique, developed since the 1980s [112,113], is a method used for determining displacement fields. From these fields, local deformations in the specimen are calculated. It is particularly useful in the field of material mechanics for analyzing the behavior of structures under loading.

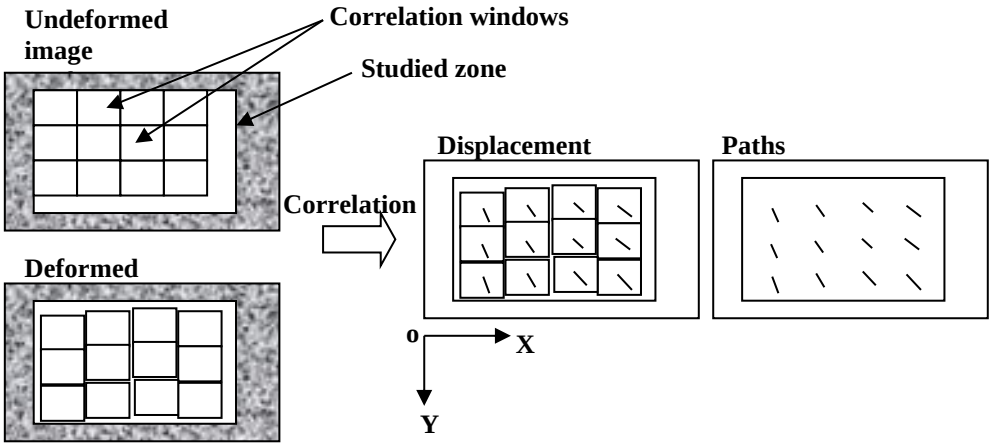

Figure 2-4: Principle of displacement and path determination by image correlation [38].

This technique involves capturing a sequence of images during specimen loading: one image before deformation, called the "reference image", and others after deformation, called "deformed images" [38]. These images must have a random grayscale pattern by creating a speckle on the surface of the specimen (Figure 2-2 and Figure 2-3). This speckle is typically created by first applying a layer of white paint, followed by droplets of black paint, which creates a random pattern of contrasted spots.

The fundamental principle of the technique is to find the displacement needed to align the pattern of the reference image with that of the deformed image. This process allows for determining the displacement field on the surface of the specimen, i.e., how each point on the surface has moved in response to the applied load (Figure 2-4). These displacement fields are then used to compute local strain fields.

The DIC experimental setup consists of a high-resolution camera to capture images, a computer with acquisition and analysis software, and a lighting system to ensure good image quality. The software analyzes the images by defining a series of correlation windows, which are small areas on the image where displacements are calculated. The size of these windows is crucial for the accuracy of the measurement and must be selected based on the size of the speckle spots and the image resolution [38].

Using this technique, anisotropy coefficients (Lankford coefficients) were calculated from longitudinal and transversal plastic strains.

The "GOM Correlate" software was used to calculate the local plastic strains in the principal directions ($\varepsilon_1, \varepsilon_2$).

2.2.4. Tensile test results

The tensile tests yielded several important results:

- Principal plastic strains ($\varepsilon_1, \varepsilon_2$) were derived from tests conducted on constant cross-section specimens (Figure 2-5) to calculate different anisotropic parameters, as detailed in subsection 2.3.1.
- Force-displacement and equivalent plastic strain results were obtained from tests on variable cross-section specimens (Figure 2-6) to identify the coupled hardening law and GTN damage parameters.

A detailed analysis of these results is provided in subsequent subsections (§ 2.4.3), particularly the determination of equivalent plastic strain in two distinct regions: one on the rupture zone and the other at a distance from the rupture zone.

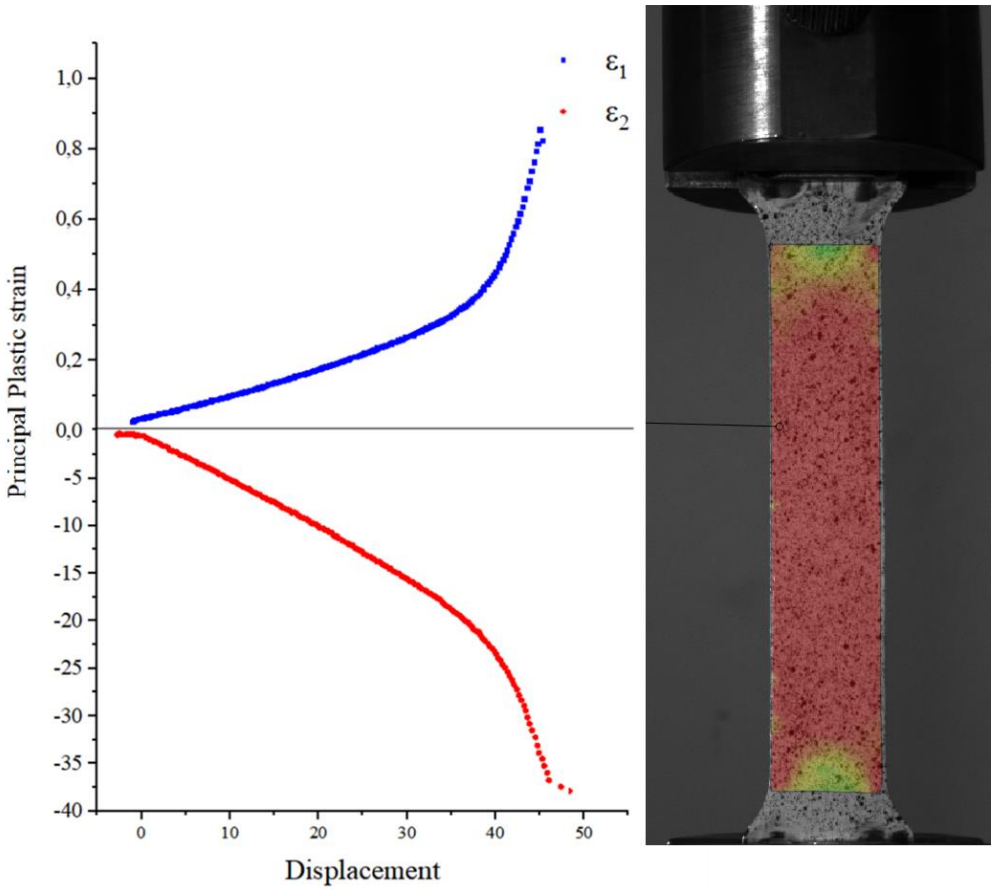

Figure 2-5: Example of tensile test results on specimens with a constant cross-section.

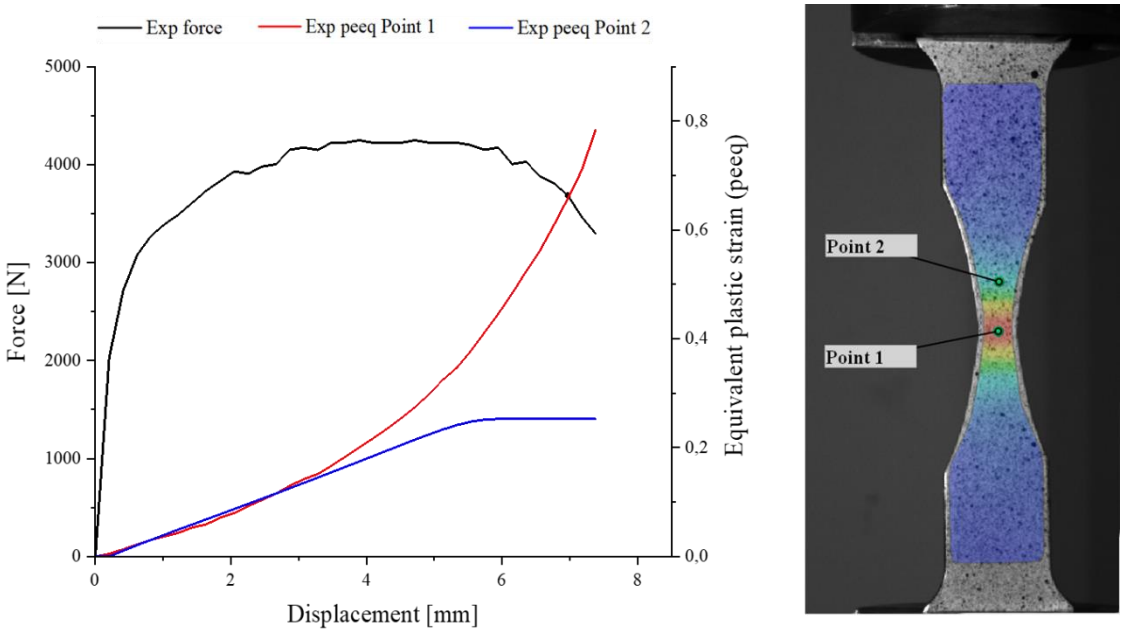

Figure 2-6: Example of tensile test results on specimens with a variable cross-section.

2.3. Anisotropy Characterization

2.3.1. Anisotropy & Lankford Coefficients

The study of anisotropy in sheet metals is often based on Lankford coefficients, which describe the ratio between transverse plastic strain and thickness plastic strain (see equation 1-3). These coefficients were determined through tensile tests conducted at three orientations (0°, 45°, and 90°) relative to the rolling direction. These tests were performed on specimens with a constant cross-section (Figure 2-2), as detailed in section § 2.2.

The average Lankford coefficient for each orientation was calculated over the strain range of 5% to 20%, in accordance with the ISO 10113:2020 standard [114]. Figure 2-7 illustrates the evolution of Lankford coefficients with respect to equivalent plastic strain during tensile tests for different orientations relative to the rolling direction. The Lankford coefficients calculated for each orientation yielded the following values: $r_0 = 1.81$, $r_{45} = 1.9$ and $r_{90} = 2.2$.

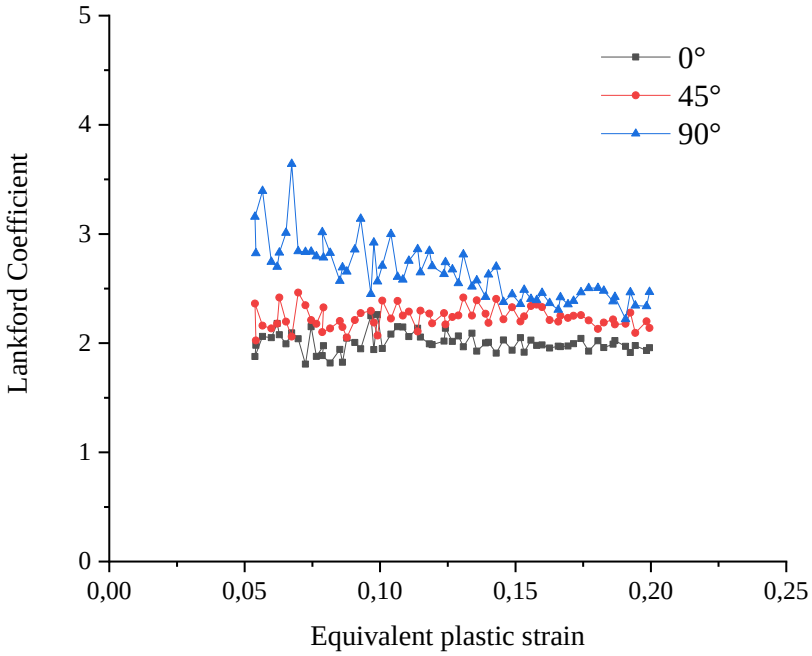

Figure 2-7: Evolution of Lankford coefficients as a function of equivalent plastic strain.

Figure 2-7 compares the Lankford coefficients obtained for DC06 steel sheet in this study with those reported in prior research. Differences in Lankford coefficients can primarily be attributed to variations in mechanical properties and chemical composition between the material used in different study and those of previous works. These discrepancies arise due to differences in supplier specifications for the steel sheets.

Table 2-1 gathers the Lankford coefficients of DC06Ek steel for some previous research including the calculated anisotropy coefficients of our study.

Table 2-1: Lankford coefficients of DC06EK

Reference	r_0	r_{45}	r_{90}
L. Junchao et al. [110]	1.85	1.78	2.45
M. Safaei et al. [115]	1.794	2.003	2.532
A. Kami et al. [116]	2.027	1.751	2.467
J. Majerníková et al. [117]	1.888	1.464	2.193
A. Belguebli et al [11]	2.82	1.95	2.68
Current work	**1.81**	**1.9**	**2.2**

The calculated Lankford coefficients closely match prior study. However, the notable difference in r_0 and r_{90} compared to those reported by A. Belguebli et al [11] can be largely attributed to the change in the sheet metal supplier, affecting the material's microstructure, texture, and mechanical properties. This highlights the importance of supplier consistency in ensuring reproducible forming characteristics in industrial applications. The analysis further confirms the strongly anisotropic behavior of DC06EK.

By definition, normal anisotropy refers to the variation in deformation between the plane of the sheet and its thickness. This variation is quantified by the normal anisotropy ratio, commonly known as the r value, which is a critical parameter for sheet materials. Planar anisotropy is associated with the deviation denoted as Δr. To characterize the anisotropy type (normal or planer), the mean anisotropy coefficient r and the deviation Δr were calculated using the following equations:

$$r = \frac{r_0 + 2r_{45} + r_{90}}{4} = 1.95 \qquad 2\text{-}1$$

$$\Delta r = \frac{r_0 - 2r_{45} + r_{90}}{4} = 0.10 \qquad 2\text{-}2$$

In cases where $r \neq 1$ and $\Delta r \neq 0$, the material exhibits either normal and planar anisotropy [38]. For the DC06EK sheet metal, the calculated parameters confirm the used material exhibits strong anisotropy.

2.3.2. Hill 48 Yield Criterion

To account for anisotropy in the modeling of the material's plastic behavior, the Hill 48 anisotropic yield criterion [118] was selected for this study among other criteria. Hill 48 was chosen due to its low number of parameters, which simplifies identification, and because it is pre-integrated into the Abaqus numerical simulation software. Under the plane stress assumption, the Hill 48 criterion is done by equation 1-11.

The Hill48 quadratic parameters are determined from the Lankford coefficients using equation 1-16. From these equations, it was assumed that the hardening in the rolling direction represents the material's overall hardening behavior. The resulting Hill48 parameters for DC06EK are summarized in Table 2-2. In this table, it's noted that there is a discrepancy between the Hill yield criterion parameters obtained in the present work and those reported by A. Belguebli [28]. The differences range from 0.01 to 0.4, with the most significant variation occurring in parameter N (0.4). The DC06EK sheet used in this study is not purchased from the same producer by the EIMS company as that used in the work of Belguebli, which explains the discrepancies in the Hill 48 parameters.

Table 2-2: Hill 48 anisotropic yield criterion parameters of DC06EK steel sheet.

Parameter	***F***	***G***	***H***	***N***
Present work	**0.29**	**0.35**	**0.64**	**1.55**
A. Belguebli [28]	0.28	0.26	0.74	1.15
Error	0.01	0.09	0.1	0.4

Even though the material is designated as DC06EK in both cases, small differences in microstructure, crystallographic texture, or residual stresses can significantly impact anisotropic yielding behavior. Therefore, supplier-dependent variations must be carefully considered when comparing experimental results or applying material models in numerical simulations.

An experimental-analytical comparison was conducted for Lankford coefficients (Figure 2-8). These values were analytically determined based on the obtained results from uniaxial tensile tests oriented at an angle θ relative to the rolling direction. The Hill 48 model (equation 1-11) provide satisfactory approximations of the experimental yield stresses at 0°, 45°, and 90°.

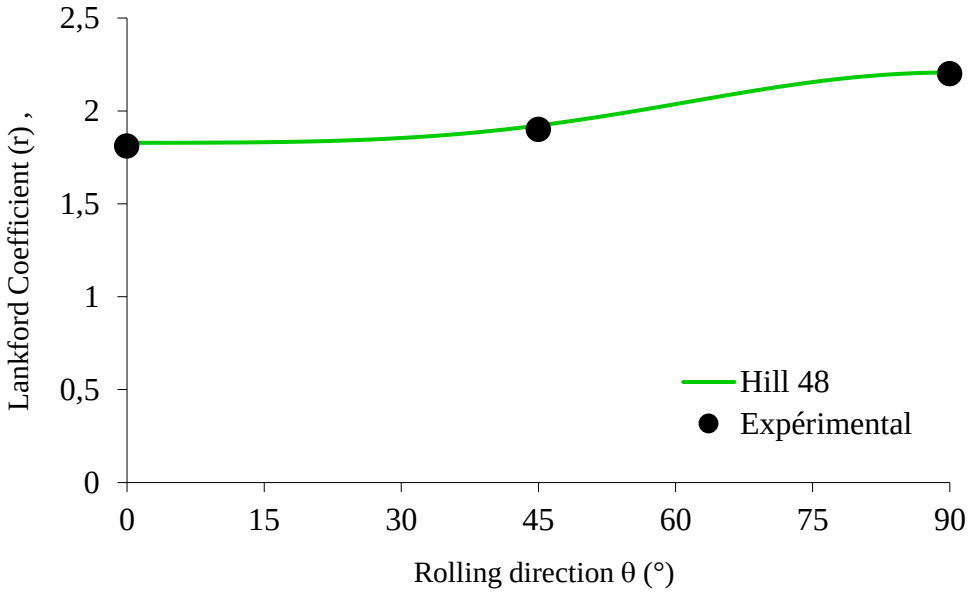

Figure 2-8: Lankford coefficient as a function of the rolling direction.

2.3.3. Non-Quadratic yield criteria

Figure 2-9 compares the quadratic and non-quadratic yield surfaces derived from isotropic and anisotropic yield criteria, as presented in subsections § 1.7.1.1, 1.7.1.2 and 1.7.1.3. It is noted that the curves are very representative of the experimental elastic limit stresses (σ_1 and σ_2).

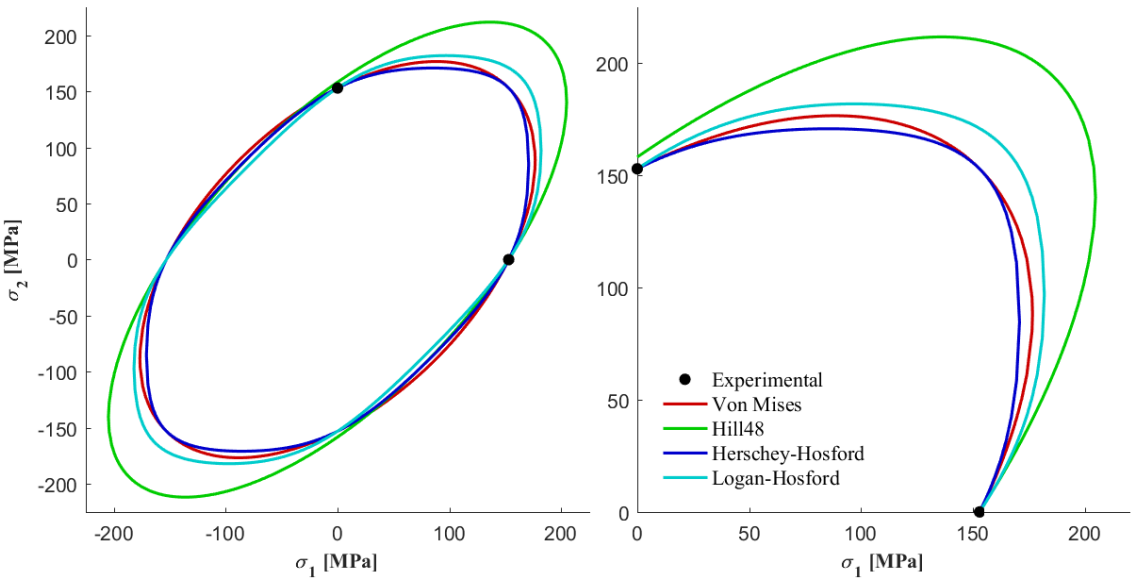

Figure 2-9: Comparison of experimental and yield surfaces plot for different yield criteria.

Additionally, we observe that the experimental point is on the line of yielding surfaces of Von Mises and Herschey-Hosford criterion, while for Hill 48 and Logan-Hosford, it is located under the bounds of their yield surfaces. The yield stresses (Figure 2-9) along the two directions (0° and 90°) give the impression that this is a material with low anisotropy. However, the average Lankford coefficient ($R = 1.95$) indicates that the material is highly anisotropic.

The anisotropic Logan-Hosford and Hill 48 surfaces are higher than those of the isotropic Mises and Hershey-Hosford models under biaxial stress, illustrating the normal anisotropy. Hence, it is necessary to carry out further experiments to characterize the DC06EK sheet metal under biaxial stress state.

2.4. GTN damage model parameters identification

Material characterization involves a combination of experimental testing and numerical simulations. Among the conventional experimental test, the tensile test which is widely used. While for the numerical side, various approaches are available, including the inverse identification technique. This technique indirectly determines unknown material parameters through an iterative process, using known global and local observables such as tensile force, plastic strain, and displacement. This resolution process is defined as inverse problems [75].

2.4.1. Adopted inverse identification procedure

An inverse identification procedure was employed to identify the parameters of the coupled GTN model coupled with a hardening law for the studied DC06EK sheet metal, assuming the material to be isotropic.

In this procedure, an optimization tool developed by GAVRUS [91] was used and integrated with the numerical model of the tensile test. This tool identifies the optimal set of parameters that best align the experimental and numerical curves and minimizes the cost function (Q) using the Gauss-Newton iterative algorithm at each iteration.

A general overview of the inverse identification process is illustrated in Figure 2-10.

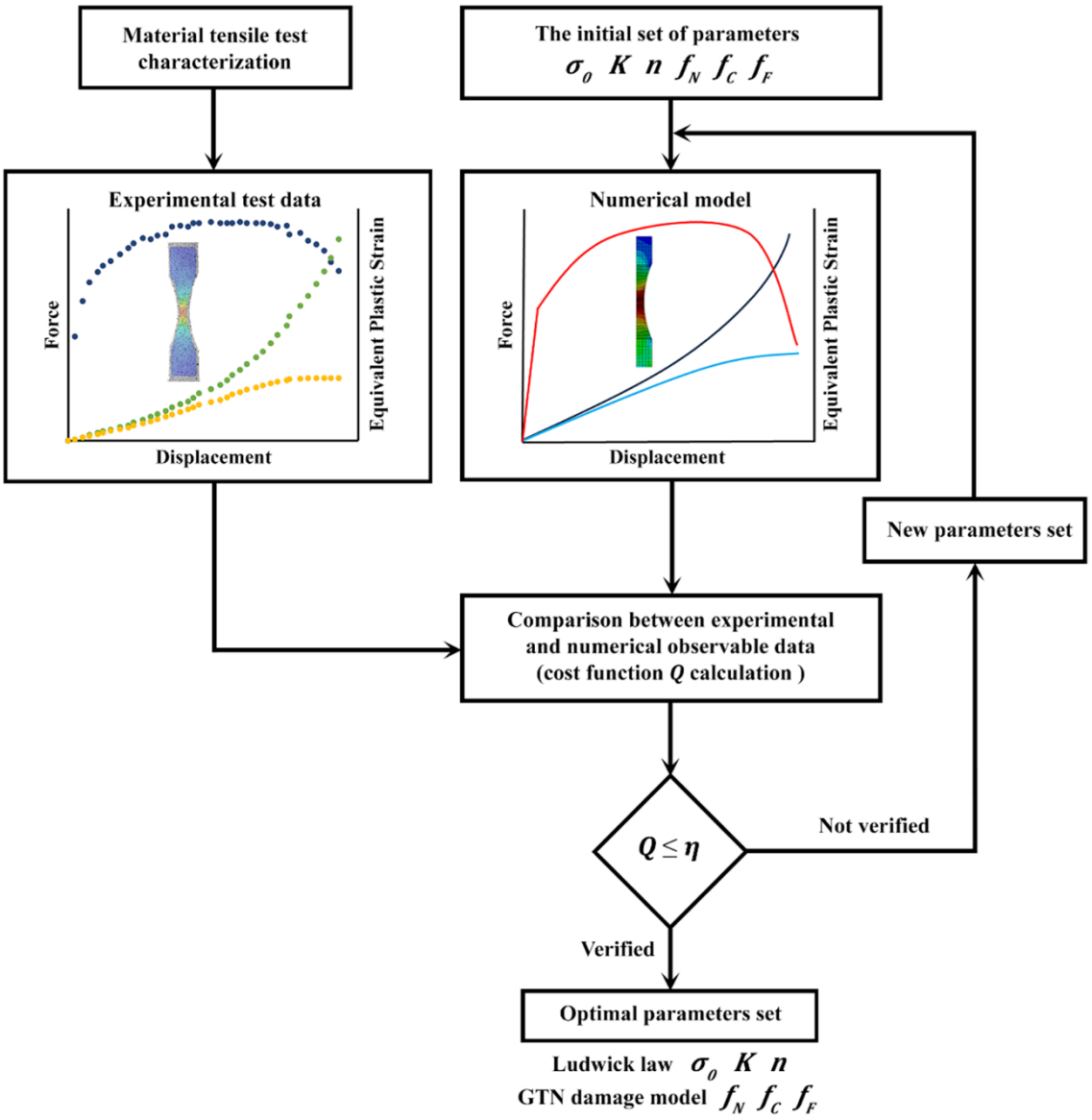

Figure 2-10: Inverse identification procedure diagram.

The cost function (Q) is given by equation:

$$Q = \frac{\sum_{i=1}^{Np}(\bar{F}_{exp}^{i} - \bar{F}_{num}^{i})^2}{\sum_{i=1}^{Np}(\bar{F}_{exp}^{i})^2} \qquad 2\text{-}3$$

where: $\overline{F}_{exp}^{i}$ (or $\overline{F}_{num}^{i}$) = { $\overline{F}^{i}$ } with $i = \{1, 2, \ldots\}, N_p$ total number of experimental measures (or computed), and η allowable error.

In addition to the numerical model of the tensile test, this process relies on both local and global observables, i.e., on obtained results from the tensile test on a specimen with a variable cross-section, described in section 2.2, specifically the tensile force and the evolution of plastic strain in two distinct zones.

2.4.2. Numerical model of tensile test

2.4.2.1. Numerical model

The tensile test was performed on specimens with a variable cross-section. This specimen is specifically chosen because it induces localized strain at the center. This tensile test is modeled and simulated on ABAQUS software, with only half of the specimen considered to take advantage of symmetry.

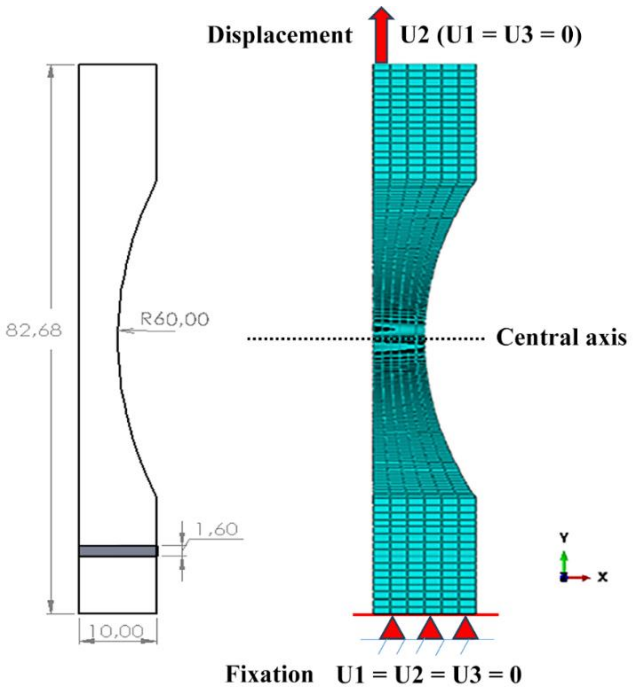

Figure 2-11: Geometry of the specimen and its tensile test's numerical model.

An isotropic elastoplastic behavior was adopted because just the parameters of the coupled Ludwick's hardening law and the GTN damage will be identified by inverse analysis. Elastic behavior was described using Hooke's model, with a young's modulus E=210000 MPa and Poisson's ratio ν=0.3. For plastic behavior, Ludwick's hardening law and the GTN damage model were integrated into the numerical model.

Within the numerical model, the geometry and applied boundary conditions are replicated from the tensile test experiment, fixating the specimen from the bottom side and applying a displacement on the top, as illustrated in Figure 2-11. As for the mesh, we adopted a refined mesh relying on segment mesh (local seeds) in double direction starting from the middle of the specimen. Moreover, we used hexahedral elements, type C3D8R with a 2895 total number of elements.

The hardening behavior is defined using the VUHARD subroutine. while, the GTN damage model parameters are set directly through the porous metal plasticity option available in Abaqus/Explicit [119].

2.4.2.2. Mesh sensitivity

As shown in Figure 2-12-a mesh sensitivity analysis was performed on the specimen using four different mesh sizes. Since the inverse identification process incorporated both global and local data, the sensitivity was assessed based on two key curves: force vs. displacement and equivalent plastic strain vs. displacement at the center of the specimen.

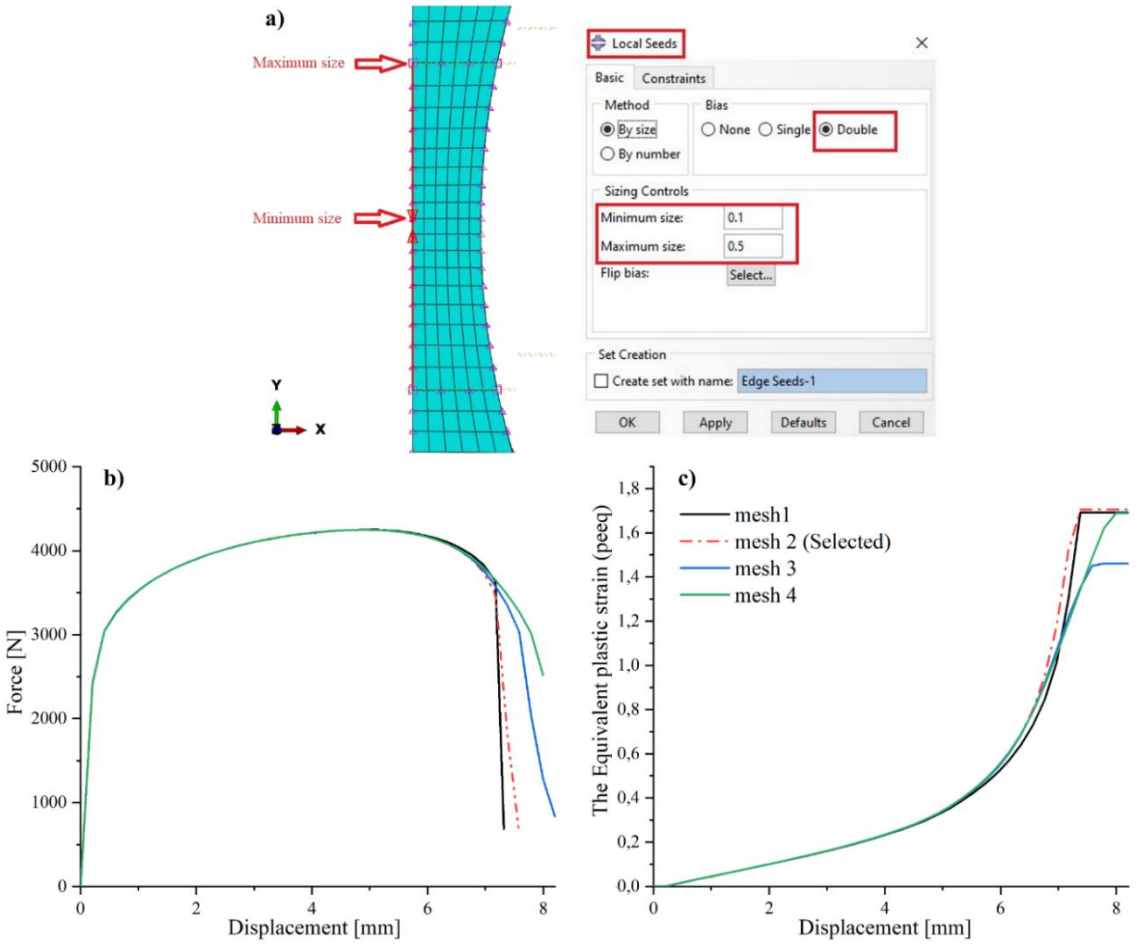

Figure 2-12: Mesh sensitivity analysis: (a) Meshing method, (b) Force vs. displacement, and (c) Equivalent plastic strain vs. displacement.

As shown Figure 2-12-b and Figure 2-12-c, the results stabilize with mesh 2 for both the force vs. displacement curve and the equivalent plastic strain vs. displacement curve.

Table 2-3: CPU time for different mesh sizes.

Mesh	Number of Elements	Min-Max element size (mm)	Relative CPU Time (hr:min:sec)
Mesh 1	7545	0.05 – 0.1	00 :24: 24
Mesh 2	**2895**	**0.1 - 0.5**	**00 :08 :42**
Mesh 3	2340	0.2 - 0.6	00 :07 :10
Mesh 4	2070	0.3 - 0.7	00 :06 :39

The analysis of Table 2-3 reveals a clear trade-off between mesh resolution and computational efficiency. The choice of an optimal mesh must balance accuracy and CPU time, ensuring that the simulation captures local plastic deformation and force response at the onset necking and rupture zones without excessive computational cost.

Mesh 1 provides the highest resolution with the smallest element size (0.05 – 0.1 mm) but comes at a significant computational cost, requiring 24 minutes and 24 seconds of CPU time. While this fine mesh ensures high accuracy, its long simulation time makes it impractical for parametric identification using the inverse analysis. On the other hand, Mesh 3 (0.2 – 0.6 mm) and Mesh 4 (0.3 – 0.7 mm) have the largest elements and the shortest CPU times. However, their coarse resolution results in a loss of accuracy, particularly in capturing local plastic deformation and force response at the onset of necking and rupture zones. Meanwhile, Mesh 2 (0.1 – 0.5 mm) emerges as the optimal choice. It strikes a balance between computational efficiency and accuracy. This mesh makes it possible to capture local plastic deformation and force response at the onset necking and rupture zones exactly the same as Mesh 1, but with significantly reduced computational time (08 minutes and 42 seconds). Consequently, Mesh 2 was chosen for the numerical identification process.

2.4.3. Inverse identification strategy

The inverse identification technique is typically performed on observables obtained from the tensile test on specimen with variable cross-section. The observables can be divided into two categories: global observables such as tensile force, and local observables such as strains or local displacement. Many authors used only global or local observables [7–9,12,13,41,75,76,108,109]. Still, this work investigates the use of both global and local observables. This involves the integration of a local observable, which is the plastic strain at two different zones within the specimen.

The inverse identification strategy consists of three separate cases, as illustrated in Figure 2-13 and Table 2-4:

- The first case entails using only the global observable (tensile force).
- The second case adds a local observable (equivalent plastic strain: PEEQ 1) at the rupture zone, where either bifurcation occurs or a significant increase in plastic strain is observed.
- The third case considers all the observables and also adds the equivalent plastic strain: PEEQ 2 at shifted zone where plastic strain stagnates after necking initiation.

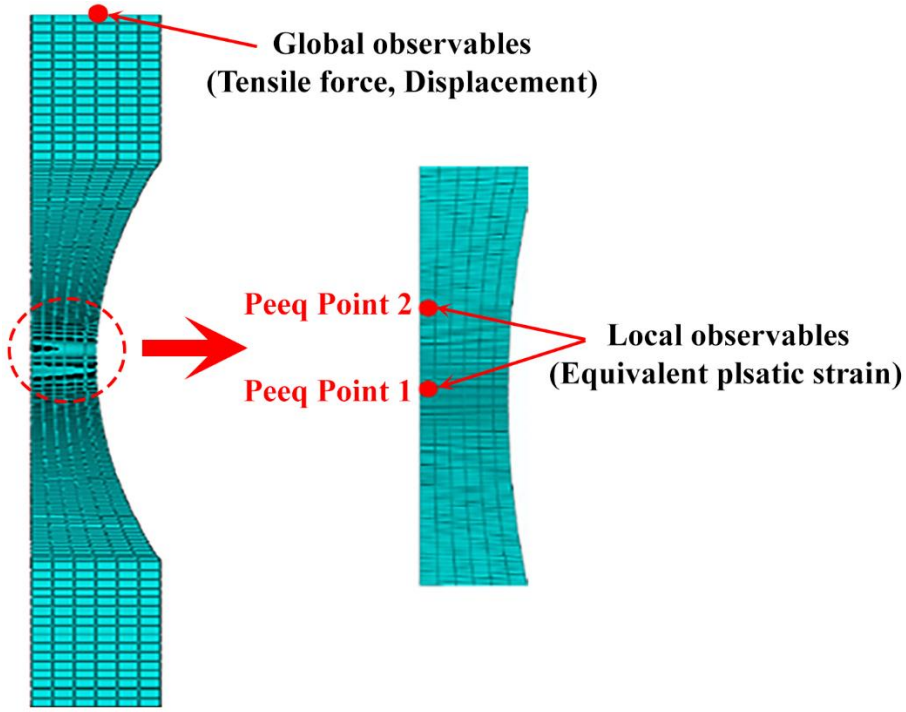

Figure 2-13: Inverse identification global and local observables.

Table 2-4: Different cases of the inverse identification strategy.

Cases	Selected number of observables
1	Tensile force
2	Tensile force + Equivalent plastic strain at a central zone within the specimen (rupture zone)
3	Tensile force + Equivalent plastic strain at a central zone within the specimen (rupture zone) + Equivalent plastic strain in a shifted (another) zone from the center (stagnation zone)

To validate this inverse identification strategy, the study explores both pseudo-experimental and experimental identification processes. Pseudo-experimental identification uses simulated data to test and refine the identification methodology, while experimental identification relies directly on tensile test results. The findings from both approaches are presented, emphasizing how the number of observables affects the accuracy and effectiveness of parameter identification. By combining these approaches, the study provides a comprehensive evaluation of the inverse identification strategy and their contribution in material characterization.

2.4.4. Validation of the inverse identification strategy on pseudo-experimental database

To validate the numerical approach of the identification by inverse analysis, detailed in subsection § 2.4.3, an inverse identification was carried out on a pseudo-experimental database. To generate the pseudo-experimental database, namely: force, PEEQ1 and PEEQ2 as a function of the displacement, we consider the Voce hardening law (equation 1-23) and the GTN damage model (subsection § 1.8). The parameters of the latter are given in Table 2-5.

Table 2-5: Voce hardening law and GTN damage model parameters.

	Voce law			**GTN damage model**								
Parameters	σ_0	σ_s	A	q_1	q_2	q_3	S_N	ε_N	f_0	f_N	f_C	f_F
DC06	200 MPa	350 MPa	10	1.5	1	2.25	0.1	0.3	0.0005	0.0008	0.0219	0.1677
Ref.	[120]			[121]								

2.4.4.1. Selection of parameters

The identification of GTN damage coupled with hardening law parameters is a challenging task due to the non-uniqueness of the solution [122,123]. To simplify the process, many researchers adopt the values proposed by Tvergaard for q_1, q_2, q_3, S_N and ε_N, as explained in subsection § 1.8 and illustrated in Table 2-5 . In this study, the same simplification is used to reduce the number of identifiable parameters, enabling more accurate calibration of the remaining ones. Consequently, f_N, f_C, and $f_F$will be identified using the inverse identification procedure. The parameters of the Voce hardening law are also added as presented in Table 2-6.

Table 2-6: Voce hardening law and GTN damage model parameters to be identified.

Voce law			GTN model		
σ_0	A	σ_s	f_N	f_C	f_F

The inverse identification entails of using the mentioned observables of the pseudo-experimental database to identify the hardening and damage parameters beginning with an initial set of values. At each iteration, the algorithm compares the new identified parameters with the pseudo-experimental data until reaching an optimal set with an acceptable error.

2.4.4.2. Identification results

Table 2-7 illustrates Identified parameters for the three (3) cases confronted with those of used in generating pseudo-experimental data.

Table 2-7: Identified parameters for the three (3) cases confronted with those of used in generating pseudo-experimental data.

			Parameters						Error (%)
			σ_0	A	σ_s	f_N	f_C	f_F	
Initial parameters			155	15	400	0.001	0.003	0.1	
Identified parameters	**Cases**	**1**	157.56	13.95	380.18	0.002	0.0380	0.19	2.78
		2	155.50	14.37	395.21	0.002	0.012	0.4	3.40
		3	**189.72**	**10.86**	**357.39**	**0.0005**	**0.025**	**0.1**	2.16
Parameters used in generating pseudo-experimental data			**200**	**10**	**350**	**0.0008**	**0.0219**	**0.1677**	

For case 1, when using only the global observable (tensile force), there is practically no significant change between the initial and the identified parameters, while the discrepancy between the identified and pseudo-experimental observables is very closed with an error 2,78 %.

For case 2, even adding the local observable (equivalent plastic strain in the rupture zone), the error between the identified and pseudo-experimental observables is about 3,4 %. However, the same remark as for case 1 is noted: there is almost no significant change between the initial and identified parameters.

For case 3, we observe that the addition of the third observable, equivalent plastic strain at the zone where plastic strain stagnates after necking initiation, helped the inverse identification algorithm to converge to the parameters used in generating pseudo-experimental data, minimizing the discrepancy and leading to the optimal set. The error between the identified and pseudo-experimental observables is the minimal between the three cases and is about 2,16 %.

To illustrate the influence of the number of observables on the inverse identification technique, we plotted the tensile force and the equivalent plastic strains versus the displacement for the identified and the pseudo-experimental parameters Figure 2-14.

For Case 1, we can see a notable difference between the identified and the pseudo-experimental tensile force. As for case 2, we notice discrepancy between the curve of the pseudo-experimental and the identified. Meanwhile, for the plastic strain, a slight change is observed.

On the other hand, case 3 provides more information regarding the local observables by adding equivalent plastic strain at the zone where plastic strain stagnates after necking initiation leads to the optimal fit. The combination of the equivalent plastic strains in the rupture zone and in another zone where there is a stagnation of the deformation gives the precise moment of the appearance of necking before rupture, and this allows a better identification, which made it possible to find the parameters that were used for the generation of the pseudo-experimental base. In Figure 2-14, identified and the pseudo-experimental curves (observables) completely superpose each other. Thus, giving sufficient information about the specimen's plastic strain state by increasing the number of observables, the optimal parameter set can be reached.

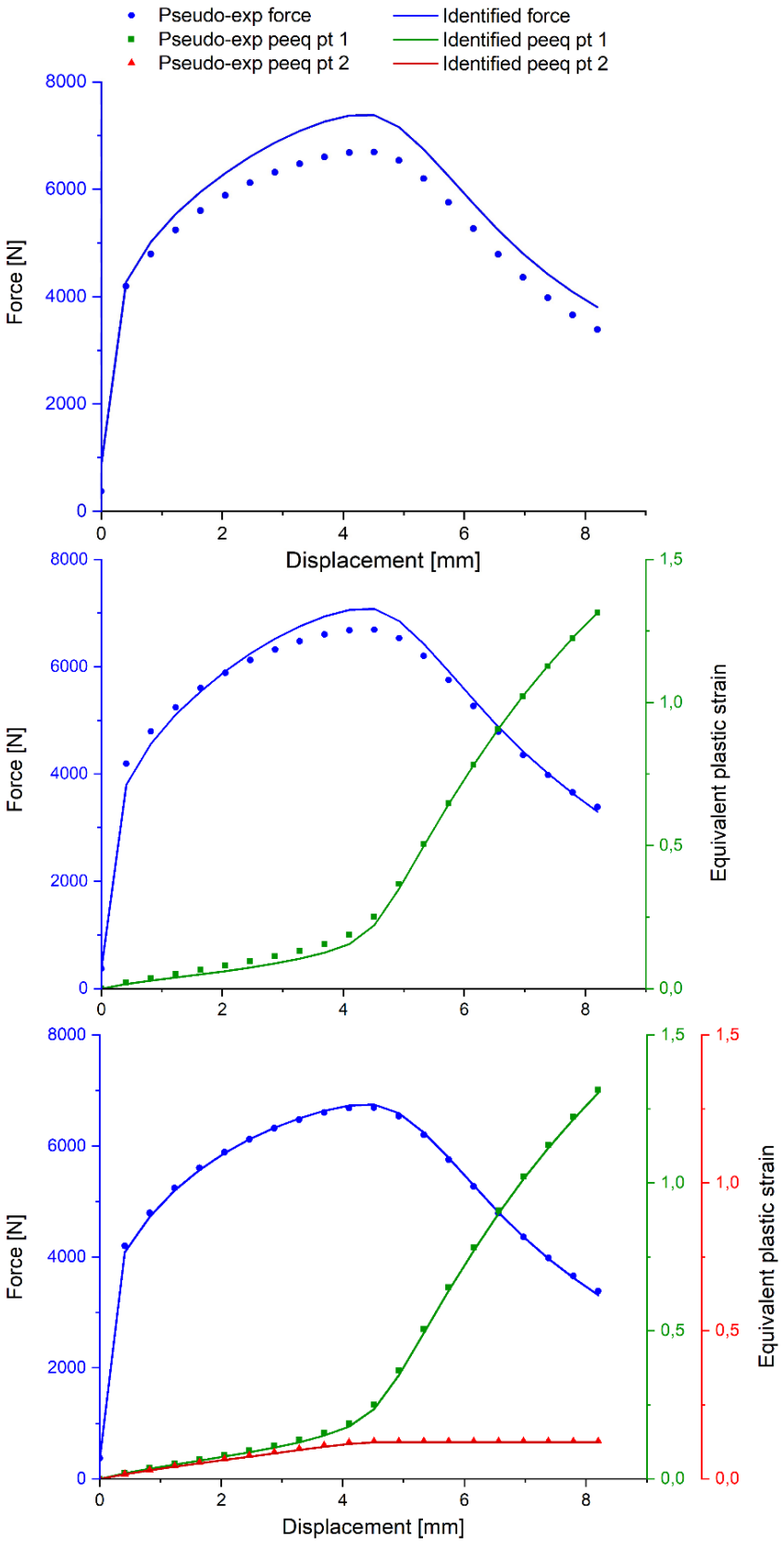

Figure 2-14: Identified and pseudo-experimental observables curves for the three cases.

In summary, by combining the identified parameters in Table 2-7 with the plot of tensile force and plastic strains with respect to displacement in Figure 2-14, the number of observable influences is well highlighted. Confirming the reliability of the algorithm and the proposed strategy of the inverse identification.

2.4.5. Inverse identification from experimental database

Based on the investigation realized in the validation of the inverse identification strategy on the pseudo-experimental database, the same identification procedure algorithm and strategy are used in real experimental data obtained from the tensile test on the specimen with a variable cross-section cut from the DC06EK sheet metal. So, likely the third case, the observables consist of tensile force, equivalent plastic strain (PEEQ 1) at the rupture zone, where either bifurcation occurs or a significant increase in plastic strain is observed, and the equivalent plastic strain (PEEQ 2) at another zone where plastic strain stagnates after necking initiation.

2.4.5.1. Selection of parameters

For this inverse identification on experimental data, unlike the first one, Ludwick hardening law (equation 1-21) is used, as presented Table 2-8. Ludwick law is used instead of Voce law because the hardening parameter "n" will be used to determine the analytical FLC using the Keeler and Brazier model, as detailed in subsection § 1.7.3.1 (equation 1-27).

Table 2-8: Ludwick hardening law and GTN damage model parameters to be identified.

Ludwick law			**GTN model**		
σ_0	K	n	f_N	f_C	f_F

2.4.5.2. Identification results

Figure 2-15 presents a comparison between the experimental observables and the identified results. The experimental curves effectively align the identified results, particularly in terms of tensile force and plastic strains. The transition where plastic strains bifurcate into two zones: one exhibiting localized strain and the other showing strain stagnation (indicating the onset of necking) is accurately captured.

Subsequently, the force drop (P zone), signifying rupture, is observed, after which the curves may diverge in different directions.

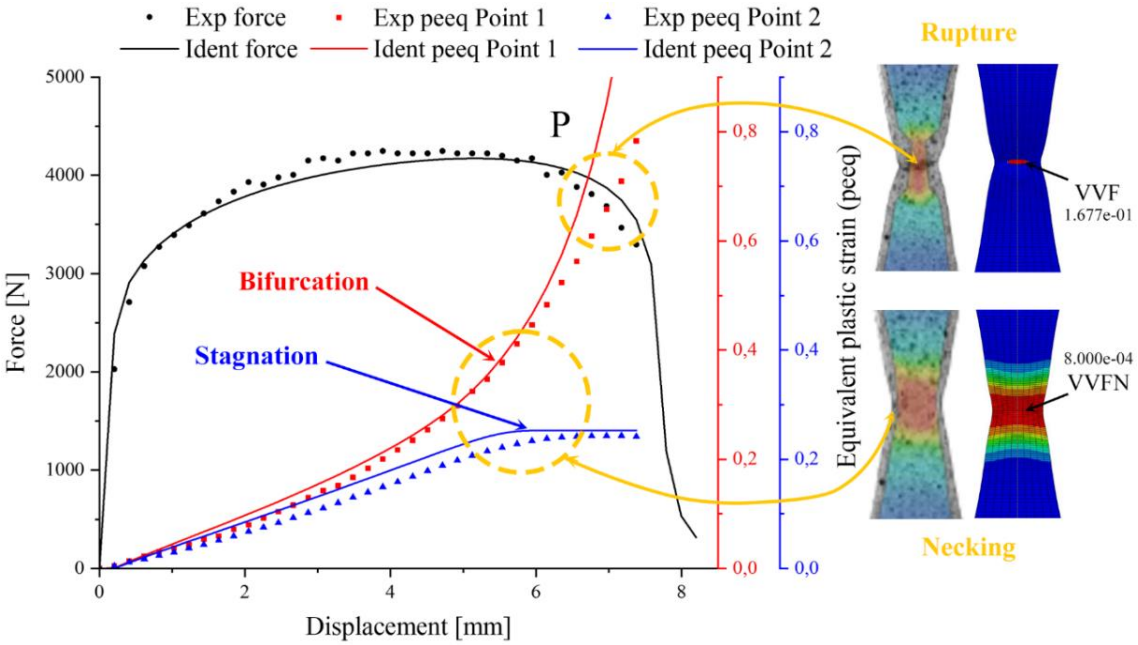

Figure 2-15: Comparison between identified and experimental results of forces and equivalent plastic strains.

Additionally, numerical cartographies of the void volume fraction due to nucleation (VVFN) and the total void volume fraction (VVF) were shown for comparison with experimental observations of necking and rupture Figure 2-15. The VVFN cartography was taken at the moment when plastic strain bifurcates in the central zone while stagnating in the other zone. At this stage, the tensile displacement was 6.085 mm, with a nucleation parameter f_N identified as 0.0009, coinciding precisely with the onset of necking. As for rupture, it occurs at the center of the specimen at a tensile displacement of 7.261 mm, where the critical final void volume fraction f_F approximately 0.17 was reached, as depicted in the VVF cartography and summarized in Table 2-9.

Table 2-9 summarizes the identified parameters for Ludwik's law and the GTN model. The identified GTN model parameters show strong alignment with those reported by D. Banabic et al. [121] and Y. Bouktir et al. [120]. However, the parameters for Ludwik's law differ from those in [11], particularly the parameter "K," which represents material consistency and σ_0 which represent the yield stress.

Table 2-9: Coupled Ludwick law and the GTN damage model Identified parameters.

	Ludwick law			GTN damage model		
Parameters	σ_0 [MPa]	n	K	f_N	f_C	f_F
Identified	**138.48**	**0.49**	**373.05**	**0.0009**	**0.0230**	**0.1724**
Reference [120,121]	152.00	0.25	433.59	0.0008	0.0219	0.1677
Error	13,52	0,24	60,54	0.0001	0,0011	0,0047
Reference [11]	100.00	0.46	521.46	Not used		
Error	38,48	0,03	148,41			

The observations for the Ludwick hardening law parameters reveal some deviations. The yield stress ($\boldsymbol{\sigma_0}$) shows discrepancies of 13.52 MPa and 38.48 MPa, depending on the reference. The strain hardening exponent (n) exhibits errors of 0.24 and 0.03, with the larger deviation highlighting differences in plastic behavior assumptions. The hardening coefficient (K) also shows discrepancies, 60.54 MPa and 148.41 MPa, indicating variations in strain hardening behavior.

Regarding the GTN damage model parameters, the initial void volume fraction ($\boldsymbol{f_N}$) and critical void volume fraction ($\boldsymbol{f_C}$) have small errors (0.0001 and 0.0011), demonstrating good agreement with reference values. However, the failure void volume fraction ($\boldsymbol{f_F}$) presents a slight deviation (0.0047), which could impact the accuracy of damage evolution predictions. These discrepancies can be attributed to differences in material microstructure, as DC06EK sheets may originate from different manufacturers, leading to variations in composition and processing history.

Additionally, laboratory test conditions and the method of material characterization significantly influence the results. Despite these errors, the identified parameters remain within a reasonable range, confirming that the model provides a sufficiently accurate representation of material behavior. Further refinements, such as improved optimization approaches or additional experimental validation, could help reduce these discrepancies.

2.5. Conclusions

This work aimed to enhance the numerical simulation of the deep drawing process through the experimental characterization of the mechanical behavior of DC06EK sheet metal. Tensile tests were conducted on specimens with constant cross-section at 0°, 45°, and 90° orientations relative to the rolling direction. The mean anisotropy coefficient ($R \approx 1{,}95$) and its deviation ($\Delta R \approx 0{,}10$) confirmed the confirmed the high anisotropy of the DC06EK sheet.

Although quadratic plasticity models like Hill 48 provide a good approximation, they fail to accurately capture the normal anisotropy of DC06EK. Alternative non-quadratic models, such as Hershey-Hosford and Logan-Hosford, offer better agreement with experimental observations, particularly under biaxial stress conditions. Further experiments, especially biaxial tests, are necessary to fully characterize the anisotropy of DC06EK steel.

An inverse analysis procedure was implemented to identify the parameters of the hardening law coupled with the GTN damage law. This strategy was numerically validated using a pseudo-experimental database. The identification process compared numerical results with global and local observables across three test cases:

1. **Global observable only**: Used tensile force as the sole parameter.
2. **Global and local observables**: Added the equivalent plastic strain at the rupture zone, where bifurcation or significant plastic strain occurs.
3. **All observables**: Included the equivalent plastic strain at a shifted zone where strain stagnates after necking initiation, alongside other parameters.

The identified parameters show good agreement when both local and global observables are used, enhancing the accuracy of the inverse identification technique. Notably, in the third case, the identified parameters closely matched the pseudo-experimental database. The third case allowed to find the parameter set used to generate the experimental database with a very low error (~2%) between numerical predictions and experimental observables.

After validating the inverse identification procedure, the GTN damage model parameters coupled with the hardening law were identified using real experimental data for DC06EK sheet metal. The results demonstrated a strong correlation between numerical prediction and experimental observations, with the identified parameters closely aligning with those reported in previous studies. The proposed identification strategy proved both effective and robust for material characterization. By integrating both local and global observables (tensile force and plastic strains), the approach significantly enhances parameter identification accuracy. This represents a substantial improvement over traditional strategies that rely solely on either global or local observables, enabling optimal parameter determination.

The simultaneous identification of hardening laws and damage model parameters ensures precise material characterization and modeling, which is critical for predicting defects such as necking and rupture. The analysis of the VVFN allowed accurate identification of the point where plastic strains bifurcate into two zones: one showing increased plastic strain and the other exhibiting plastic strain stagnation. This bifurcation corresponds to the onset of necking and aligns with the foundational principles used to establish forming limit curves. Similarly, the occurrence of rupture in the central zone was effectively captured by the VVF. The selection of the hardening law, whether coupled or uncoupled with the GTN model, plays a significant role in accurately representing material behavior.

Chapter 3. Simulation of deep drawing of a wheelbarrow tray with industrial parameters

3.1. Introduction

This chapter explores the potential of the GTN damage model as an alternative to the conventional Forming Limit Curves (FLCs) traditionally employed in industrial deep-drawing applications. The investigation focuses on a practical case study conducted at the local Algerian company "EIMS of Miliana" [1]. The deep-drawing process (DDP) can be simulated by integrating the GTN model into the Abaqus commercial finite element analysis software.

To achieve this, a choice was made between three numerical studies carried out using industrial parameters reflecting the practices of machine operators at the EIMS company. The first study is a numerical simulation of the DDP on a gas-heater body in the shape of a box [124]. The second one, conducted by Belguebli et al. [11], analyzed the formability and optimized the deep-drawing process for a wheelbarrow tray (WBT). The third study, by Hadj Amar et al. [10], investigated the extra-deep drawing of a bathtub, focusing on enhancing formability and product quality by controlling non-uniform blank holder pressures (BHP). In these studies, DC06EK sheet metal is used, and the formability through FLCs was analyzed under various BHP conditions.

In this numerical simulation, the parameters identified for Ludwik's hardening law and the GTN damage model, as described in section § 2.4, were applied to the WBT deep-drawing process. A comparative analysis was performed between two simulation approaches: one incorporating the GTN damage model and the other without it. The WBT was selected for this comparison due to its relative simplicity compared to the bathtub and gas-heater body in the shape of a box model.

3.2. Presentation of projects on products manufactured by deep drawing

To address the requirement of the EIMS company, different numerical simulations were performed in previous research work in the Mechanics and Rheology Laboratory, Faculty of Technology – University of Chlef. These research works are briefly presented below:

3.2.1. Gas-heater body

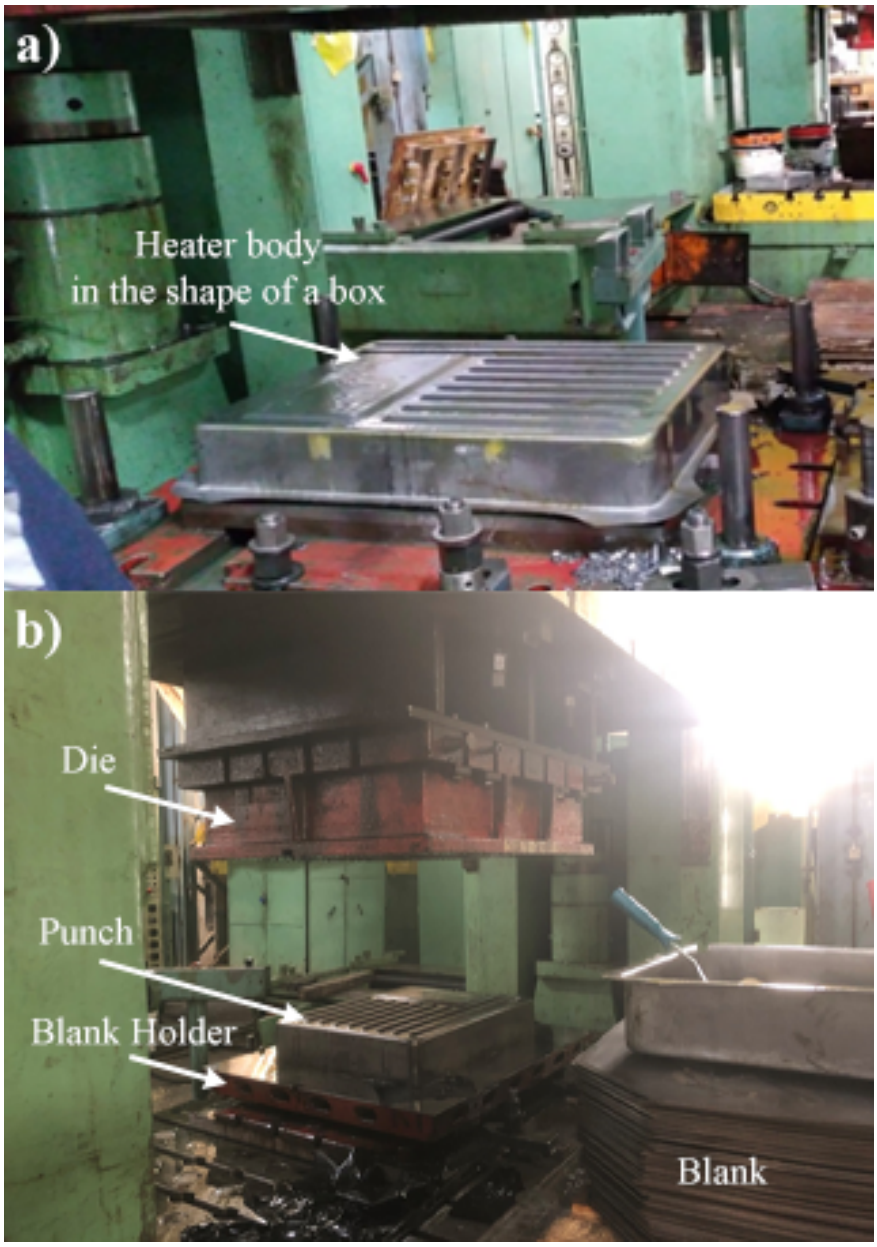

Figure 3-1 : Deep drawing of heater body in the shape of a box [124].

The production of gas-heater bodies at EIMS is primarily carried out through deep drawing. This product is typically made from six parts: the heater body in the shape of a box, the heater body in the shape of a plate, the nozzle, the deflection chamber, the small-format discharge casing, and the large-format discharge casing. The heater body in the shape of a box is done by deep drawing operation (Figure 3-1-a) in a press named ZE500-25 (Figure 3-1-b). As an example, Figure 1-6-c illustrates the rupture defect in the heater body.

A numerical simulation of the deep drawing process was carried out on the gas-heater body in the shape of a box, the most affected part, with industrial parameters used in EIMS in order to prevent the defects mentioned above. The used numerical model is illustrated in

Figure 3-2 including the boundary conditions, mesh type, and the total number of elements.

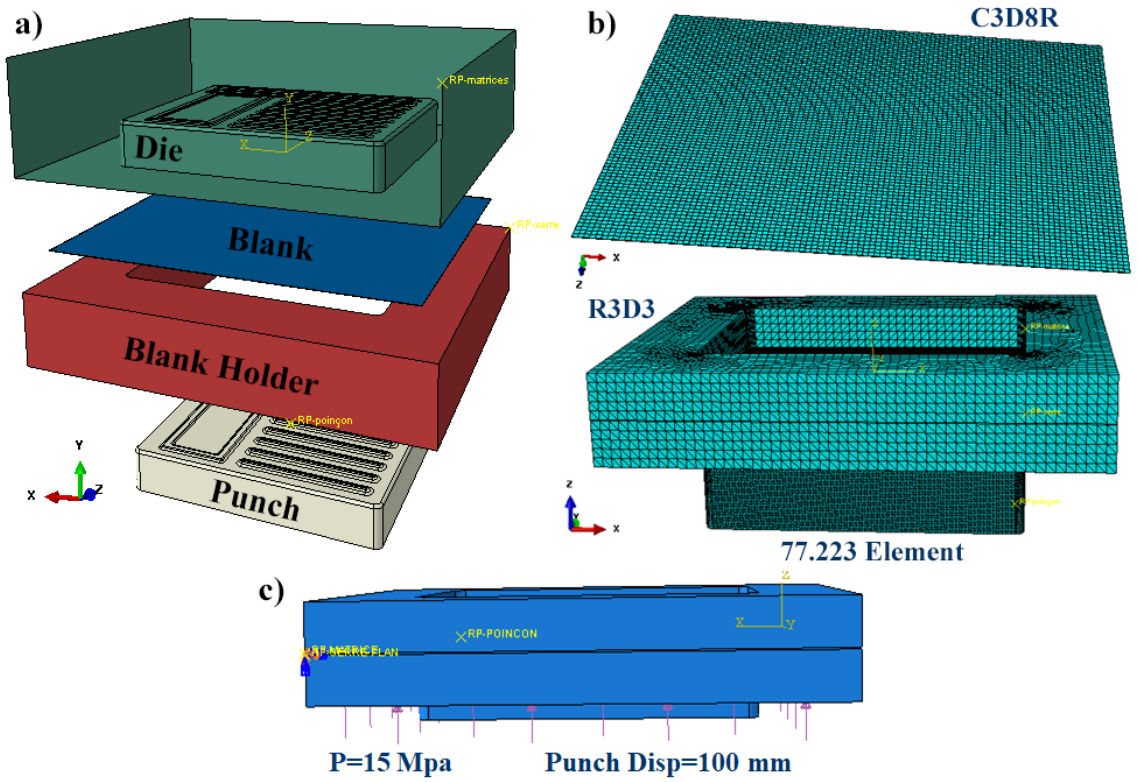

Figure 3-2 : Numerical simulation of heater body in the shape of a box.

3.2.2. Wheelbarrow Tray

Similarly, the wheelbarrow tray is also obtained by deep drawing, but it is not obtained from the same deep drawing press. The used press is named BZE1600-32. This press is different from the ZE500-25 machine, since in the BZE1600-32 different pressures are generated on the blank holder via six hydraulic cylinders.

Figure 3-3 illustrates the BZE1600-32 press, the deep-drawn wheelbarrow tray, and the final product after assembly.

Figure 3-3 : a) BZE1600-32 Press b) Semi finished wheelbarrow tray product, c) Final product [28].

Poor control of the applied pressures to the blank holder leads either to rupture or to the appearance of wrinkling during deep drawing (example of wrinkling in Figure 1-6-a). To avoid these two defects and improve the quality of this product, a numerical simulation of the deep drawing operation of the wheelbarrow tray product (Figure 3-4) with the same industrial parameters was performed by A. Belguebli [11,28].

In this study the FLCs were used to assess the formability and damage of the sheet metal during the DDP.

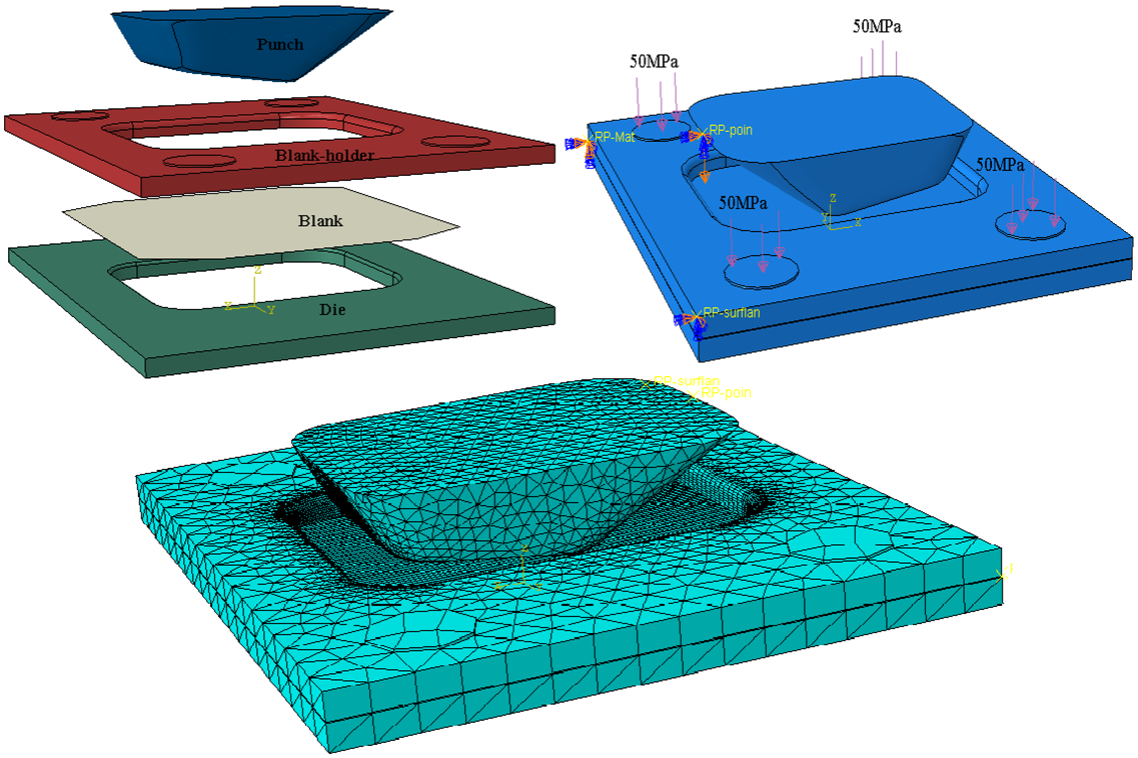

Figure 3-4 : Assembly, boundary conditions and mesh for the numerical simulation of wheelbarrow tray [11,28].

The WBT was selected for numerical simulation due to its relative simplicity compared to the bathtub and gas-heater body in the shape of a box model.

3.2.3. Bathtub

For bathtubs, the same deep drawing press (BZE1600-32) previously mentioned is used to manufacture bathtubs. Here, we talk about the extra-deep drawing process of bathtubs because the depth reaches about 400mm. Figure 3-5-a presents the deep-drawn bathtub and BZE1600-32 press, which is equipped with six actuators that control the blank holder pressures (BHP). A research work was conducted by Hadj Amar et al. [10], investigated the extra-deep drawing of a bathtub, focusing on enhancing formability and product quality by controlling non-uniform BHP. In this study the FLCs were used to assess the formability and damage of the sheet metal during the DDP. In addition, the semi-finished bathtub is illustrated in Figure 3-5-b and the assembly view of the numerical model is illustrated in Figure 3-5-c.

It should be noted here that it is absolutely necessary to consider all industrial parameters for the success of the numerical simulation: blank anisotropy, blank holder pressures, cutting of the blank corners, and the draw beads.

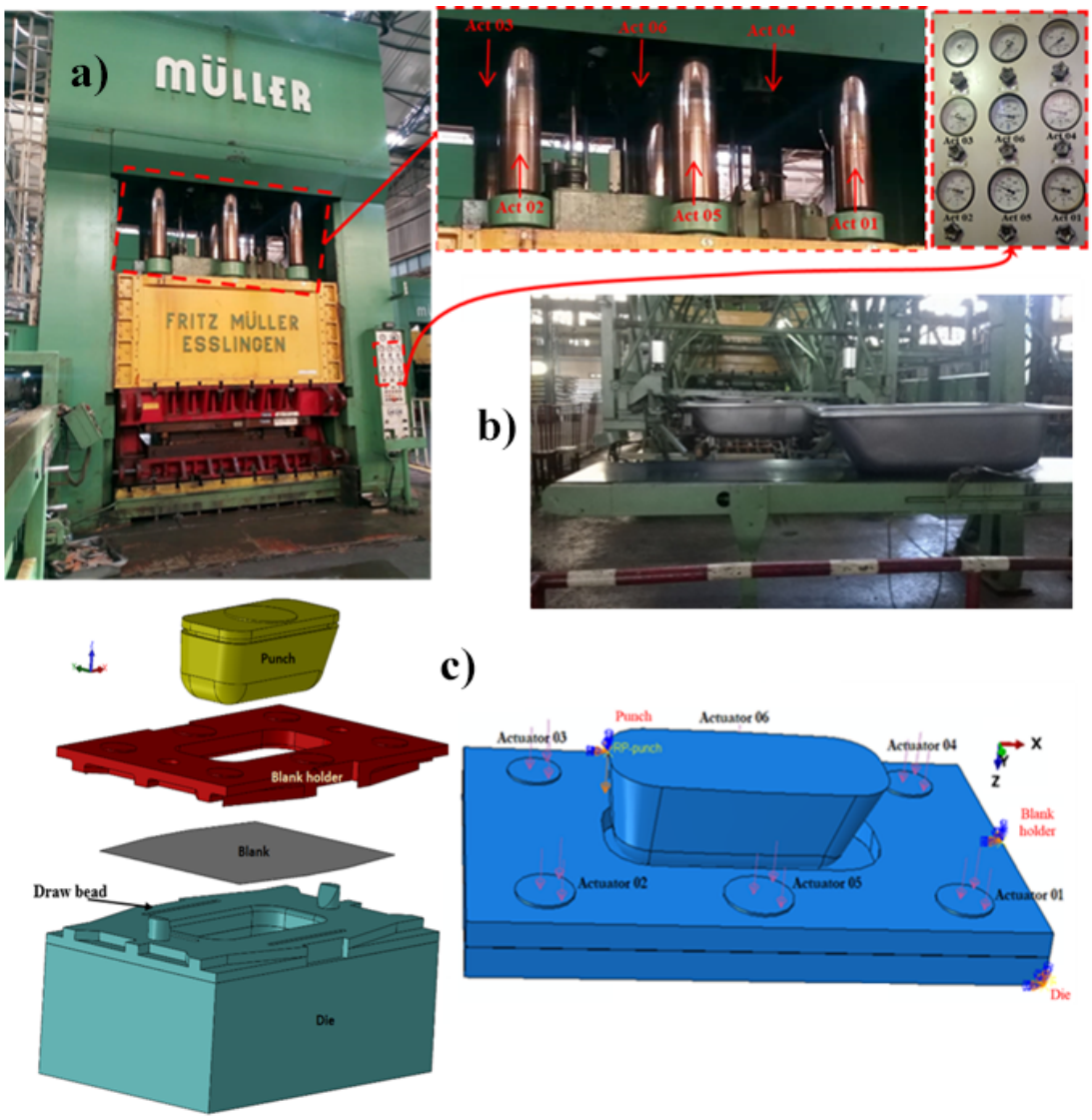

Figure 3-5 : a) BZE1600-32 press, b) Semi-finished bathtub c) Numerical model of the bathtub [2].

3.3. WBT deep-drawing process

The production of wheelbarrows at EIMS company is primarily carried out through deep drawing. Before the drawing operation, the sheet metal (the blank) (Figure 3-6-a) is loaded using a blank loader equipped with a vacuum pump. Subsequently, the blank is transported to the deep-drawing press (named BZE1600-32) using a motor reducer and rack system.

The BZE1600-32 press is a heavy-duty hydraulic machine (Figure 3-6-b) with a capacity of 1600 tons (600 tons for the punch and 1000 tons for the blank holder). This type of press represents a significant investment and is typically purchased for a lifespan of around forty years. The press consists of a ram controlled by seven actuators: six actuators for the blank holder, one actuator for the punch, and an ejector under the die. Three pumps are used to supply these cylinders, generating the following pressures:

- Blank holder pump: 0-1000 bar
- Ram pump: 0-600 bar
- Ejector pump: 0-50 bar

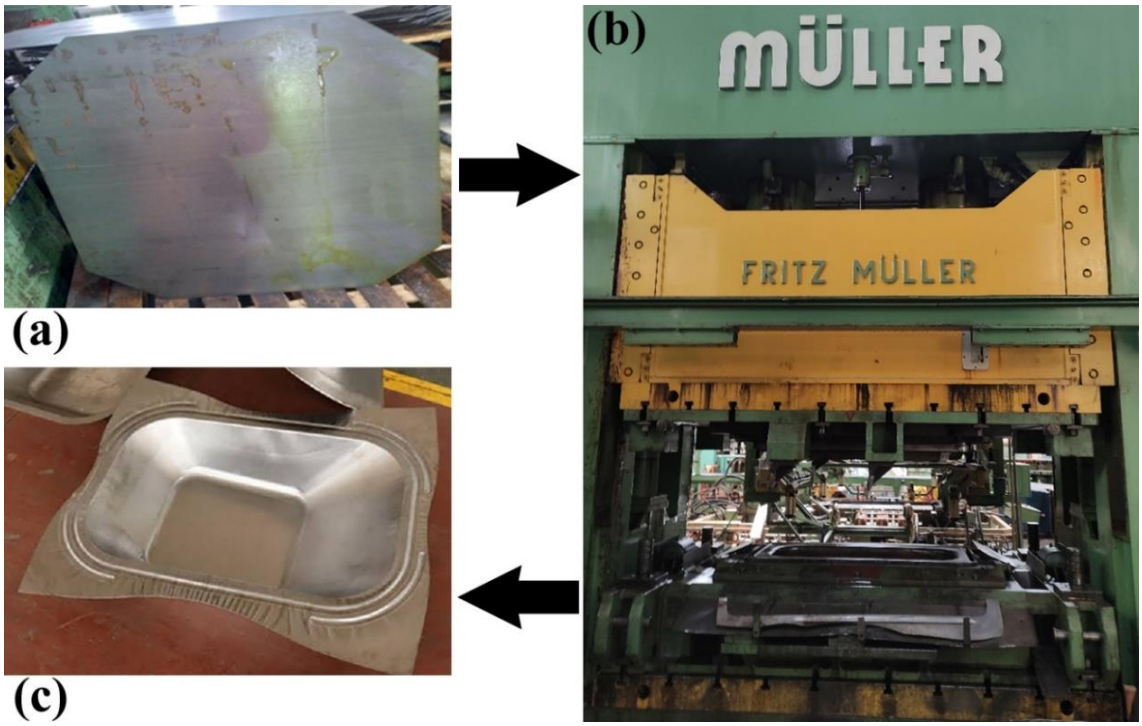

Figure 3-6: Deep drawing operation for the WBT: (a) DC06EK sheet metal, (b) BZE1600-32 press, (c) semi-finished product.

Before the drawing operation, the four corners of the sheet are cut (Figure 3-6-a) to ensure precise clamping and allow proper flow of the blank between the die and blank holder, thereby preventing rupture and wrinkling. The blank is manually lubricated before being clamped by the blank holder to ensure a lubricated contact between the blank and tools. Lubrication is crucial as it facilitates material flow under the BHP and ensures the success of the deep-drawing operation.

The blank holder secures the blank in place. In the deep drawing of the WBT, only four actuators are used. Subsequently, the punch descends, plastically deforming the blank to form the WBT (Figure 3-6-c).

After the deep-drawing operation, the WBT is transferred to a second press (BZE600-32) for trimming, bending, and punching. The BZE600-32 press is designed for trimming and bending the edges of the WBT (Figure 3-7). This is achieved by the descent of a ram controlled by a double-acting hydraulic cylinder at a pressure of 400 bar. Once trimming is complete, the ram retracts, and the WBT is ejected from the press.

Figure 3-7: Trimming and bending operation for the wheelbarrow tray.

Subsequently, the WBT is positioned on a punching machine to create holes for assembling the wheelbarrow chassis. The finishing line involves several tasks:

- Fixing the tray to the chassis using screws to produce the final product, the "wheelbarrow" Figure 3-8).
- Painting the wheelbarrow.
- Visual inspection and repair.
- Once the manufacturing operations are complete, the finished wheelbarrows are stored on wooden pallets for delivery to the commercial department.

Figure 3-8: Assembly of the final wheelbarrow tray product.

3.4. Defect modes in deep drawing of the WBT

In an increasingly competitive industrial context, manufacturing costs and lead times are crucial factors. For deep drawing processes, acceptance criteria can vary, relating to issues of mechanical strength, dimensional tolerances, or surface quality. By its very nature, deep drawing involves a compromise between shrink draw and stretching deformations, where the respective limits are wrinkling and necking/rupture phenomena, which serve as basic rejection criteria. Additional causes for rejection may include dimensional tolerances, springback, and surface finish.

Reducing the rejection rate of manufactured parts to save time and costs is essential. In the deep drawing of WBTs, the observed defect types are illustrated in Figure 3-9. These defects include:

- **Wrinkling:** This corresponds to the appearance of undulations or blisters on the deformed part during forming processes (Figure 3-9-a). It is a shape defect caused by one or more compressive stresses. Wrinkles can occur in both the elastic and plastic domains. They are generally associated with shrink draw deformations and can appear in areas of the blank that are temporarily not in contact with the die, punch, or under the blank holder. They may also result from forming stresses or residual stresses released after punch withdrawal and part extraction from the die. In practice, wrinkles typically form in the plastic deformation domain during material forming. They can also occur in non-contact areas of the part, i.e., areas not in contact with the forming tools (punch, die, and blank holder).

  They can arise due to:

  - Insufficient BHP;
  - Punch dimensions being much smaller relative to die dimensions (large gap between die and punch);
  - Existing ridges or defects in the tools;
  - Excessive distance between the blank holder and die;
  - Over-lubrication (very low friction).

- **Rupture:** This is characterized by the presence of a crack (fracture or tear) in the formed part (Figure 3-9-b). For the deep-drawing operator, visible onset necking has the same significance as rupture since the two phenomena are closely related in terms of deformation. Rupture may stem from a local necking or a defect on the blank wall. In deep drawing operations, these two defect modes occur due to tensile and compressive forces. Excessive forces in critical regions may lead to rupture. Rupture can occur at the start or during the forming operation, often resulting from poor control of clamping force and/or ineffective non-lubricated contact, causing excessive frictional.

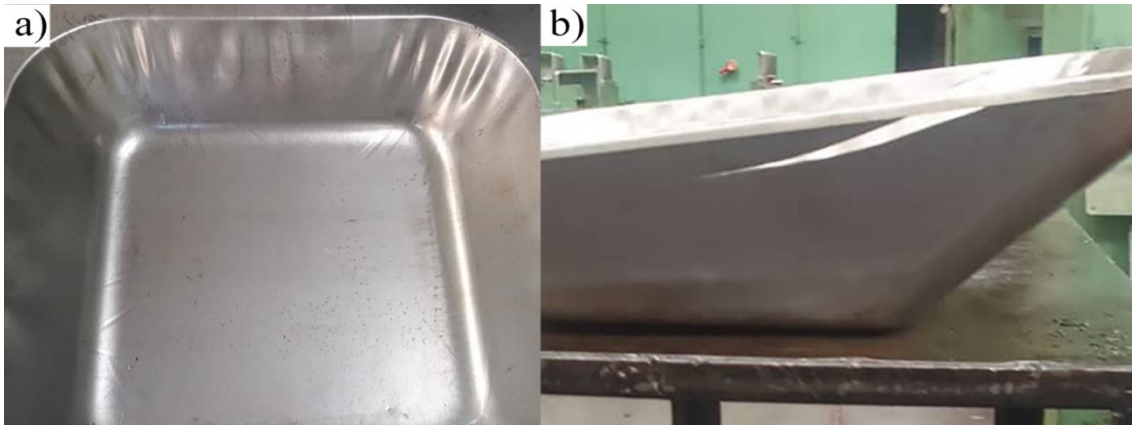

Figure 3-9: Deep drawing defects: (a) Wrinkling, (b) Rupture.

Deep-drawing machine operators typically adjust BHP values based on their experience to produce semi-finished products free from rupture or wrinkling defects. These direct machine trials are costly in terms of time, materials, costs, and production rates. Moreover, achieving a successful semi-finished product is not necessarily the result of experimental trial techniques.

As deep drawing applications become increasingly relevant, the industrial manufacturer seeks to enhance production levels by:

- Reducing production costs;
- Increasing production rates;
- Eliminating potential defects that may arise during or after forming.

To address this issue, we aim to apply numerical simulation, a type of computation that allows the simulation of complex and real physical events, such as rupture and wrinkle development.

3.5. Finite element model of WBT DDP

The deep drawing process of the WBT, described in section § 3.3, is modeled using the finite element method with the ABAQUS/Explicit software under industrial parameters, using the same numerical model of A. Belguebli et al. [11]. The process simulation flowchart is illustrated in Figure 3-10.

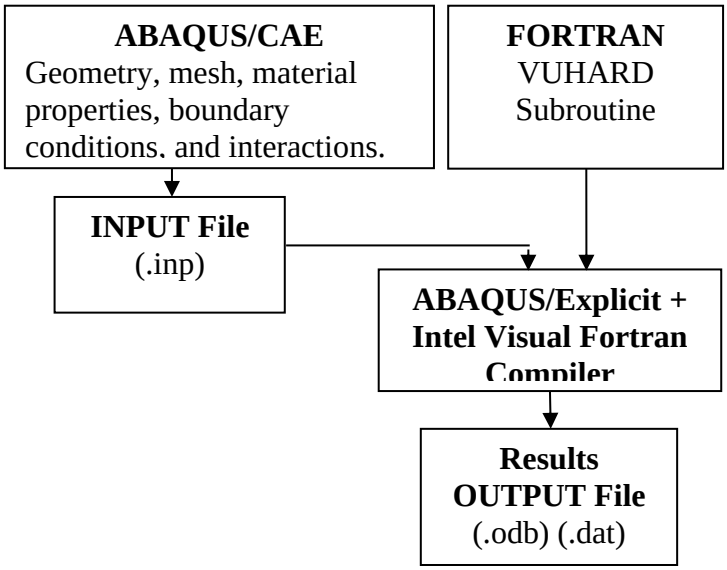

Figure 3-10: Flowchart of the numerical simulation of the WBT deep drawing process.

Figure 3-11-a shows the assembly of the different tools with the blank. The tools are considered rigid and non-deformable due to their high stiffness, whereas the blank is modeled as a deformable body. For the blank mesh, the S4R element type is used. This is a 4-node quadrilateral shell element with reduced integration and a large-strain formulation [125,126], allowing the elements to deform in the transverse shear plane. For the tools, R3D3 triangular 3-node rigid elements were selected, with refinement applied to radii and fillets.

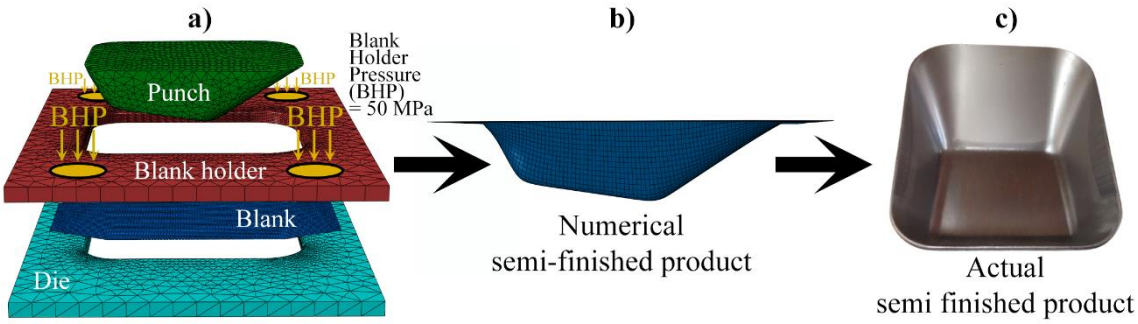

Figure 3-11: (a) Numerical model of the WBT including boundary conditions, (b) Numerical semi-finished product, (c) Actual semi-finished product.

The number of elements and mesh type used for each part in the numerical modeling are presented in Table 3-1.

Table 3-1: Number of elements and mesh type for each part.

Part	Number of Elements	Mesh Type
Punch	4886	Triangular “R3D3”
Die	7846	Triangular “R3D3”
Blank holder	6922	Triangular “R3D3”
Sheet metal	8840	Quadrilateral “S4R”

The DC06EK steel sheet used in the numerical simulation was represented with isotropic elastoplastic behavior. Elastic behavior was described using Hooke’s model, with a Young’s modulus E=210000 MPa and Poisson’s ratio ν=0.3. For plastic behavior, Ludwick’s identified hardening law and the GTN damage model were integrated into the numerical model to evaluate formability. It should be noted that, two simulation approaches will be compared: with and without the GTN damage model.

The GTN model parameters were directly input into ABAQUS/Explicit. Meanwhile, Ludwick’s hardening law was implemented in ABAQUS/Explicit via a VUHARD subroutine. The parameters for the GTN model and Ludwick’s hardening law are detailed in subsection § 2.4.5.2 and given in the Table 2-9.

In the numerical modeling, the blank was positioned between the die and the blank holder. A "surface-to-surface" contact type was defined to specify the direct contact surfaces, using the “Master-Slave” concept. This specific type of contact describes the mechanical interaction between a deformable surface (sheet metal) and rigid surfaces (die, punch, and blank holder). Figure 3-12, Figure 3-13, and Figure 3-14 represent surface-to-surface interactions.

During the deep-drawing operation, all contact surfaces were assumed to be lubricated. Coulomb’s friction law was employed to describe the sliding interaction between the sheet metal and the tools. A constant and uniform friction coefficient of 0,175 was applied to all interactions.

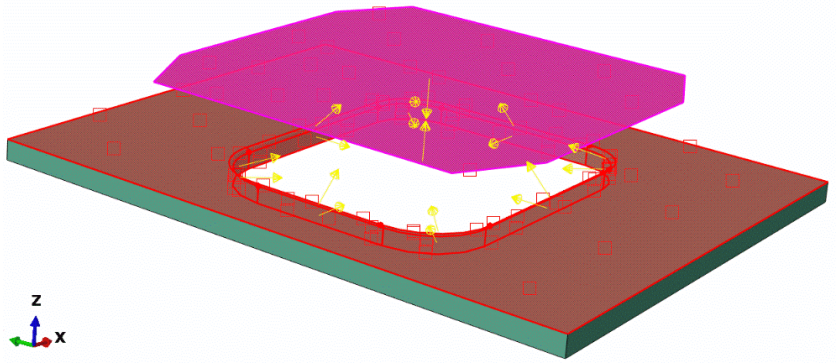

Figure 3-12 : Interaction between blank and die.

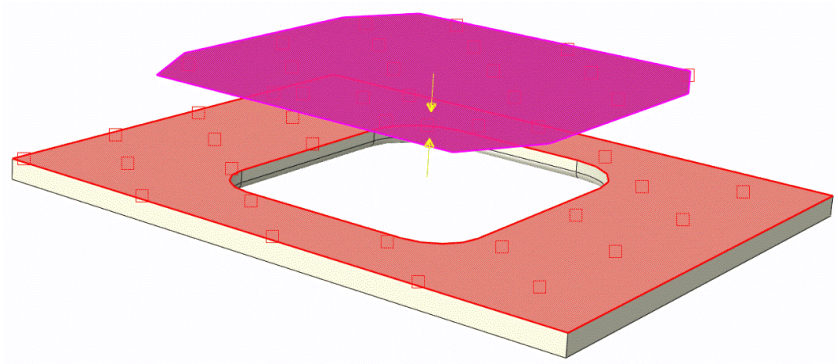

Figure 3-13 : Interaction between blank and blank holder.

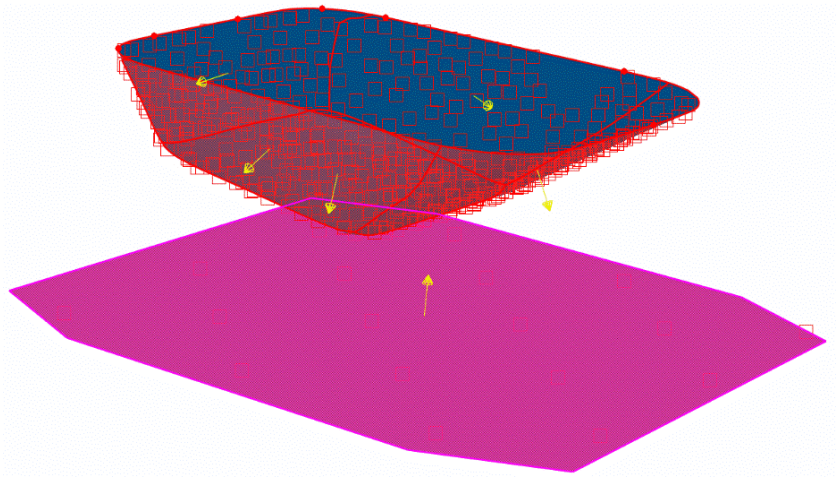

Figure 3-14 : Interaction between blank and punch.

Boundary conditions define the actions of the tools and the pressure applied by the blank holder. These boundary conditions replicate the actual deep drawing operation of the WBT at EIMS company and were applied in the numerical simulation. Movements and constraints were applied to the tools via reference points. The reference point designated on the punch was also used to measure the reaction force as a function of displacement.

The numerical model including boundary conditions is illustrated in Figure 3-15 and described below:

1. **Punch:** A displacement of 220 mm was applied to the reference point along the Z-axis (central axis). This displacement was executed at a constant velocity.
2. **Blank Holder Pressure (BHP):** The BHP consists of four independently controlled cylinders (Figure 3-15).
    - A pressure of 50 MPa was applied to each cylinder on the blank holder's upper surface. This corresponds to the pressure used by the machine operator to produce a defect-free WBT.
    - Additional pressures were applied to study and analyze the occurrence of rupture and wrinkling defects. The aim was to determine the lower and upper pressure limits for producing defect-free products.
    - The applied pressures remained constant throughout the deep-drawing operation.
3. **Die:** The die was considered fully fixed, meaning it remained in a stationary position during the simulation.

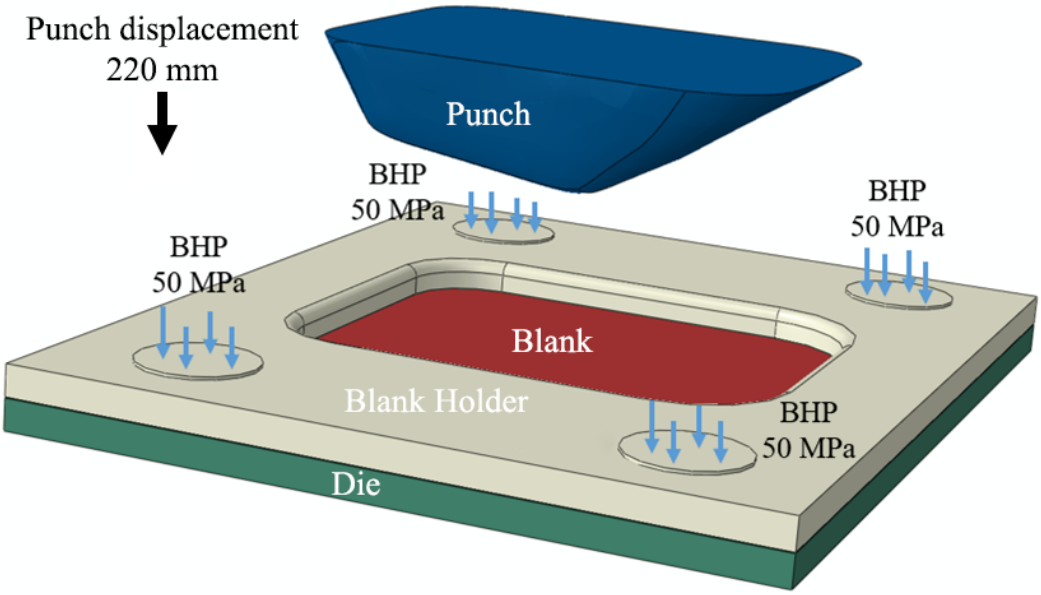

Figure 3-15 : Boundary conditions.

3.6. Results and Discussions

3.6.1. Validation of numerical simulation

In this step, thickness variation measurements in the final product were performed to validate the numerical model of the WBT. The thickness reduction in the WBT was measured using the ultrasonic device "SOFRANEL EHC 09B" (Figure 3-16-a), with a precision of 0.01 mm. Measurements were taken at various sections of the WBT, as shown in Figure 3-16-b): longitudinal (AA), transverse (BB), and diagonal (CC).

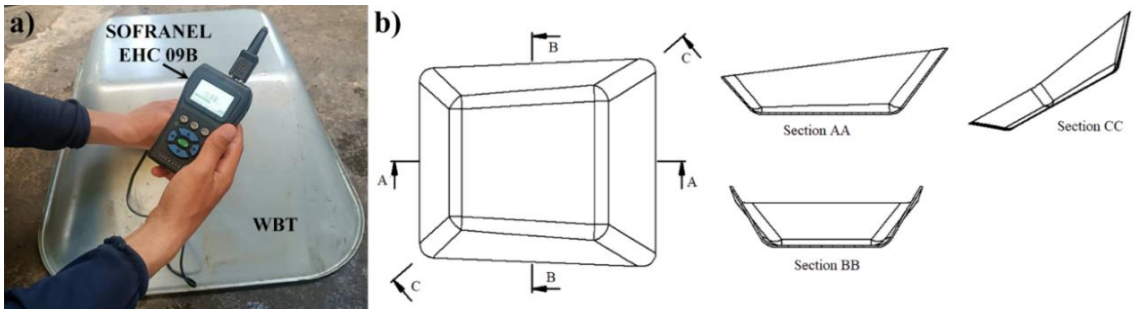

Figure 3-16 : a) Ultrasonic measuring device, b) Different WBT measurement sections.

The ultrasonic thickness measurements were compared to the numerical simulation results, both with and without the GTN model, across different sections of the WBT: longitudinal (section AA), transverse (section BB), and diagonal (section CC). The comparison shows good reproducibility, as depicted in Figure 3-17.

The root mean square error between the numerical results using the GTN model and the experimental measurements is 5%, slightly lower than the 6% observed without the GTN model. This suggests that incorporating the GTN model has a minimal effect on the plastic behavior of the sheet metal. The small discrepancies between the experimental and numerical results can be attributed to the following factors:

- The sheet metal may not have a uniform thickness of 1.6 mm before the DDP.
- A detailed characterization, including an anisotropic yield criterion, is required to accurately model the elastoplastic and anisotropic behavior of the sheet.
- Friction and contact definition between the sheet and the tools are critical. The friction coefficient must account for the materials of the tools, their surface finish, and the mixed lubrication conditions in the simulation.
- The implementation of GTN damage model in the numerical simulation demonstrated that the numerical DDP of the WBT closely matches the DDP of the defect-free WBT produced by the company.

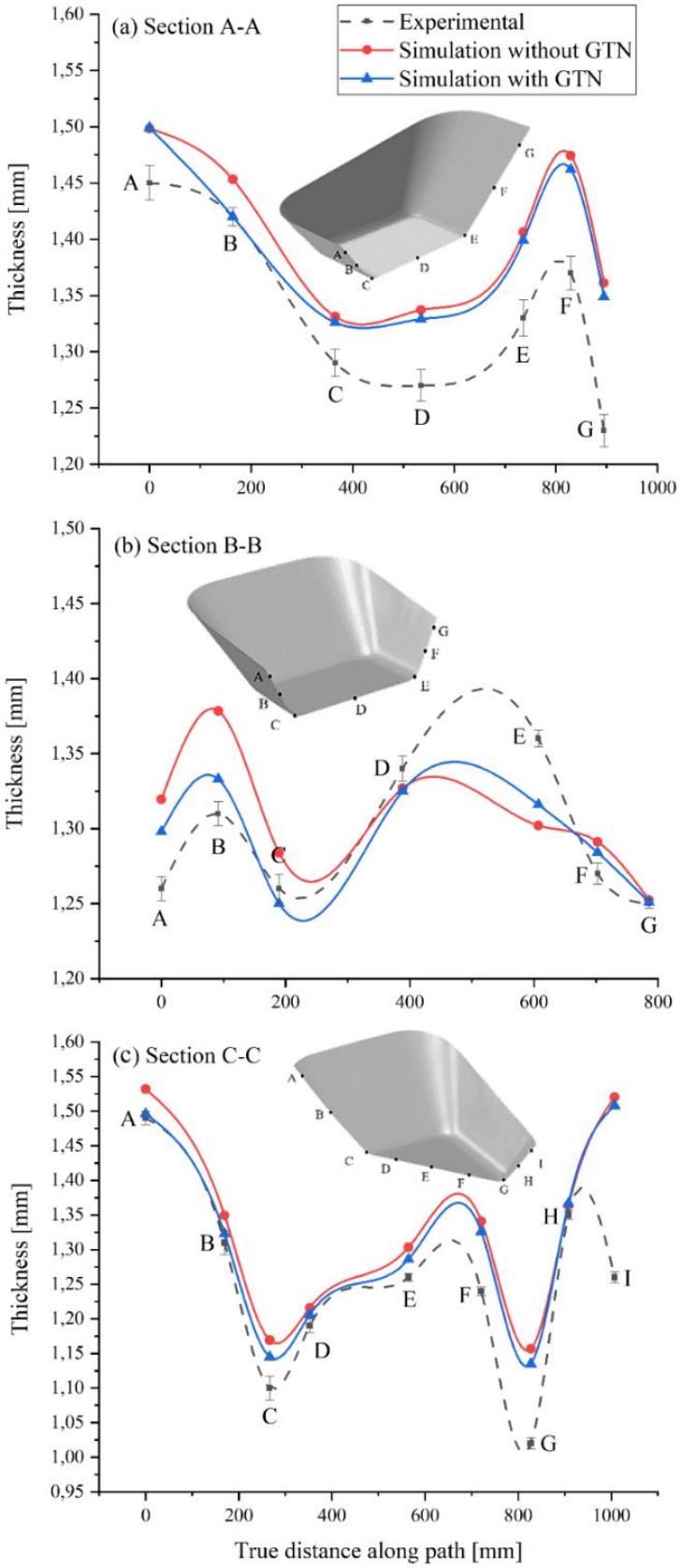

Figure 3-17 : Numerical and experimental thickness variation measurements across different sections.

3.6.2. Deformation modes

The deep-drawn WBT, illustrated in Figure 3-18, clearly exhibits several deformation modes. Zone "A" undergoes drawing deformation, where the variation in thickness remains almost constant. Zone "B" is stretched by the punch during its displacement, leading to plane stress tension. The corners (Zone "C") experience expansion, where the thickness deformation is greater than in the other zones, such as plane stress deformation and drawing deformation. In Zone "G," the thickness varies slightly, while the deformation mode is clearly equibiaxial stretching [127].

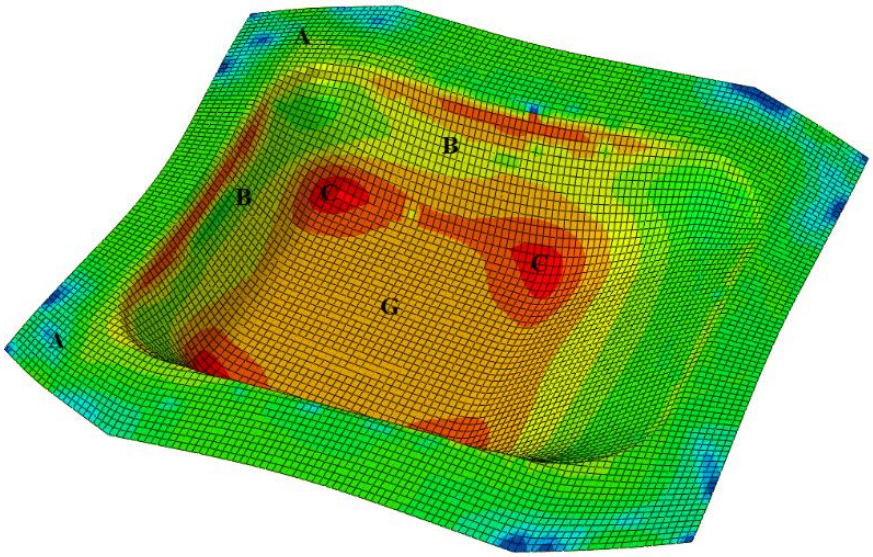

Figure 3-18 : Deformation zones in the WBT.

We can provide a more quantitative representation of the previous description by plotting the measured strains at various points on a strain diagram Figure 3-19. Based on this diagram, the deformation modes can be explained according to the following zones [27]:

In Zone A (Shrink drawing), a circle is stretched in the transverse direction, where the major strain is positive while the minor strain is negative ($\varepsilon_1 > 0$ and $\varepsilon_2 < 0$). Here, the diameter D_1 increases relative to D_0, while D_2 decreases ($D_1 > D_2$).

Zone B (Plane strain) represents a case of plane strain tension, where $\varepsilon_1 > 0$ and $\varepsilon_2 = 0$, with D_1 increasing relative to D_0, while D_2 remains unchanged ($D_2 = D_0$).

In Zone C (Stretching), both principal diameters increase relative to the initial diameter D_0, following the strain condition $\varepsilon_1 > \varepsilon_2 > 0$.

Finally, in Zone G (Equibiaxial Stretching), both diameters increase equally ($D_1 = D_2$) compared to the initial diameter D_0, with the strain condition $\varepsilon_1 = \varepsilon_2 > 0$.

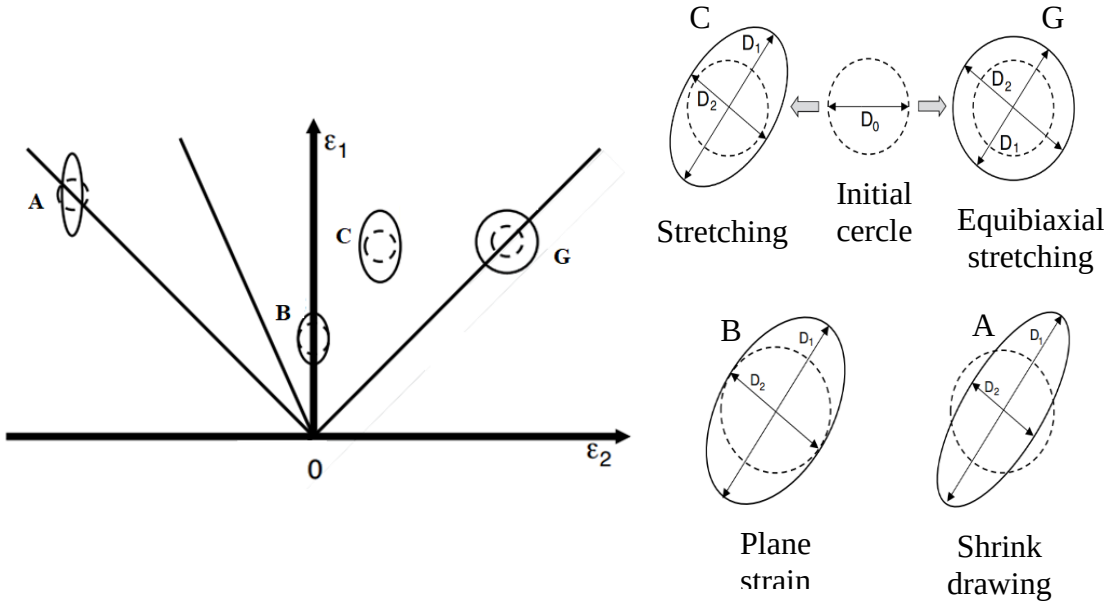

Figure 3-19 : Deformation modes in the WBT.

3.6.3. Triaxiality

In sheet metal forming, triaxiality is a key parameter that influences damage initiation and failure mechanisms. The stress triaxiality factor (η) is defined as [128]:

$$\eta = \frac{\sigma_m}{\sigma_{eq}} \qquad 3\text{-}1$$

where: σ_m is the mean stress (hydrostatic stress) and σ_{eq} is the von Mises equivalent stress (deviatoric stress component).

Triaxiality governs void nucleation, growth, and coalescence in ductile metals. High triaxiality promotes faster void growth and coalescence, leading to fracture, while low triaxiality delays these processes which causes an apparent increase in formability [128].

Additionally, under axisymmetric loading with a tensile axial stress, triaxiality can range from -2/3 (biaxial compression) to infinity (hydrostatic tension). In plastic plane strain, it varies between 0 (pure shear) and infinity (hydrostatic tension). However, in plane stress, triaxiality is limited to a range of -1/3 (compression) to 2/3 (biaxial tension). In practical applications, it typically falls between 1/3 and 2/3, except in cases where one stress component becomes negative, such as during deep drawing [129].

Moreover, Small values of the strain hardening parameter (n = 0.05) lead to a rapid increase of the stress triaxiality with the post-necking strain. Conversely large strain hardening parameters (n = 0.25), lead to a small increase of the stress triaxiality with post-necking strain [130].

The stress triaxiality of the used sheet metal was addressed directly in the finite element simulation software ABAQUS by selecting a field output variable named TRIAX or stress triaxiality, which is, this variable's cartography is illustrated in Figure 3-20.

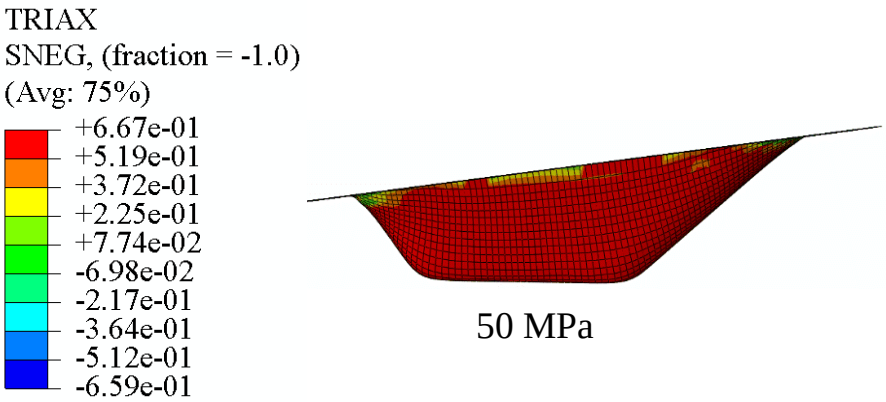

Figure 3-20 : Stress triaxiality distribution cartography.

In Figure 3-20, the legend on the left provides the triaxiality scale, ranging from -0.659 (blue) to +0.667 (red). This aligns with the theoretical range of -1/3 to 2/3 mentioned above.

For low blank holder pressure, the triaxiality distribution shifts toward negative values (blue regions). In this case, the material flows more freely, leading to higher compressive stress in the thickness direction and reduced triaxiality. As a result, this region is less likely to experience void growth and failure since lower triaxiality generally delays ductile fracture initiation.

Conversely, increasing the blank holder pressure up to value used at EIMS company (50 MPa), the triaxiality distribution shifts toward positive values (red regions), indicating a stress state approaching biaxial tension or plane stress conditions. This occurs because the increased BHP restricts material flow, leading to greater tensile stress in the radial and circumferential directions, this corresponds to our case where the stress triaxiality wasn't greater enough (≈ 0.67) to cause accelerated void growth to cause coalescence (Figure 3-20) justifying not reaching the critical void volume fraction to failure f_F in spite of reaching the critical void nucleation f_N value (Figure 3-21).

3.6.4. A Comparative Approach to Formability Prediction: GTN Damage Model vs. Traditional FLCs

The objective of this study, based on the DDP of an actual industrial application, was to predict and prevent wrinkling, necking, and ultimately rupture defects. The concern is to ensure that formability does not reach necking stage. Usually, a safety margin of 10% is considered by setting the FLCs slightly lower [131]. These margins help avoid the risk of necking by observing how closely the limit strains approach the FLCs.

As illustrated in Figure 2-15, when the critical value of f_N approximately 0.0009 is reached, plastic strain concentrates in one zone indicating the onset of necking, which is the basis for establishing FLCs. The critical value of f_F around 0.17 corresponds to rupture stage. For this reason, it is preferable to analyze the void volume fraction due to nucleation (VVFN) instead of the total volume fraction at failure (VVF). The VVF indicates total rupture, while VVFN reflects the initiation of damage. By controlling the critical nucleation values, coalescence and rupture can be prevented.

Figure 3-21 compares the numerical simulation results using Ludwick's hardening law with and without the integration of the GTN damage model, for different BHPs, including the equivalent plastic strain (PEEQ) cartographies for both simulations. Additionally, the VVFN and the VVF cartographies are provided for the simulation case with the GTN model. These cartographies help analyze the occurrence of wrinkles and rupture defects. For further illustration, the analytical FLC of the DC06EK sheet metal, with a thickness of 1.6 mm, as determined by Belguebli et al. [11] using the Keeler and Brazier model [54,132], is included.

Wrinkling defect appears in the cartographies at low BHPs up to 20 MPa for the simulation without the GTN model and up to 25 MPa for the simulation with the GTN model, as indicated by the purple color. Within this pressure range, the strain limits fall below the uniaxial compression line on the FLC. Successful deep drawing operations are observed within a BHP range of 25 to 50 MPa for the simulation without the GTN model and 30 to 50 MPa for the simulation with the GTN model. At 50 MPa, both simulations result in a defect-free product, consistent with the settings used by the company's machine operator.

Damage initiation in WBT occurs when the BHP reaches 60 MPa, as indicated in VVFN cartography, where voids reach the identified nucleation value of 0.0009. Based on this analysis, the recommended BHP range for producing a defect-free WBT is between 25 and 60 MPa.

We note that, the same hardening law, identified through inverse analysis, was used in both simulations, with and without the GTN model, as presented in in subsection § 2.4.5.2. The two simulations yield similar results, with minimal differences observed except for wrinkling, where the GTN model shows some influence in the PEEQ cartographies. The onset of necking is nearly identical in both cases.

According to Belguebli et al. [11], there is a notable difference in the identified parameters of the Ludwick hardening law for the same material, precisely the consistency coefficient "K" and the yielding stress "σ_0", as shown in Table 2-9. In that study, the recommended pressure range was 20 to 70 MPa, while in our study it was 25 to 60. Therefore, the integration of the GTN model or its absence affects the numerical results, particularly in terms of material behavior.

This numerical investigation demonstrates that integrating the GTN model impacts plastic deformation, particularly in predicting wrinkling, which varies depending on its use. The GTN model also identifies the onset of necking and damage initiation zones before rupture, as shown in the VVFN cartographies. However, the VVF does not reach critical rupture values, as observed experimentally (Figure 3-21). This can be explained by the fact that void growth predicted by the GTN model is insufficient to reach accelerated growth and coalescence, likely due to low stress triaxiality in sheet metals, as detailed in subsection § 3.6.3.

Consequently, the GTN model may have limitations in predicting rupture occurrence in deep-drawing processes but can indicate its probable zone. Nevertheless, Figure 3-21 shows that the classical use of FLCs effectively predicts rupture occurrence. As a result, combining FLCs with the GTN model offers a robust approach for assessing formability and predicting rupture in deep-drawing processes.

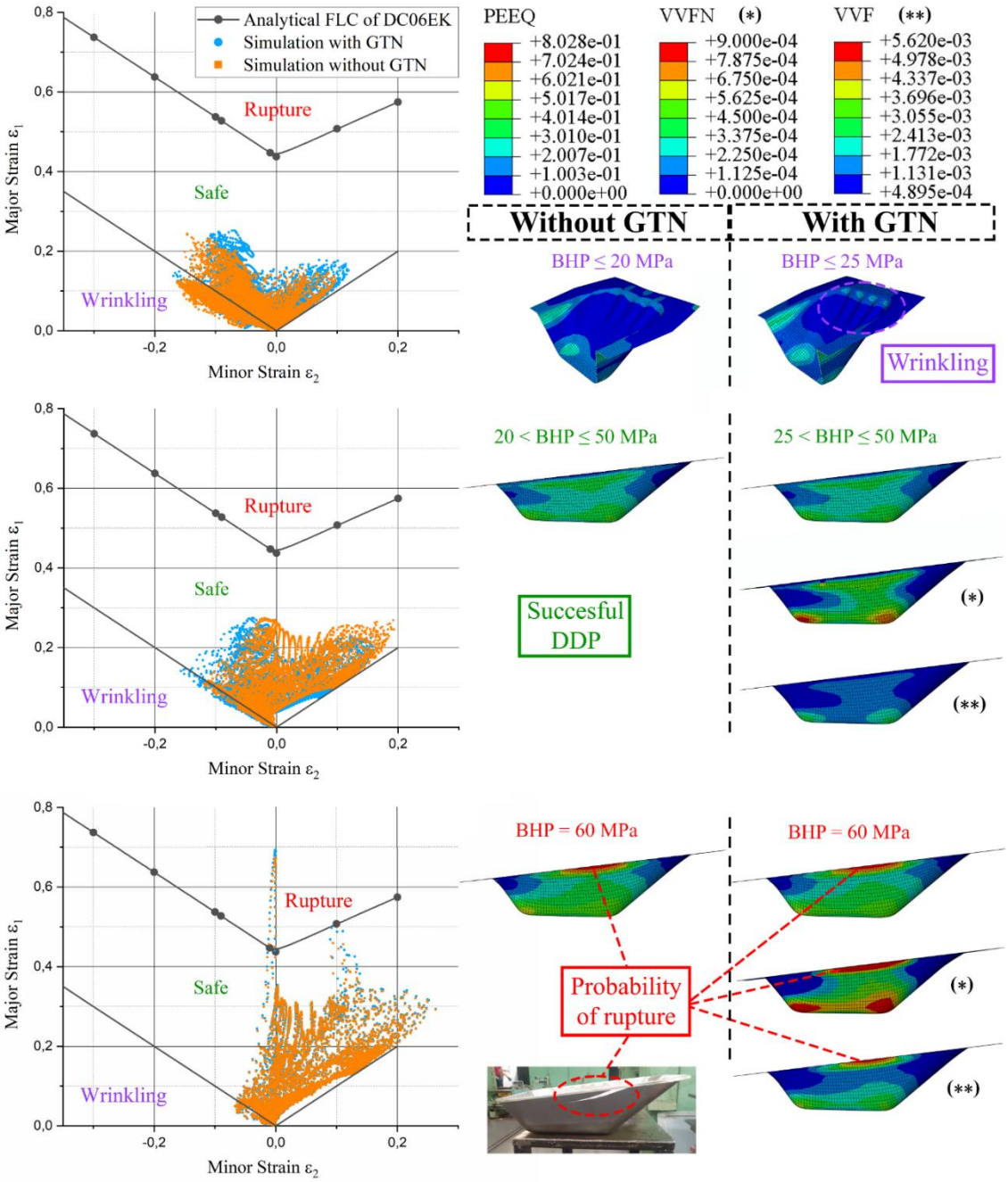

Figure 3-21 : Total void volume fraction VVF and void volume fraction due to the nucleation VVFN cartographies for different blank holder pressures.

3.7. Conclusions

This chapter involved applying the identified parameters of Ludwick's hardening law and GTN damage model in a numerical simulation of an industrial WBT DDP. This numerical approach was validated through ultrasonic thickness measurements which demonstrated its reproducibility and reliability of the numerical model. Additionally, two constitutive models were compared with and without the use of the GTN damage model.

The obtained results shown that the GTN model significantly influences the prediction of wrinkling defect. However, for rupture it revealed certain limitations, as void growth did not reach critical levels that cause accelerated growth of voids and coalescence, likely due to low stress triaxiality in sheet metals. Therefore, The GTN damage model highlighted its reliability in predicting deformation localization (necking) and rupture zone by analyzing VVFN cartographies. Additionally, the stress triaxiality proven to be an important factor with relation to the damage mechanisms and the blank holder pressure.

Moreover, the integration of the GTN damage model with the classical FLCs method has proven to be a robust framework for predicting necking and rupture occurrence. While the GTN model offers a micromechanical perspective by analyzing void nucleation, the FLC method provides macroscopic insights into formability and presence and absence of rupture. Together, these complementary approaches enable more accurate and reliable predictions of material behavior in sheet metal forming processes.

Conclusions & Perspectives

This thesis work aimed to enhance the numerical simulation of the deep drawing process through the experimental characterization of the mechanical behavior of DC06EK sheet metal.

Starting with the anisotropy study, the mean anisotropy coefficient ($R \approx 1.95$) and its deviation ($\Delta R \approx 0.10$) confirmed the material's strong anisotropy. Although quadratic plasticity models like Hill 48 provide a good approximation, they fail to accurately capture the normal anisotropy of DC06EK. Alternative non-quadratic models, such as Hershey-Hosford and Logan-Hosford, may offer better agreement with experimental observations, particularly under biaxial stress conditions. Further experiments, especially biaxial tests, are necessary to fully characterize the anisotropy of DC06EK steel.

The research was conducted in two main phases:

The first phase focused on identifying the GTN damage model parameters coupled with the hardening law using experimental data for DC06EK sheet metal. The results demonstrated a strong correlation between the simulations and experimental observations, with the identified parameters aligning closely with previous studies. The proposed identification strategy proved to be robust and effective for inverse material characterization.

By integrating both local (plastic strains) and global (tensile force) observables simultaneously, the accuracy of parameter identification was significantly enhanced compared to traditional approaches, which typically rely on either local or global observables alone. This simultaneous identification process ensured optimal parameter determination, which is critical for accurately predicting defects such as necking and rupture.

The analysis of the VVFN successfully pinpointed the onset of necking by identifying the point where plastic strains bifurcate into two zones: one exhibiting localized plastic strain and the other showing plastic strain stagnation. This behavior aligns with the fundamental principles used to establish traditional FCLs.

Similarly, the VVF effectively captured rupture initiation in the central zone. The study revealed that the choice of the hardening law, whether coupled or uncoupled with the GTN model, significantly influences the material's behavior and the accuracy of predictions.

In the second phase, the identified parameters of Ludwik's hardening law and the GTN damage model were applied to a numerical simulation of the DDP for an industrial WBT. The simulation results were validated against ultrasonic thickness measurements, demonstrating the model's reliability and reproducibility.

A comparative analysis of two constitutive models, with and without the GTN damage model, was performed. The obtained results shown that the GTN model significantly influences the prediction of wrinkling defect. However, for rupture prediction, the model exhibited limitations. The void growth did not reach the critical levels required for accelerated void coalescence, likely due to the low stress triaxiality characteristic of sheet metals. Despite this, the GTN damage model effectively predicted deformation localization (necking) and rupture zones through the analysis of VVFN cartographies.

The integration of the GTN damage model with the traditional FLC method provided a robust framework for predicting necking and rupture. While the GTN model offers a micromechanical perspective by analyzing void nucleation and growth, the FLC method provides macroscopic insights into formability. Together, these complementary approaches enable more accurate and reliable predictions of material behavior in sheet metal forming processes.

As perspective, several avenues for further research and improvement are identified:

- Future work should include the identification of parameters for anisotropic yield criteria, such as the non-quadratic models of Barlat and Hill [39]. This will require additional tensile tests conducted at 45° and 90° orientations relative to the rolling direction on specimens with variable cross-section. The inclusion of these criteria is particularly relevant for simulating complex processes like the deep drawing of bathtubs, as noted in the work of Hadj Amar [2], where the implementation of anisotropy was shown to be necessary for successful numerical simulations.

- The inverse analysis method should be further developed to incorporate anisotropic plasticity parameters alongside the GTN damage model and hardening laws. This integrated approach will improve the accuracy of simulations for industrial applications.
- Extending the validation of the coupled GTN model to a broader range of industrial deep drawing applications, including automotive and household components, will further confirm its robustness and reliability.

In conclusion, this thesis contributes to the advancement of material characterization and numerical simulation techniques in deep drawing processes. By addressing key challenges in anisotropy modeling, parameter identification, and defect prediction, the findings pave the way for more reliable and efficient industrial applications of deep drawing.

References

[**1**] EIMS-Miliana, ***Entreprise industrielle de materiel sanitaire***, Algeria, 1980.

[**2**] A. Hadj amar, ***Study of the aptitude of DC0xEK steels for enameling and deep drawing***, Thesis, Hassiba benbaouli university of Chlef, Algeria, 2024.

[**3**] C. Alain and M. Colombié, ***L'emboutissage des aciers***, Dunod, 2010.

[**4**] M. Tisza, ***Advanced materials in sheet metal forming***, Key Engineering Materials, 581, 137–142, 2014. DOI: 10.4028/www.scientific.net/KEM.581.137

[**5**] ***Properties and Selection: Irons, Steels, and High Performance Alloys Vol 1,ASM Handbook***, Book, United States of America, ASM international, 2005. ISBN: 0-87170-377-7

[**6**] M. Tisza and Z. Lukács, ***High strength aluminum alloys in car manufacturing***, IOP Conference Series: Materials Science and Engineering, 418(1), 2018. DOI: 10.1088/1757-899X/418/1/012033

[**7**] R. Amaral, P. Teixeira, A. D. Santos, and J. C. de Sá, ***Assessment of different ductile damage models and experimental validation***, International Journal of Material Forming, 11(3), 435–444, 2018. DOI: 10.1007/s12289-017-1381-4

[**8**] A. Kami, B. Mollaei Dariani, *et al.*, ***Application of a GTN damage model to predict the fracture of metallic sheets subjected to deep-drawing***, Proceedings of the Romanian Academy Series A - Mathematics Physics Technical Sciences Information Science, 15(3), 300–309, 2014. ISSN: 14549069

[**9**] S. Laboubi, O. Boussaid, M. Zaaf, and W. Ghennai, ***Numerical investigation and experimental validation of Lemaitre ductile damage model for DC04 steel and application to deep drawing process***, International Journal of Advanced Manufacturing Technology, 126(5–6), 2283–2294, 2023. DOI: 10.1007/s00170-023-11244-0

[**10**] A. Hadj Amar, I. Zidane, H. Zahloul, and A. Belguebli, ***Controlling non-uniform blank holder pressures in an extra-deep drawing process for enhancing formability and product quality***, International Journal of Advanced Manufacturing Technology, 133(1–2), 129–144, 2024. DOI: 10.1007/s00170-024-13746-x

[**11**] A. Belguebli, I. Zidane, A. Hadj Amar, and A. Benhamou, ***Numerical investigation of an extra-deep drawing process with industrial parameters: formability analysis and process optimization***, Frattura ed Integrità Strutturale, 18(68), 45–62, 2024. DOI: 10.3221/igf-esis.68.03

[**12**] S. More, A. Kumar, and K. Narasimhan, ***Parameter identification of GTN damage model using response surface methodology for single point incremental sheet forming of IF steel***, Advances in Materials and Processing Technologies, 8(2), 1753–1768, 2022. DOI: 10.1080/2374068X.2021.1874770

[**13**] K. Belouettar, S. Thibaud, M. Ould Ouali, and M. K. Harouche, ***A numerical-experimental coupled method for the identification of model parameters from μ-SPIF test using a finite element updating method***, International Journal of Advanced Manufacturing Technology, 128(11–12), 5195–5208, 2023. DOI: 10.1007/s00170-023-12210-6

[**14**] P. J. Zhao, Z. H. Chen, and C. F. Dong, ***Experimental and numerical analysis of micromechanical damage for DP600 steel in fine-blanking process***, Journal of Materials Processing Technology, 236, 16–25, 2016. DOI: 10.1016/j.jmatprotec.2016.05.002

[**15**] M. Achouri, G. Germain, P. Dal Santo, and D. Saidane, ***Numerical integration of an advanced Gurson model for shear loading: Application to the blanking process***, Computational Materials Science, 72, 62–67, 2013. DOI: 10.1016/j.commatsci.2013.01.035

[**16**] R. Hambli, ***Comparison between Lemaitre and Gurson damage models in crack growth simulation during blanking process***, International Journal of Mechanical Sciences, 43(12), 2769–2790, 2001. DOI: 10.1016/S0020-7403(01)00070-4

[**17**] M. Rachik, J. M. Roelandt, and A. Maillard, ***Some phenomenological and computational aspects of sheet metal blanking simulation***, Journal of Materials Processing Technology, 128(1–3), 256–265, 2002. DOI: 10.1016/S0924-0136(02)00460-0

[**18**] V. Lemiale, J. Chambert, and P. Picart, ***Description of numerical techniques with the aim of predicting the sheet metal blanking process by FEM simulation***, Journal of Materials Processing Technology, 209(5), 2723–2734, 2009. DOI: 10.1016/j.jmatprotec.2008.06.019

[**19**] H. Marouani, A. Ben Ismail, E. Hug, and M. Rachik, ***Numerical investigations on sheet metal blanking with high speed deformation***, Materials and Design, 30(9), 3566–3571, 2009. DOI: 10.1016/j.matdes.2009.02.028

[**20**] R. Padmanabhan, M. C. Oliveira, J. L. Alves, and L. F. Menezes, ***Influence of process parameters on the deep drawing of stainless steel***, Finite Elements in Analysis and Design, 43(14), 1062–1067, 2007. DOI: 10.1016/j.finel.2007.06.011

[**21**] M. Khelifa and M. Oudjene, ***Numerical damage prediction in deep-drawing of sheet metals***, Journal of Materials Processing Technology, 200(1–3), 71–76, 2008. DOI: 10.1016/j.jmatprotec.2007.08.041

[**22**] T. Bunyan, S. Yiemchaiyaphum, and S. Panich, ***Wrinkling Prediction of Rectangular Cup Deep Drawing Process for Aluminum Alloy Sheets by Using the Modified Yoshida Buckling Test***, Key Engineering Materials, 856, 143–151, 2020. DOI: 10.4028/www.scientific.net/KEM.856.143

[**23**] F. Hamza, O. Boussaid, and K. Tadjine, ***Study by Numerical Simulation of the Deep Drawing Parameters-Material during the Wheelbarrow Forming***, Materials Science Forum, 895, 94–98, 2017. DOI: 10.4028/www.scientific.net/MSF.895.94

[**24**] N. Habibi, V. Sundararaghavan, U. Prahl, and A. Ramazani, ***Experimental and Numerical Investigations into the Failure Mechanisms of TRIP700 Steel Sheets***, Metals, 8(12), 1073, 2018. DOI: 10.3390/met8121073

[**25**] M. Luo, Y. Li, *et al.*, ***Prediction of Shear-induced Crack Initiation in AHSS Deep Drawing Operation with a Phenomenological Fracture Model***, Conference, 2010, 464–472. DOI: 10.1063/1.3457591

[**26**] M. Abbadeni, I. Zidane, H. Zahloul, and Z. Madaoui, ***Comparative study of conventional and hydromechanical deep drawing processes based on finite element analysis***, Frattura ed Integrita Strutturale, 13(49), 2019. DOI: 10.3221/IGF-ESIS.49.28

[**27**] I. Zidane, D. Guines, L. Léotoing, and E. Ragneau, ***Development of an in-plane biaxial test for forming limit curve (FLC) characterization of metallic sheets***, Measurement Science and Technology, 21(5), 055701, 2010. DOI: 10.1088/0957-0233/21/5/055701

[**28**] A. Belguebli, ***Caractérisation des Lois de Comportement Rhéologique et Tribologique d'une Tôle en Acier DC06EK Appliquée à l'Emboutissage***, Thesis, Hassiba Benbouali university of chlef, Algeria, 2024.

[**29**] W. C. Emmens, ***Formability: A review of parameters and processes that control, limit or enhance the formability of sheet metal***, (9783642219030), Book, 2011. DOI: 10.1007/978-3-642-21904-7

[**30**] W. T. Lankford, S. C. Snyder, and J. A. Bauscher, ***New criteria for predicting the press performance of deep drawing sheets***, Thrity-first Annual Convention of the Society, 1–28, 1949.

[**31**] H. J. Bunge, K. Pöhlandt, and A. E. Tekkaya, ***Formability of metallic materials: plastic anisotropy, formability testing, forming limits***, Book, 2013. ISBN: 3-540-67906-5

[**32**] D. Banabic, B. Carleer, *et al.*, ***Sheet metal forming processes: Constitutive modelling and numerical simulation***, Book, 2010. DOI: 10.1007/978-3-540-88113-1

[**33**] M. Abbadeni, ***Simulation de l'Interaction Fluide-Structure Pour le Procédé d'Hydroformage***, Thesis, Université Hassiba Benbouali de Chlef, Algérie, 2018.

[**34**] W. Ghennai, O. Boussaid, *et al.*, ***Experimental and numerical study of DC04 sheet metal behaviour—plastic anisotropy identification and application to deep drawing***, International Journal of Advanced Manufacturing Technology, 100(1–4), 361–371, 2019. DOI: 10.1007/s00170-018-2700-8

[**35**] D. Banabic, ***Multiscale Modelling in Sheet Metal Forming. ESAFORM Book series on Material Forming***, Book, Springer, 2016. ISBN: 978-3-319-44068-2

[**36**] W. F. Hosford, ***A generalized isotropic yield criterion***, Journal of Applied Mechanics, Transactions ASME, 39(2), 607–609, 1972. DOI: 10.1115/1.3422732

[**37**] W. F. Hosford, ***Mechanical Behavior of Materials***, Book, Cambridge University Press, 2005. DOI: 10.1017/CBO9780511810930

[**38**] I. Zidane, ***Developpement d'un banc d'essai de traction biaxiale pour la caractérisation de la formabilité et du comportement élastoplastique de tôles métalliques***, Thesis, Rennes, INSA, 2009.

[**39**] P. M. Dixit and U. S. Dixit, ***Plasticity: Fundamentals and applications***, Book, 2014. DOI: 10.1201/b17588

[**40**] P. M. Dixit and U. S. Dixit, ***Modeling of Metal Forming and Machining Processes by Finite Element and Soft Computing Methods***, Book, 2008. DOI: 10.1007/978-1-84800-189-3

[**41**] M. Djouabi, A. Ati, and P. Y. Manach, ***Identification strategy influence of elastoplastic behavior law parameters on Gurson–Tvergaard–Needleman damage parameters: Application to DP980 steel***, International Journal of Damage Mechanics, 28(3), 427–454, 2018. DOI: 10.1177/1056789518772130

[**42**] S. P. Keeler and W. A. Backofen, ***Plastic instability and fracture in sheets stretched over rigid punches***, Transactions of The ASM, 56, 25–48, 1963. URL: https://dspace.mit.edu/handle/1721.1/120282

[**43**] GOODWIN GM, ***Application of Strain Analysis To Sheet Metal Forming Problems in the Press Shop***, Met Ital, 62(8), 767–774, 1970.

[**44**] ***Tool and Manufacturing Engineers Handbook (Vol 2 : fomring)***, Book, ISBN: 0-87263-135-4

[**45**] F. A. Ahamed J, P. Chinnaiyan, and R. M. Vashishta, ***Hydroforming of nimonic 80 A sheet: a novel optimization based numerical simulation***, International Journal on Interactive Design and Manufacturing (IJIDeM), 2024. DOI: 10.1007/s12008-024-02094-5

[**46**] M. B. Silva, A. J. Martínez-Donaire, *et al.*, ***Recent Approaches for the Determination of Forming Limits by Necking and Fracture in Sheet Metal Forming***, Procedia Engineering, 132, 342–349, 2015. DOI: 10.1016/j.proeng.2015.12.504

[**47**] T. K. Hoang, T. T. Luyen, and D. T. Nguyen, ***Enhancing/Improving Forming Limit Curve and Fracture Height Predictions in the Single-Point Incremental Forming of Al1050 Sheet Material***, Materials, 16(23), 2023. DOI: 10.3390/ma16237266

[**48**] K. Achineethongkham and V. Uthaisangsuk, ***Analysis of forming limit behaviour of high strength steels under non-linear strain paths using a micromechanics damage modelling***, International Journal of Mechanical Sciences, 183, 105828, 2020. DOI: 10.1016/J.IJMECSCI.2020.105828

[**49**] G. Patel, K. Ganesh M, and O. Kulkarni, ***Experimental and numerical investigations on forming limit curves in micro forming***, Advances in Materials and Processing Technologies, 1–12, 2020. DOI: 10.1080/2374068X.2020.1793268

[**50**] A. Werber, M. Liewald, *et al.*, ***Assessment of forming limit stress curves as failure criterion for non-proportional forming processes***, Production Engineering, 7(2–3), 213–221, 2013. DOI: 10.1007/s11740-013-0446-6

[**51**] L. Leotoing, D. Guines, I. Zidane, and E. Ragneau, ***Cruciform shape benefits for experimental and numerical evaluation of sheet metal formability***, Journal of Materials Processing Technology, 213(6), 2013. DOI: 10.1016/j.jmatprotec.2012.12.013

[**52**] L. E. Asp and L. A. Berglund, ***A biaxial thermomechanical disk test for glassy polymers***, Experimental Mechanics, 37(1), 96–101, 1997. DOI: 10.1007/BF02328755

[**53**] S. P. Keeler, ***Relationship between laboratory material characterization and press-shop formability***, 1977.

[**54**] S. K. Paul, ***Controlling factors of forming limit curve: A review***, Advances in Industrial and Manufacturing Engineering, 2(100033), 2021. DOI: 10.1016/j.aime.2021.100033

[**55**] S. S. Hecker, ***A simple forming limit curve technique and results on aluminium alloys***, Conference, Proceedings of the IDDRG Conference, Amsterdam, 1972, 35.

[**56**] VEERMAN CC, HARTMAN L, PEELS JJ, and NEVE PF, ***Determination of appearing and admissible strains in cold- reduced sheets***, Sheet Metal Industries, 48(9), 678–680, 1971. ISSN: 00373435

[**57**] A. Bragard, J.-C. Baret, and H. Bonnarens, ***A simplified technique to determine the FLD at the onset of necking***, 1972.

[**58**] G. Marron, L. Moinier, P. Patou, and J. C. Celeski, ***A new necking criterion for the forming limit diagrams***, Revue de Metallurgie, Cahiers d'Informations Techniques(France), 94(6), 837–845, 1997.

[**59**] A. Col, ***L'emboutiisage des aciers***, Book, in L'usine nouvelle. Série mécanique et matériaux. Paris, Dunod, 2010. ISBN: 9782100520909

[**60**] S. Pasta, C. Catalano, F. Crascì, and R. Scuoppo, ***A custom-built planar biaxial system for soft tissue material testing***, HardwareX, 16, e00475, 2023. DOI: 10.1016/j.ohx.2023.e00475

[**61**] V. Gupta, S. Gupta, and A. Chanda, ***Development of an ultra-low-cost planar biaxial tester for soft tissue characterization***, Biomedical Physics & Engineering Express, 9(2), 025011, 2023. DOI: 10.1088/2057-1976/acb940

[**62**] A. L. Gurson, ***Plastic flow and fracture behavior of ductile materials incorporating void nucleation, growth, and interaction***, Thesis, Brown University, 1975.

[**63**] V. Tvergaard, ***Influence of voids on shear band instabilities under plane strain conditions***, International Journal of Fracture, 17(4), 389–407, 1981. DOI: 10.1007/BF00036191

[**64**] V. Tvergaard, ***On localization in ductile materials containing spherical voids***, International Journal of Fracture, 18(4), 237–252, 1982. DOI: 10.1007/BF00015686

[**65**] V. Tvergaard and A. Needleman, ***Analysis of the cup-cone fracture in a round tensile bar***, Acta Metallurgica, 32(1), 157–169, 1984. DOI: 10.1016/0001-6160(84)90213-X

[**66**] T. Zhang and Y. Zhao, ***A study on the parameter identification and failure prediction of ductile metals using Gurson–Tvergaard–Needleman (GTN) model***, Materials Today Communications, 34, 105223, 2023. DOI: 10.1016/j.mtcomm.2022.105223

[**67**] G. Li and S. Cui, ***A review on theory and application of plastic meso-damage mechanics***, Theoretical and Applied Fracture Mechanics, 109, 2020. DOI: 10.1016/j.tafmec.2020.102686

[**68**] J. Lemaitre, ***A continuous damage mechanics model for ductile fracture***, Journal of Engineering Materials and Technology, Transactions of the ASME, 107(1), 83–89, 1985. DOI: 10.1115/1.3225775

[**69**] Xue Liang, ***Ductile Fracture Modeling - Theory, Experimental Investigation and Numerical Verification***, Thesis, MASSACHUSETTS INSTITUTE OF TECHNOLOGY, 2007.

[**70**] L. Z. Mansouri, H. Chalal, and F. Abed-Meraim, ***Ductility limit prediction using a GTN damage model coupled with localization bifurcation analysis***, Mechanics of Materials, 76, 64–92, 2014. DOI: 10.1016/j.mechmat.2014.06.005

[**71**] A. L. Gurson, ***Continuum theory of ductile rupture by void nucleation and growth: Part 1 - yield criteria and flow rules for porous ductile media***, Journal of Engineering Materials and Technology, Transactions of the ASME, 99(1), 2–15, 1977. DOI: 10.1115/1.3443401

[**72**] C. C. Chu and A. Needleman, ***Void nucleation effects in biaxially stretched sheets***, Journal of Engineering Materials and Technology, Transactions of the ASME, 102(3), 249–256, 1980. DOI: 10.1115/1.3224807

[**73**] J. Koplik and A. Needleman, ***Void growth and coalescence in porous plastic solids***, International Journal of Solids and Structures, 24(8), 835–853, 1988. DOI: 10.1016/0020-7683(88)90051-0

[**74**] M. Springmann and M. Kuna, ***Determination of ductile damage parameters by local deformation fields: Measurement and simulation***, Archive of Applied Mechanics, 75(10–12), 775–797, 2006. DOI: 10.1007/s00419-006-0033-9

[**75**] M. Hadj Miloud, I. Zidane, and M. Mendas, ***Coupled identification of the hardening behavior laws and Gurson–Tvergaard–Needleman damage parameters - Validation on tear test of 12NiCr6 CT specimen***, Frattura ed Integrità Strutturale, 13(49 SE-Articles), 630–642, 2019. DOI: 10.3221/IGF-ESIS.49.57

[**76**] H. Gholipour, F. R. Biglari, and K. Nikbin, ***Experimental and numerical investigation of ductile fracture using GTN damage model on in-situ tensile tests***, International Journal of Mechanical Sciences, 164, 105170, 2019. DOI: 10.1016/j.ijmecsci.2019.105170

[**77**] M. Abbasi, M. A. Shafaat, *et al.*, ***Application of the GTN model to predict the forming limit diagram of IF-Steel***, Journal of Mechanical Science and Technology, 26(2), 345–352, 2012. DOI: 10.1007/s12206-011-1038-z

[**78**] W. Schmitt, D. Z. Sun, and J. G. Blauel, ***Damage mechanics analysis (Gurson model) and experimental verification of the behaviour of a crack in a weld-cladded component***, Nuclear Engineering and Design, 174(3), 237–246, 1997. DOI: 10.1016/S0029-5493(97)00135-0

[**79**] M. Springmann and M. Kuna, ***Identification of material parameters of the Gurson-Tvergaard-Needleman model by combined experimental and numerical techniques***, Computational Materials Science, 32(3–4), 544–552, 2005. DOI: 10.1016/j.commatsci.2004.09.010

[**80**] P. G. Kossakowski, ***Simulation of ductile fracture of S235JR steel using computational cells with microstructurally-based length scales***, Journal of Theoretical and Applied Mechanics, 50(2), 589–607, 2012. ISSN: 14292955

[**81**] R. Kiran and K. Khandelwal, ***Gurson model parameters for ductile fracture simulation in ASTM A992 steels***, Fatigue and Fracture of Engineering Materials and Structures, 37(2), 171–183, 2014. DOI: 10.1111/ffe.12097

[**82**] M. Brunet, F. Sabourin, and S. Mguil-Touchal, ***The prediction of necking and failure in 3 D. Sheet forming analysis using damage variable***, Journal De Physique. IV : JP, 6(6), C6-473-C6-482, 1996. DOI: 10.1051/jp4:1996647

[**83**] A. Ramazani, M. Abbasi, U. Prahl, and W. Bleck, ***Failure analysis of DP600 steel during the cross-die test***, Computational Materials Science, 64, 101–105, 2012. DOI: 10.1016/j.commatsci.2012.01.031

[**84**] H. D. Bui and H. MAIGRE, ***Facteur d'intensité dynamique des contraintes tiré des grandeurs mécaniques globales***, Comptes rendus de l'Académie des sciences. Série 2, Mécanique, Physique, Chimie, Sciences de l'univers, Sciences de la Terre, 1988.

[**85**] C. Chicone and J. Gerlach, ***Identifiability of Distributed Parameters***, Inverse and Ill-Posed Problems, 513–521, 1987. DOI: 10.1016/b978-0-12-239040-1.50038-7

[**86**] A. Bamberger, G. Chavent, C. Hemon, and P. Lailly, ***Inversion of normal incidence seismograms.***, Geophysics, 47(5), 757–770, 1982. DOI: 10.1190/1.1441345

[**87**] A. A. Déom, D. Boscher, and D. L. Balageas, ***Pulsed Photothermal Nondestructive Testing — Application to Carbon Epoxy Laminates***, Review of Progress in Quantitative Nondestructive Evaluation, 525–531, 1990. DOI: 10.1007/978-1-4684-5772-8_65

[**88**] H. D. Bui, ***Introduction aux problèmes inverses en mécanique des matériaux***, Volume 83., Book, France, 1993. ISBN: 2212016352, 9782212016352

[**89**] A. Khalfallah, ***Identification Des Lois De Comportement Élastoplastiques Par Essais Inhomogènes Et Simulations Numériques***, Thesis, Université ElManar-Tunisia, 2004.

[**90**] D. S. Schnur and N. Zabaras, ***An inverse method for determining elastic material properties and a material interface***, International Journal for Numerical Methods in Engineering, 33(10), 2039–2057, 1992. DOI: 10.1002/nme.1620331004

[**91**] A. Gavrus, ***Identification automatique des paramètres rhéologiques par analyse inverse***, Thesis, 1996.

[**92**] A. Gavrus, E. Massoni, and J. L. Chenot, ***The analysis of inelastic behaviour formulated as an inverse rheological approach***, Measurement Science and Technology, 9(6), 848–863, 1998. DOI: 10.1088/0957-0233/9/6/002

[**93**] A. Gavrus, E. Massoni, and J. L. Chenot, ***The rheological parameter identification formulated as an inverse finite element problem***, Inverse Problems in Engineering, 7(1), 1–41, 1999. DOI: 10.1080/174159799088027685

[**94**] A. Gavrus, E. Massoni, and J. L. Chenot, ***Thermo-viscoplastic parameter identification formulated as an inverse finite element analysis of the hot torsion test***, Steel Research, 70(7), 259–268, 1999. DOI: 10.1002/srin.199905637

[**95**] R. Mahnken and E. Stein, ***The identification of parameters for visco-plastic models via finite-element methods and gradient methods***, Modelling and Simulation in Materials Science and Engineering, 2(3 A), 597–616, 1994. DOI: 10.1088/0965-0393/2/3A/013

[**96**] R. Mahnken and E. Stein, ***A unified approach for parameter identification of inelastic material models in the frame of the finite element method***, Computer Methods in Applied Mechanics and Engineering, 136(3–4), 225–258, 1996. DOI: 10.1016/0045-7825(96)00991-7

[**97**] R. Mahnken and E. Stein, ***Parameter identification for finite deformation elasto-plasticity in principal directions***, Computer Methods in Applied Mechanics and Engineering, 147(1–2), 17–39, 1997. DOI: 10.1016/S0045-7825(97)00008-X

[**98**] R. Mahnken and E. Kuhl, ***Parameter identification of gradient enhanced damage models with the finite element method***, European Journal of Mechanics, A/Solids, 18(5), 819–835, 1999. DOI: 10.1016/S0997-7538(99)00127-8

[**99**] J. C. Gelin and O. Ghouati, ***An inverse method for determining viscoplastic properties of aluminium alloys***, Journal of Materials Processing Tech., 45(1–4), 435–440, 1994. DOI: 10.1016/0924-0136(94)90378-6

[**100**] J. C. Gelin and O. Ghouati, ***An inverse method for material parameters estimation in the inelastic range***, Computational Mechanics, 16(3), 143–150, 1995. DOI: 10.1007/BF00369777

[**101**] J. C. Gelin and O. Ghouati, ***An inverse solution procedure for material parameters identification in large plastic deformations***, Communications in Numerical Methods in Engineering, 12(3), 161–173, 1996. ISSN: 10698299

[**102**] O. Ghouati and J. C. Gelin, ***A finite element-based identification method for complex metallic material behaviours***, Computational Materials Science, 21(1), 57–68, 2001. DOI: 10.1016/S0927-0256(00)00215-9

[**103**] J. C. Gelin and O. Ghouati, ***The Inverse Approach for the Determination of Constitutive Equations in Metal Forming***, CIRP Annals - Manufacturing Technology, 44(1), 189–192, 1995. DOI: 10.1016/S0007-8506(07)62304-X

[**104**] O. Ghouati and J. C. Gelin, ***Identification of material parameters directly from metal forming processes***, Journal of Materials Processing Technology, 80–81, 560–564, 1998. DOI: 10.1016/S0924-0136(98)00159-9

[**105**] A. Andrade-Campos, N. Bastos, *et al.*, ***On the inverse identification methods for forming plasticity models using full-field measurements***, IOP Conference Series: Materials Science and Engineering, 1238(1), 012059, 2022. DOI: 10.1088/1757-899x/1238/1/012059

[**106**] O. El Khatib, G. Hütter, *et al.*, ***A non-iterative parameter identification procedure for the non-local Gurson–Tvergaard–Needleman model based on standardized experiments***, International Journal of Fracture, 241(1), 73–94, 2023. DOI: 10.1007/s10704-023-00689-9

[**107**] A. Z. Dizajyekan, M. J. Mirnia, and B. M. Dariani, ***Fracture investigation in single point incremental forming of the Al/Cu laminated sheets using coupled damage plasticity model***, CIRP Journal of Manufacturing Science and Technology, 43, 242–259, 2023. DOI: 10.1016/j.cirpj.2023.04.010

[**108**] A. Ouladbrahim, I. Belaidi, *et al.*, ***Prediction of Gurson Damage Model Parameters Coupled with Hardening Law Identification of Steel X70 Pipeline Using Neural Network***, Metals and Materials International, 28(2), 370–384, 2022. DOI: 10.1007/s12540-021-01024-4

[**109**] M. Abbasi, B. Bagheri, M. Ketabchi, and D. F. Haghshenas, ***Application of response surface methodology to drive GTN model parameters and determine the FLD of tailor welded blank***, Computational Materials Science, 53(1), 368–376, 2012. DOI: 10.1016/j.commatsci.2011.08.020

[**110**] J. Li, S. Li, Z. Xie, and W. Wang, ***Numerical simulation of incremental sheet forming based on GTN damage model***, International Journal of Advanced Manufacturing Technology, 81(9–12), 2053–2065, 2015. DOI: 10.1007/s00170-015-7333-6

[**111**] American Society for Testing and Materials, ***ASTM E8/E8M – 22: Standard Test Methods for Tension Testing of Metallic Materials. Volume 3.01***, Book, ASTM standards, 2022. DOI: 10.1520/E0008_E0008M-22

[**112**] M. A. Sutton, W. J. Wolters, *et al.*, ***Determination of displacements using an improved digital correlation method***, Image and Vision Computing, 1(3), 133–139, 1983. DOI: https://doi.org/10.1016/0262-8856(83)90064-1

[**113**] T. C. Chu, W. F. Ranson, and M. A. Sutton, ***Applications of digital-image-correlation techniques to experimental mechanics***, Experimental Mechanics, 25(3), 232–244, 1985. DOI: 10.1007/BF02325092

[**114**] International Standards Organization, ***ISO 10113: Metallic materials — Sheet and strip — Determination of plastic strain ratio***, Book, ISO, 2020.

[**115**] M. Safaei, M. G. Lee, S. L. Zang, and W. De Waele, ***An evolutionary anisotropic model for sheet metals based on non-associated flow rule approach***, Computational Materials Science, 81, 15–29, 2014. DOI: 10.1016/j.commatsci.2013.05.035

[**116**] A. Kami, B. Mollaei Dariani, *et al.*, ***An experimental study on the formability of a vibration damping sandwich sheet (BONDAL)***, Conference, Proceedings of the Romanian Academy Series A - Mathematics Physics Technical Sciences Information Science, 2017, 281–290. ISSN: 14549069

[**117**] J. Majerníková, E. SPIŠÁK, S. Ján, and F. Wiesław, ***Numerical simulation of deep-drawing process***, Zeszyty Naukowe Politechniki Rzeszowskiej, 4(Mechanika 86 [290]), 561–568, 2014.

[**118**] R. Hill, ***A user-friendly theory of orthotropic plasticity in sheet metals***, International Journal of Mechanical Sciences, 35(1), 19–25, 1993. DOI: https://doi.org/10.1016/0020-7403(93)90061-X

[**119**] DASSAULT SYSTEMES, ***Abaqus/CAE User's Guide (2016)***, Porous metal plasticity, 2016.

[**120**] Y. Bouktir, H. Chalal, and F. Abed-Meraim, ***Prediction of necking in thin sheet metals using an elastic–plastic model coupled with ductile damage and bifurcation criteria***, International Journal of Damage Mechanics, 27(6), 801–839, 2018. DOI: 10.1177/1056789517704030

[**121**] D. Banabic and A. Kami, ***Applications of the Gurson's model in sheet metal forming***, MATEC Web of Conferences, 190, 2018. DOI: 10.1051/matecconf/201819001002

[**122**] Z. H. LI, B. A. BILBY, and I. C. HOWARD, ***a Study of the Internal Parameters of Ductile Damage Theory***, Fatigue & Fracture of Engineering Materials & Structures, 17(9), 1075–1087, 1994. DOI: 10.1111/j.1460-2695.1994.tb00836.x

[**123**] Z. L. Zhang, ***A sensitivity analysis of material parameters for the Gurson constitutive model***, Fatigue and Fracture of Engineering Materials and Structures, 19(5), 561–570, 1996. DOI: 10.1111/j.1460-2695.1996.tb00992.x

[**124**] T. R. Souheyla, ***Simulation numérique de l'emboutissage d'un boitier de chauffage à gaz fabriquée à l'Entreprise Industrielle de Matériel Sanitaire « EIMS »***, Thesis, Hassiba Benbouali University of Chlef, Algeria, 2022.

[**125**] E. Önder and A. E. Tekkaya, ***Numerical simulation of various cross sectional workpieces using conventional deep drawing and hydroforming technologies***, International Journal of Machine Tools and Manufacture, 48(5), 2008. DOI: 10.1016/j.ijmachtools.2007.06.012

[**126**] Y. S. Kim, M. K. Jain, and D. R. Metzger, ***Determination of pressure-dependent friction coefficient from draw-bend test and its application to cup drawing***, International Journal of Machine Tools and Manufacture, 56, 2012. DOI: 10.1016/j.ijmachtools.2011.12.011

[**127**] A.Col, ***L'EMBOUTISSAGE DES ACIERS***, Book, Dunod, 2010.

[**128**] A. J. Martínez-Donaire, M. Borrego, *et al.*, ***Analysis of the influence of stress triaxiality on formability of hole-flanging by single-stage SPIF***, International Journal of Mechanical Sciences, 151, 76–84, 2019. DOI: 10.1016/j.ijmecsci.2018.11.006

[**129**] A. Pineau, A. A. Benzerga, and T. Pardoen, ***Failure of metals I: Brittle and ductile fracture***, Acta Materialia, 107, 424–483, 2016. DOI: 10.1016/j.actamat.2015.12.034

[**130**] A. Bacha, D. Daniel, and H. Klocker, ***On the determination of true stress triaxiality in sheet metal***, Journal of Materials Processing Technology, 184(1–3), 272–287, 2007. DOI: 10.1016/j.jmatprotec.2006.11.031

[**131**] S. Holmberg, B. Enquist, and P. Thilderkvist, ***Evaluation of sheet metal formability by tensile tests***, Journal of Materials Processing Technology, 145(1), 72–83, 2004. DOI: https://doi.org/10.1016/j.jmatprotec.2003.07.004

[**132**] S. P. Keeler and W. G. Brazier, ***Relationship between Laboratory Material Characterization and Press-Shop Formability***, Microalloying 75 Proceedings, 517–530, 1977.

Annex 1. Chemical composition of DC06Ek steel

A03 Numéro de document: K0482767

A05 Acheteur: TOLCOLOR S.A., LE THILLAY CEDEX

A07 Cmde No.: 14117T0017

A06 Destinataire: TOLCOLOR S.A., LE THILLAY CEDEX

No. commande:

B01 Produit: BOBINES LAMINEES A FROID

B02 Matériau: DC 06 EK

B03 Valeur norme: EN 10209/

B03 - Informations supplémentaires
BOBINES LAMINEES A FROID
EN QUALITE DC 06EK
HUILEES

Z01 - Contrôle visuel et contrôle de dimensions: satisfaisants. Nous certifions que la livraison mentionnée ci dessus correspond aux prescriptions de la commande (prescription de m
Z01 - M a r q u a g e : Procede d'acieration, (selon specification), Nuance de material, No. de coulee, No. de tole

Detail de la livraison

B07 No. coulee	B06 No. de tole	B07 Pos	B08 Epaisseur mm	B10 Largeur mm	B11 Longueur mm	B08 Nbre pieces	B12 Brut kg	B13 Net kg	B13 Ref. Art.-No
860797	541330/1	10	1,50	1400,0		1	13.730	13.720	49631
	Totale					1	13.730	13.720	

C70 - Mode d'elaboration, procede d'affinage a l'oxygene

Composition chimique (Analyse de coulee)

B07 No. coulee	C %	Si %	Mn %	P %	S %	Al %	N %	Ti %
860797	.005	.008	.195	.010	.016	.060	.0095	.100

TOLCOLOR SAS
25 rue des Ecoles - BP 039
95508 LE THILLAY Cedex
Tél 01.39.92.86.45 Fax 01.39.92.86.46
Email tolcolor@tolcolor.fr

A04 Sigle de l'usine: voestalpine

A01,A05,Z02 Inspecteur d'usine, Département Qualité, Florennville

voe

No. de tole	L0	Dir	Rp0,2 MEA	Rm MPA	A %
541330	80	T	145	290	38.3

TOLCOLOR SAS
25 rue des Ecoles - BP 839
95508 LE THILLAY Cedex
Tél 01.39.92.86.45 Fax 01.39.92.86.46
Email tolcolor@tolcolor.fr

A04
Sigle de l'usine
voestalpine

A01.A05.Z02
Inspecteur d'usine
Département Qualité
Threnmuller

voesta

Annex 2. Inverse identification script

script1 - Bloc-notes

Fichier Edition Format Affichage Aide

```
File.close()
InputFile.close()

mdb.models['Model-1'].materials
mdb.models['Model-1'].materials['DC06EK'].plastic.setValues(table=((
    SIGMA, ), (AN, ), (KK, )))

mdb.models['Model-1'].materials['DC06EK'].porousMetalPlasticity.setValues(
    relativeDensity=0.9995, table=((1.5, 1, 2.25), ))
mdb.models['Model-1'].materials['DC06EK'].porousMetalPlasticity.voidNucleation.setValues(
    table=((0.3, 0.1, FN), ))
mdb.models['Model-1'].materials['DC06EK'].porousMetalPlasticity.porousFailureCriteria.setValues(
    fraction=FF, criticalFraction=FC)
mdb.save()


mdb.jobs['Epreal'].submit()
        ###: The job input file "Traction_uniaxiale.inp" has been submitted for analysis.
mdb.jobs['Epreal'].waitForCompletion()


o1 = session.openOdb('Epreal.odb')
odb = session.odbs['Epreal.odb']
assembly = odb.rootAssembly
###my_eleset = odb.rootAssembly.elementSets['EPROUVETTE-1.SET-1']
my_force1set = odb.rootAssembly.nodeSets['SET-2']
my_PEEQ1set = odb.rootAssembly.elementSets['SET-4']
my_PEEQ2set = odb.rootAssembly.elementSets['SET-5']

my_instance=odb.rootAssembly.instances['EPROUVETTE-1']
elementList = my_instance.elements
num_element=len(elementList)
num_frames = len(odb.steps['Step-1'].frames)

outputFile = open('observables','w')
s=0
while s< num_frames:
    current_frame = odb.steps['Step-1'].frames[s]
    time_incre=current_frame.frameValue    #### time increment
    time=time_incre

    forceField = current_frame.fieldOutputs['RF']
    forceSubField = forceField.getSubset(region=my_force1set)
    force_1 = forceSubField.values[0].dataDouble[1]
    force_11 = force_1*(2)

    displacementField = current_frame.fieldOutputs['U']
    displacementSubField = displacementField.getSubset(region=my_force1set)
    displacement_1 = displacementSubField.values[0].dataDouble[1]

    centerdispField = current_frame.fieldOutputs['PEEQ']
    centerdispSubField1 = centerdispField.getSubset(region=my_PEEQ1set)
    PEEQ_meshA = centerdispSubField1.values[0].data
```

script1 - Bloc-notes

Fichier Edition Format Affichage Aide

```
from abaqus import *
from sketch import *
from part import *
from material import *
from section import *
from assembly import *
from load import *
from visualization import *
from interaction import *
from step import *
from mesh import *
from job import *
from odbAccess import *
from shutil import *
import assembly
import regionToolset
import displayGroupMdbToolset as dgm
import part
import step
import interaction
import load
import mesh
import job
import visualization
import xyPlot
import displayGroupOdbToolset as dgo
import material
import section


openMdb('epreal.cae')
InputFile = open('parametres','r')
a = InputFile.readline()
T = float(a)
b = InputFile.readline()
SIGMA = float(b)
c = InputFile.readline()
AN = float(c)
d = InputFile.readline()
KK = float(d)
j = InputFile.readline()
FN = float(j)
m = InputFile.readline()
FC = float(m)
k = InputFile.readline()
FF = float(k)
File = open('obs','w')
File.write('%f\t%f\t%f\t%f\t%f\t%f' %(SIGMA, AN, KK, FN, FC, FF))
###File.write('%f\t%f\t%f\t%f\t%f\t%f\t%f' %(SIGMA, AN, KK, FN, FC, FF, PR))
###File.write('%f\t%f\t%f' %(FN, FC, FF))
File.close()
InputFile.close()
```

script1 - Bloc-notes

Fichier Edition Format Affichage Aide

```
        centerdispField = current_frame.fieldOutputs['PEEQ']
        centerdispSubField1 = centerdispField.getSubset(region=my_PEEQ1set)
        PEEQ_meshA = centerdispSubField1.values[0].data

        centerdispField = current_frame.fieldOutputs['PEEQ']
        centerdispSubField2 = centerdispField.getSubset(region=my_PEEQ2set)
        PEEQ_meshB = centerdispSubField2.values[0].data

        ##utputFile.write('%f\t%f\n' %(displacement_1, force_11))
        ##outputFile.write('%f\t%f\t%f\n' %(displacement_1, force_11, PEEQ_meshA))
        outputFile.write('%f\t%f\t%f\t%f\n' %(displacement_1, force_11, PEEQ_meshA, PEEQ_meshB))

        s=s+1
    outputFile.close()
    odb.close()

    mdb.save()
    mdb.close()
```

Annex 3. Data entry for the script (.don file)

ident - Bloc-notes

Fichier Edition Format Affichage Aide

```
2                                       ! modele elements finis
1                                       ! nb de courbes
script1.py                              ! fichier de donnees
exp.data                                ! fichier des donnees exp
ident.res                               ! fichier des resultats d'ident
ident.gr                                ! fichier des resultats
1.E-3                                   ! stagnation STAG
1.E-3                                   ! erreur maximale EQEXIT
1.E-2                                   ! precision calcul derivees
2                                       ! type de norm
0                                       ! type d'impression
0                                       ! nb des variables X(I)
3                                       ! nb des observables
6                                       ! nb de parametres
150.00      130.00      180.00          ! parametre(1)
0.4996      0.200       0.500           ! parametre(2)
370.00      300.00      400.00          ! parametre(3)
0.0008      0.0001      0.0010          ! parametre(4)
0.021       0.0020      0.0030          ! parametre(5)
0.1677      0.050       0.200           ! parametre(6)
```

Annex 4. VUHARD subroutine for Ludwick Law (.for file)

```
      subroutine vuhard(
C Read only -
     *     nblock,
     *     jElem, kIntPt, kLayer, kSecPt,
     *     lAnneal, stepTime, totalTime, dt, cmname,
     *     nstatev, nfieldv, nprops,
     *     props, tempOld, tempNew, fieldOld, fieldNew,
     *     stateOld,
     *     eqps, eqpsRate,
C Write only -
     *     yield, dyieldDtemp, dyieldDeqps,
     *     stateNew )
C
      include 'vaba_param.inc'
C
      dimension props(nprops), tempOld(nblock), tempNew(nblock),
     1   fieldOld(nblock,nfieldv), fieldNew(nblock,nfieldv),
     2   stateOld(nblock,nstatev), eqps(nblock), eqpsRate(nblock),
     3   yield(nblock), dyieldDtemp(nblock), dyieldDeqps(nblock,2),
     4   stateNew(nblock,nstatev), jElem(nblock)
      real*8 SIGMA, AN, KK, epsil
      character*80 cmname
       SIGMA = props(1)
       AN = props(2)
       KK = props(3)
       epsil = 0.00015
      do 100 km = 1,nblock
      IF(eqps(km).GE.0 .AND.eqps(km).LE.epsil) THEN
      yield(km)=SIGMA
      dyieldDeqps(km,1)=0.
      dyieldDeqps(km,2)=0.
      dyieldDtemp(km)=0.
      ELSE IF (eqps(km).GT.epsil) THEN
      yield(km)=SIGMA+(KK*((eqps(km))**AN))
      dyieldDeqps(km,1)=AN*KK*((eqps(km))**(AN-1))
      dyieldDeqps(km,2)=0.
      dyieldDtemp(km)=0.
      END IF
  100 continue
      return
      end
```

Annex 5. VUHARD Subroutine for Voce Hardenig law (.for file)

```
      subroutine vuhard(
C Read only -
     *     nblock,
     *     jElem, kIntPt, kLayer, kSecPt,
     *     lAnneal, stepTime, totalTime, dt, cmname,
     *     nstatev, nfieldv, nprops,
     *     props, tempOld, tempNew, fieldOld, fieldNew,
     *     stateOld,
     *     eqps, eqpsRate,
C Write only -
     *     yield, dyieldDtemp, dyieldDeqps,
     *     stateNew )
C
      include 'vaba_param.inc'
C
      dimension props(nprops), tempOld(nblock), tempNew(nblock),
     1   fieldOld(nblock,nfieldv), fieldNew(nblock,nfieldv),
     2   stateOld(nblock,nstatev), eqps(nblock), eqpsRate(nblock),
     3   yield(nblock), dyieldDtemp(nblock), dyieldDeqps(nblock,2),
     4   stateNew(nblock,nstatev), jElem(nblock)
      real*8 SIGMA, AA, SIGMAS, eps
      character*80 cmname
       SIGMA = props(1)
       AA = props(2)
       SIGMAS = props(3)
       eps = 0.00015
      do 100 km = 1,nblock
      IF(eqps(km).GE.0. AND. eqps(km).LE.eps) THEN
      yield(km)=SIGMA
      dyieldDeqps(km,1)=0.
      dyieldDeqps(km,2)=0.
      dyieldDtemp(km)=0.
      ELSE IF (eqps(km).GT.eps) THEN
      yield(km)=SIGMAS-((SIGMAS-SIGMA)*(EXP(-(eqps(km)-eps)*AA)))
      dyieldDeqps(km,1)=(SIGMAS-SIGMA)*AA*EXP(-(eqps(km)-eps)*AA)
      dyieldDeqps(km,2)=0.
      dyieldDtemp(km)=0.
      END IF
  100 continue
      return
      end
```